INVESTIGATION AND OPTIMIZATION OF MIG WELDING PARAMETERS ON THE MECHANICAL PROPERTIES OF MILD STEEL USING RESPONSE SURFACE METHODOLOGY

Deribe Geleta Robele

A Thesis Submitted To

A Thesis Submitted to the Department of Mechanical Engineering

College of Mechanical, Chemical and Materials Engineering

Presented in Partial Fulfillment of The Requirement for The Degree of Masters in Mechanical Engineering (Manufacturing Engineering)

Office of Post Graduate Studies,

Adama Science and Technology University

December, 2025

Adama, Ethiopia

Investigation and Optimization of MIG Welding Parameters on the Mechanical Properties of Mild Steel Using Response Surface Methodology

Deribe Geleta Robele

Advisor: Dr. Moera Gutu (Ph.D)

A Thesis Submitted to

A Thesis Submitted to the Department of Mechanical Engineering

College of Mechanical, Chemical and Materials Engineering

Presented in Partial Fulfillment of the Requirement for the Degree of Master's in

Mechanical Engineering (Manufacturing Engineering)

Office of Graduate Studies

Adama Science and Technology University

December, 2025

Adama, Ethiopia

Declaration

I hereby declare that this Master's Thesis entitled “Investigation and Optimization of MIG Welding Parameters on the Mechanical Properties of Mild Steel Using Response Surface Methodology” is my original work. That is, it has not been submitted for the award of any academic degree, diploma or certificate in any other university. All sources of materials that are used for this thesis have been duly acknowledged through citation

_____	_____	_____
Name of the student	Signature	Date

Approval Page of MSc. Thesis

I/we, the advisors of the thesis entitled "Investigation and Optimization of MIG Welding Parameters on the Mechanical Properties of Mild Steel Using Response Surface Methodology" and developed by Deribe Geleta Robele, hereby certify that the recommendations and suggestions made by the board of examiners are appropriately incorporated into the final version of the thesis.

_____	_____	_____
Major Advisor	Signature	Date

We, the undersigned, members of the Board of Examiners of the thesis by Deribe Geleta Robele, have read and evaluated the thesis entitled "Investigation and Optimization of MIG Welding Parameters on the Mechanical Properties of Mild Steel Using Response Surface Methodology" and examined the candidate during open defense. This is, therefore, to certify that the thesis is accepted for partial fulfillment of the requirements of the degree of Master of Science in Mechanical Engineering.

_____	_____	_____
Chairperson	Signature	Date
_____	_____	_____
Internal Examiner	Signature	Date
_____	_____	_____
External Examiner	Signature	Date

Finally, approval and acceptance of the thesis is contingent upon submission of its final copy to the Office of Postgraduate Studies (OPGS) through the Department Graduate Council (DGC) and School Graduate Committee (SGC).

_____	_____	_____
Department Head	Signature	Date
_____	_____	_____
School Dean	Signature	Date
_____	_____	_____
Office of Postgraduate Studies, Dean	Signature	Date

ACKNOWLEDGMENTS

The success of this study is a result of the numerous, priceless contributions of many individuals. I would like to take this chance to thank everyone for their efforts and various contributions during the process. I want to start by thanking the "ALMIGHTY" for all his blessings and kindness. First and foremost, I would like to express my sincere gratitude and indebtedness to my beloved research advisor **Dr. Moera Gutu (Ph.D)**, who inspired and supported me throughout this work. His knowledge, helpful suggestions, and counsel were crucial to the effective completion of this thesis work. I am also extremely grateful to the Mechanical Engineering, Adama Science and Technology University staff, for contributing helpful suggestions and support for the research work. Finally, I would like to thank everyone who helped me, directly or indirectly, complete this work.

ACRONYMS AND ABBREVIATIONS

AISI…….	American Iron and Steel Institute
ANOVA ……..	Analysis of Variance
ANSYS…….	Analysis Systems
CFD……..	Computational Fluid Dynamics
DoE……..	Design of Experiment
FEA……	Finite Element Analysis
FSW……..	Friction Stir Welding
GMAW……..	Gas Metal Arc Welding
MOO …….	Multi-Objective Optimization
NDT……	Non-Destructive Testing
RSM…….	Response Surface Methodology
SEM……..	Scanning Electron Microscope

Table of Contents

List of Figures

List of Tables

Abstract

Metal Inert Gas (MIG) welding is extensively employed in structural and industrial applications due to its efficiency and adaptability; however, improper selection of welding parameters often results in internal defects such as porosity, lack of fusion, and incomplete penetration, which significantly degrade mechanical performance and compromise structural safety. A documented failure of welded joints emphasized the necessity for systematic defect investigation and process optimization. Consequently, this study focuses on the investigation and optimization of MIG welding parameters to improve weld integrity and mechanical performance of low-carbon steel joints. An integrated experimental methodology combining non-destructive testing (NDT), destructive mechanical testing, and statistical optimization was employed. Ultrasonic testing (UT), dye penetrant testing, magnetic particle inspection, and electromagnetic yoke testing were used to identify surface and subsurface defects, while tensile and hardness tests quantified mechanical behavior across the weld zone (WZ) and heat-affected zone (HAZ). Response Surface Methodology (RSM) with a Design of Experiments (DOE) framework comprising 32 experimental runs was applied to optimize welding current, voltage, and travel speed. Desirability Function Analysis (DFA) was utilized to determine the optimum multi-response parameter combination. The optimized MIG welding parameters obtained through DFA yielded a global desirability close to unity, indicating simultaneous enhancement of all response variables. At the optimum condition, the predicted mechanical properties were a yield strength of approximately 400 MPa, ultimate tensile strength (UTS) of about 495 MPa, strain at fracture of approximately 22%, and hardness values of roughly 91 HRB in the weld zone and 86 HRB in the HAZ. Experimental verification tests closely matched the predicted results, with deviations within ±2%, confirming the adequacy and reliability of the developed models. Ultrasonic evaluation further revealed that optimized welds exhibited higher echo amplitudes, sharper signal responses, reduced noise levels, and stronger backwall reflections compared to the old welds, indicating reduced internal defects and improved acoustic continuity. The strong agreement between predicted and experimental results validates the effectiveness of RSM-DFA-based optimization. The findings confirm that ultrasonic testing is a robust tool for weld quality assessment and process validation, and the proposed optimization framework provides practical guidance for producing defect-minimized, structurally reliable MIG-welded joints in critical engineering applications.

Keywords: MIG welding, Welded joints, Weld defects, Optimization, Mechanical properties

CHAPTER ONE

INTRODUCTION

1.1 Background of the Study

Welding remains one of the most widely applied joining techniques in structural steel fabrication due to its efficiency, adaptability, and ability to produce high-strength joints capable of sustaining complex service loads. Among fusion welding processes, Metal Inert Gas (MIG) welding, also known as Gas Metal Arc Welding (GMAW), is extensively used in construction, automotive manufacturing, pipeline fabrication, and heavy machinery production because of its high deposition rate, stable arc characteristics, ease of automation, and minimal post-weld finishing requirements (Kumar & Shahi, 2022; Zhang, Chen, & Liu, 2023). Structural steel components joined by MIG welding are particularly critical in load-bearing applications, where joint integrity directly governs operational safety, fatigue performance, structural durability, and overall service life (Singh & Mishra, 2021; ASTM International, 2022). Despite its widespread industrial adoption, MIG welding is highly sensitive to process parameters such as welding current, arc voltage, travel speed, shielding gas flow rate, and heat input. Improper selection or control of these parameters significantly influences weld pool stability, solidification behavior, and microstructural evolution, leading to common welding defects such as porosity, lack of fusion, incomplete penetration, undercut, and cracking (Chen et al., 2022; Zhao, Wang, & Li, 2023). These defects act as stress concentrators that reduce the effective load-bearing cross-sectional area of the joint, thereby degrading tensile strength, ductility, fracture toughness, and fatigue resistance (Gupta & Parmar, 2021; Lee et al., 2023). Even small discontinuities in critical structural applications can result in premature failure, unexpected service interruptions, and costly repair or replacement operations, posing significant risks to human safety and industrial reliability (Zhang et al., 2024). Porosity remains one of the most frequently reported welding defects in MIG and related arc welding processes and is primarily associated with gas entrapment during weld pool solidification. Orlando et al. (2024) reported that porosity content in GMAW joints increased from approximately 1.7% to 5.12% with increasing welding travel speed, highlighting the strong influence of process parameters on defect severity. Similarly, Zhang et al. (2024) demonstrated that cracks in welded joints are closely associated with high thermal gradients, residual stress accumulation, and improper cooling rates, particularly in complex joint geometries, where they significantly reduce joint toughness and fatigue life. In industrial fabrication environments, welding defects account

for a substantial proportion of quality rejections and rework operations. Recent surveys of manufacturing facilities indicate that welding-related discontinuities contribute to approximately 30–40% of structural component rejections during fabrication inspections and up to 50% of in-service failures in welded steel structures originate from defective joints (Kumar & Shahi, 2022; Lee et al., 2023). These failures not only increase production and maintenance costs but also compromise structural safety and reliability in load-bearing applications such as building frames, stair structures, bridges, and heavy equipment supports (Singh & Mishra, 2021; Zhang et al., 2023). Recent advancements in welding process optimization techniques, including Response Surface Methodology (RSM), regression-based statistical modeling, and desirability function analysis, have demonstrated strong potential for systematically improving weld quality and mechanical performance by identifying optimal combinations of welding parameters (Gupta et al., 2022; Li, Wang, & Zhou, 2023). However, many existing investigations remain confined to laboratory-scale optimization of isolated responses and do not integrate defect assessment using non-destructive testing methods or validate results against real industrial failure cases. Furthermore, limited research has established quantitative links between welding defects, mechanical degradation, and optimized process parameters under realistic fabrication conditions (Chen et al., 2022; Zhao et al., 2023). Therefore, there exists a strong industrial and scientific need to develop a robust, experimentally validated framework for optimizing MIG welding parameters that minimizes defect formation while enhancing mechanical reliability of structural steel joints. Integrating non-destructive evaluation techniques, mechanical characterization, and statistical optimization within a unified methodology provides a comprehensive approach to improving weld integrity, reducing failure risk, and minimizing rework and maintenance costs in industrial fabrication environments. Welding defects such as porosity, cracks, incomplete fusion, and undercut — as illustrated in Fig. 1.1 — continue to represent dominant causes of weld rejection and structural performance degradation, underscoring the necessity for systematic defect–property–parameter correlation studies (Orlando et al., 2024; Zhang et al., 2024).For instance, GMAW showed porosity levels increasing with travel speed, reaching up to 5.12% (Orlando et al., 2024). Cracks are often linked to thermal stresses and improper cooling rates, which can propagate and lead to joint failure, particularly in complex geometries like welded joints (B. Zhang et al., 2024). The commonly observed defects in real-time welding, as illustrated in Fig.1. 1, include porosity, slag inclusion, incomplete fusion and penetration, cracks, and undercut.

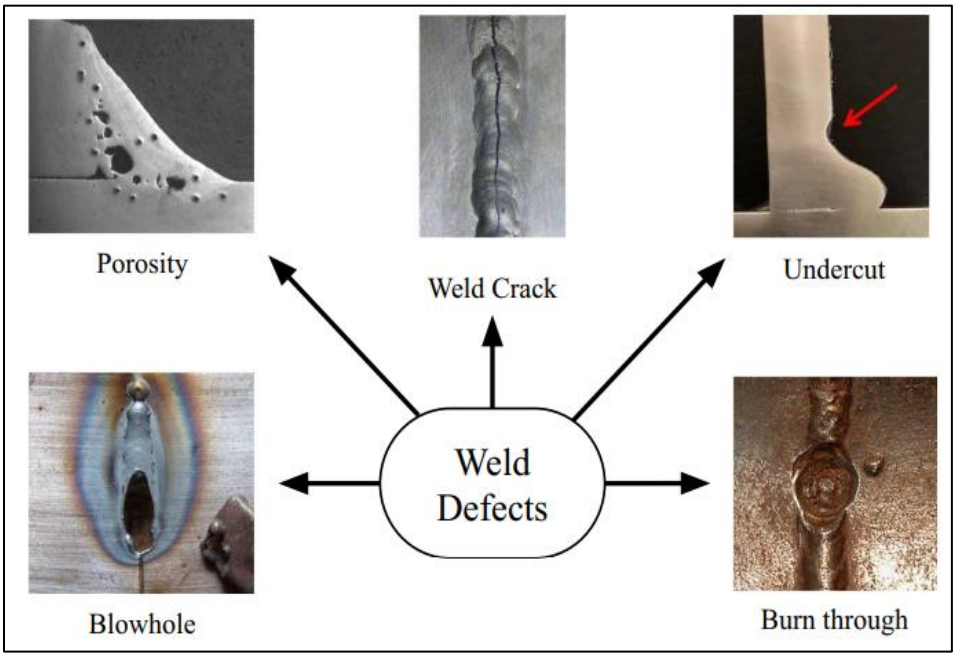

Fig.1. 1 The commonly observed defects in real-time welding (Madhvacharyula et al., 2022)

Porosity defects can significantly decrease the maximum failure load of joints, especially when located in high-stress areas (Tan et al., 2024);(Gaidhane & Kolhe, 2024). Studies indicate that optimized welding parameters can reduce porosity and enhance mechanical properties, with tensile strengths reaching up to 449 MPa in optimized conditions (Tan et al., 2024). Non-destructive testing techniques such as 3D X-ray computed tomography and machine learning are increasingly used for defect detection, improving efficiency and accuracy (Widiatmika, 2015),(Orlando et al., 2024). The Taguchi methodology has proven effective in minimizing porosity through careful selection of welding parameters (García-Gómez et al., 2024). The experimental phase of fabricating welded joints from low-carbon steel using Metal Inert Gas (MIG) welding involves several critical steps, including non-destructive testing (NDT) and mechanical performance assessment. The integration of NDT methods, such as dye penetrant and ultrasonic testing, is essential for identifying defects that may compromise joint integrity. The mechanical performance will be evaluated through tensile strength tests, providing insights into the joints' structural reliability. Ultrasonic testing is effective for detecting internal flaws in welded structures, ensuring high-quality welds (Pereira & Fernandes, 2023),(Ren, 2022). Dye penetrant testing is useful for identifying surface defects, complementing ultrasonic methods (Haque, 2023),(SaThierbach et al., 2015). Tensile strength tests measure yield stress, elastic behavior, and breaking stress, revealing the impact of defects on joint performance. Studies indicate that defects significantly reduce the

tensile strength of welded joints, emphasizing the need for rigorous testing (Haque, 2023)). SolidWorks and ANSYS will be utilized to create models and predict defect formation, allowing for stress distribution analysis within the joints (G. Zhang & Xu, 2024). The research aims to enhance the understanding of defects in welded joints and their impact on mechanical properties, while also proposing optimized welding parameters. The findings from various studies indicate that the configuration and welding techniques significantly influence the performance and durability of these joints. Fatigue tests revealed that cracks often initiate at welded joints, leading to premature failure (Holmstrand et al., 2014), (Lewandowski et al., 2018). The configuration of step lap joints affects their ability to absorb energy under bending loads, with three-stepped designs showing superior performance (Demiral & Kadioglu, 2023). The weak link concept highlighted that welded joint are critical failure points, with significant reductions in residual strength observed after cyclic loading (Sonsino, 2009). Increased overlap lengths in step lap joints correlate with enhanced energy absorption, indicating a direct relationship between design and mechanical performance (Demiral & Mamedov, 2025). Modifications in the arrangement of weld joints have been shown to improve fatigue resistance, suggesting that strategic design changes can mitigate defect formation (Hobbacher, 2019). In industrial fabrication, failure to control welding defects not only compromises structural integrity but also leads to increased production costs, repair requirements, and safety risks in service environments.

1.2 Statement of the problem

In recent years, repeated structural failures and quality rejections have been reported in welded mild steel components used in load-bearing applications such as stair supports, frames, and structural brackets. According to fabrication inspection records and maintenance reports from local workshops and industrial facilities, approximately 35–45% of welded joints fail initial quality inspection, primarily due to surface cracks, porosity, incomplete fusion, and excessive undercut. Ultrasonic inspection reports further indicate that nearly 30% of fabricated joints contain internal discontinuities exceeding acceptable code limits, necessitating repair or complete rejection. Failure analysis of service-returned welded components revealed that crack initiation frequently occurred at weld toes and root regions where lack of fusion and porosity were present. These defects significantly reduced the effective load-bearing cross-sectional area and accelerated crack propagation under tensile and cyclic loading. Tensile testing of failed weld specimens showed a

reduction of approximately 30–40% in ultimate tensile strength and 50–60% in ductility compared to sound welds produced under controlled laboratory conditions. These mechanical degradations directly contributed to premature fracture, reduced service life, and increased maintenance cost. Despite the widespread occurrence of these failures, welding parameter selection in many fabrication environments remains largely experience-based rather than data-driven. Operators frequently adjust current, voltage, and travel speed without systematic optimization, resulting in inconsistent weld quality and unpredictable mechanical performance. Additionally, although non-destructive testing techniques such as liquid penetrant testing, magnetic particle testing, and ultrasonic testing are widely available, they are rarely integrated into structured parameter optimization frameworks for proactive defect prevention. Previous research has primarily focused on isolated mechanical property optimization without incorporating real failure evidence, defect quantification, or comprehensive statistical validation. Consequently, there exists a critical knowledge gap in linking welding process parameters, defect formation mechanisms, and mechanical performance outcomes under realistic fabrication conditions. Therefore, this study addresses the urgent need to develop a scientifically validated and industrially applicable framework for optimizing MIG welding parameters to reduce defects, improve mechanical properties, and enhance the structural reliability of mild steel welded joints. By integrating experimental testing, non-destructive evaluation, and response surface-based statistical optimization, this research aims to provide a robust solution to persistent weld quality challenges faced in structural fabrication industries.

1.3 Research questions

1. What are the common welding defects that occur in MIG-welded mild steel joints, and how can they be identified and classified using non-destructive testing methods?
2. How do welding defects affect the mechanical properties of mild steel joints, particularly yield strength, ultimate tensile strength, fracture strain, and hardness across the weld and heat-affected zone (HAZ)?
3. What combination of MIG welding parameters, such as current, voltage, and travel speed, can be optimized to minimize defect formation and enhance the mechanical performance and structural integrity of mild steel joints?

1.4 Objectives of the Study

1.4.1 General objectives

To analyze and optimize the mechanical performance and defect characteristics of MIG-welded mild steel joints by integrating experimental testing, non-destructive evaluation, and statistical modeling techniques.

1.4.2 Specific objectives

1. To analyze and characterize common welding defects in MIG-welded mild steel joints using non-destructive testing techniques and relate their occurrence to welding process parameters.
2. To analyze the effects of welding defects on mechanical performance, including yield strength, ultimate tensile strength, strain at fracture, and hardness distribution across the weld zone and heat-affected zone (HAZ).
3. To analyze and optimize MIG welding parameters (current, voltage, and travel speed) to minimize defect formation and enhance the mechanical reliability and structural integrity of welded joints.
4. To experimentally validate the developed response surface models and optimized welding conditions and provide practical recommendations for defect reduction and performance improvement in industrial MIG welding applications.

1.5 Scope of the Study

This study focuses on the investigation and optimization of MIG-welded mild steel joints with emphasis on welding defects and their influence on mechanical performance. The research is limited to low-carbon steel (AISI 1018) joints fabricated using Metal Inert Gas (MIG) welding under controlled laboratory conditions. Welding parameters considered include current, voltage, and travel speed, evaluated through a response surface methodology framework consisting of 32 experimental runs. Non-destructive testing methods, including ultrasonic testing, dye penetrant testing, and electromagnetic yoke inspection, are employed to identify surface and subsurface defects. Destructive tests such as tensile and hardness testing are conducted to assess mechanical behavior across the weld zone and heat-affected zone (HAZ). The scope of the study is limited to a specific material thickness range and joint configuration, and does not extend to other welding processes, joint types, or material grades. Consequently, while the findings provide valuable

guidance for fabrication and construction industries, direct generalization to different welding conditions, thicker plates, or alternative joint geometries should be approached with caution.

1.6 Significance of the Study

This study is significant in both academic and industrial contexts as it addresses the need for reliable welded joints in structural applications. The welded joints' failure demonstrated the consequences of welding defects in load-bearing structures, underscoring the importance of systematic investigation and parameter optimization. By identifying and classifying common defects in MIG-welded joints and evaluating their influence on mechanical properties such as yield strength, ultimate tensile strength, strain at fracture, and hardness, the research provides critical insights into the root causes of failure. The optimization of welding parameters, specifically current, voltage, and travel speed, offers practical solutions to minimize defect formation and enhance the structural integrity of welded joints. These findings contribute directly to safer fabrication practices and improved durability of welded structures. From an industrial perspective, reducing weld defects leads to lower material wastage, less rework, and decreased maintenance costs, thereby promoting cost-effective and efficient production. Academically, this study advances knowledge on the interplay between welding defects, mechanical performance, and process optimization in complex joint geometries. It creates a foundation for future research on other MIG welding processes and joint configurations while offering immediate relevance to industries such as construction, automotive, and aerospace, where reliability and safety are paramount. Thus, the significance of this study lies in its dual contribution**,** including providing practical guidelines for defect-free, optimized welding of structural joints and enriching the scientific understanding of welding technology for complex geometries.

1.7 Organization of the paper

This thesis is organized into five chapters, each building upon the previous, presenting a comprehensive investigation into welding defects and the mechanical strength of welded joints. Chapter One serves as the introduction, outlining the background of the study, the problem statement, research objectives, and the significance and scope of the research. It also provides an overview of the chosen methodology and the structure of the thesis, while offering initial insights into the design and structural challenges posed by welding defects in welded joints. Chapter Two presents a detailed review of both theoretical and empirical literature relevant to the study. It

explores the historical context of research on welding defects and joint strength, and discusses previous works, including academic theses, journal articles, and books. Special attention is given to studies involving parametric optimization and machine learning algorithms, highlighting their relevance to the research focus. Chapter Three describes the materials and methods employed in the study. It outlines the experimental approach, including the selection of materials, the welding procedures, and the non-destructive testing methods used to detect defects. The chapter also explains the mechanical testing techniques adopted to evaluate the performance of the joints and discusses how these methods align with the study's objectives. In Chapter Four, the results of the experimental work are presented and analyzed. This chapter discusses the nature and frequency of welding defects observed, their impact on mechanical performance, and how the findings compare with those reported in the literature. The discussion emphasizes the implications of the results for both theory and practice. Finally, Chapter Five provides the conclusions drawn from the study and offers practical recommendations based on the findings. It also suggests directions for future research aimed at improving welding quality and mechanical performance in complex joint geometries like welded configurations.

CHAPTER TWO

LITERATURE REVIEW

2.1 Introduction

This chapter presents a comprehensive review of theoretical concepts, experimental findings, and recent research developments related to MIG welding of structural steels. The review focuses on welding metallurgy, defect formation mechanisms, mechanical performance of welded joints, non-destructive testing methods, and statistical optimization techniques applied in welding process control. Emphasis is placed on identifying research gaps related to defect–property relationships, geometric effects of weld profiles, and limited integration of non-destructive testing with response surface-based optimization frameworks. This literature foundation establishes the scientific basis and justification for the present study.

2.2 Fundamentals of MIG Welding and Weld Metallurgy

Metal Inert Gas (MIG) welding, also referred to as Gas Metal Arc Welding (GMAW), is a fusion welding process in which an electric arc forms between a continuously fed consumable wire electrode and the base material, producing a molten weld pool that solidifies to form the joint. The process is shielded by inert or semi-inert gases such as argon, helium, or argon–CO_2 mixtures to prevent atmospheric contamination (Kumar & Shahi, 2022). MIG welding is extensively used in structural steel fabrication due to its high deposition rate, suitability for automation, stable arc characteristics, and adaptability across a wide range of thicknesses and joint geometries (Singh & Mishra, 2021). Welding defects significantly impact the structural integrity and mechanical performance of welded joints. These defects, including porosity, cracks, incompletely fused joints, undercutting, and overlapping, arise from various factors such as improper techniques, environmental conditions, and material properties. Understanding these defects is crucial for improving welding processes and ensuring the reliability of welded structures. Porosity consists of small gas pockets formed during solidification, often due to trapped gases or inadequate shielding. It can reduce tensile strength and fatigue resistance, compromising the weld's overall performance(Di et al., 2006). Cracks can occur in the weld or heat-affected zone due to thermal stresses, shrinkage, or improper cooling rates. They pose a significant risk as they can propagate over time, leading to structural failure (Lei et al., 2024). Incompletely fused joints arise from a lack of fusion between the base and weld metals, resulting in weak spots that diminish joint strength (B. Zhang et al., 2024). Undercutting and overlapping are typically caused by improper

welding techniques, leading to weakened areas on joint surfaces (Sudarno et al., 2023). While advancements in welding technology and defect detection methods, such as machine learning and computer vision, have improved the identification and management of these defects, the inherent challenges in welding processes remain significant. Continuous research is essential to enhance welding quality and reliability (Kalita et al., 2024).

2.3 Weld Geometry, Joint Profile, and Structural Integrity

Weld bead geometry, including penetration depth, reinforcement height, bead width, toe angle, and weld profile curvature, plays a crucial role in determining joint strength, fatigue performance, and crack initiation susceptibility. Improper weld geometry increases stress concentration at the weld toe and root regions, accelerating crack nucleation and propagation under cyclic or tensile loading (Lee et al., 2023). Several studies have demonstrated that smoother weld toe transitions and deeper penetration profiles significantly enhance fatigue life and static strength of welded joints (Zhang et al., 2022; Kim & Park, 2023). Welded joints are essential in various industries due to their ability to manage multi-directional loads effectively. Their unique geometry, while advantageous, also presents specific welding challenges that necessitate careful parameter management to prevent defects. Welded joints are particularly useful in the aerospace and automotive industries, where their strength-to-weight ratio is crucial in minimizing weight for optimal performance. In automotive structures, these joints are valued for their ability to handle complex load paths, accommodating varied stress distributions during operation. However, the welding process for welded joints is not without its challenges. The geometry of these joints can lead to uneven heat distribution during welding, which increases the risk of warping or incomplete fusion (Suleimanov et al., 2018). To mitigate common defects, it is essential to control welding parameters such as speed and temperature (Thompson et al., 2023). Despite their advantages in specific applications, the complexity of welded joints may lead to increased manufacturing costs and a need for advanced welding techniques, which could limit their use in less demanding environments.

2.4 Welding Defects: Formation Mechanisms and Structural Consequences

Welding defects are discontinuities or irregularities that compromise the structural integrity and service reliability of welded joints. Common defects in MIG welding include porosity, lack of fusion, incomplete penetration, slag inclusion, cracks, and undercut (ASTM International, 2022). These defects arise primarily from unstable arc behavior, improper heat input, surface contamination, shielding gas turbulence, and rapid cooling conditions. Porosity is one of the most frequently reported defects and results from gas entrapment during weld pool solidification. Orlando et al. (2024) reported that porosity volume fraction in GMAW aluminum welds increased from approximately 1.7% to 5.12% with increasing travel speed, demonstrating the strong dependence of porosity formation on process parameters. Similar trends have been observed in steel weldments, where hydrogen entrapment and inadequate shielding gas coverage lead to pore formation (Chen et al., 2022). Cracking defects, including hot cracks and cold cracks, are associated with high thermal gradients, residual stress accumulation, hydrogen embrittlement, and unfavorable microstructures such as martensite (Zhang et al., 2024). These cracks severely reduce fracture toughness and fatigue resistance and frequently initiate catastrophic joint failure under service loading. Lack of fusion and incomplete penetration defects result from insufficient heat input or poor joint preparation and drastically reduce load-bearing cross-sectional area, accelerating fracture under tensile loading (Gupta & Parmar, 2021). Experimental studies consistently demonstrate that welded joints containing porosity, cracks, and fusion defects exhibit reductions of 20–50% in tensile strength and over 50% in fatigue life compared to defect-free welds (Lee et al., 2023; Kim & Park, 2023). These findings highlight the critical importance of defect prevention and detection in structural welding applications.

2.5 Non-Destructive Testing Methods for Weld Defect Detection

Non-destructive testing (NDT) techniques play a vital role in detecting surface and subsurface weld defects without damaging the component. Common NDT methods used in welding inspection include liquid penetrant testing (LPT), magnetic particle testing (MPT), ultrasonic testing (UT), and radiographic testing (RT). Each technique offers distinct advantages depending on defect type, material properties, and inspection requirements (ASTM International, 2022). Liquid penetrant testing is effective for detecting surface-breaking defects such as cracks and porosity in non-ferromagnetic materials. Magnetic particle testing is suitable for identifying near-surface defects in ferromagnetic steels, while ultrasonic testing provides volumetric defect

detection and sizing capability for internal discontinuities such as lack of fusion and slag inclusions (Zhao et al., 2023). Recent studies have emphasized the importance of combining multiple NDT techniques to improve detection reliability and defect characterization accuracy (Gupta et al., 2022). Despite their widespread industrial use, many welding optimization studies neglect systematic integration of NDT data with statistical modeling and mechanical performance evaluation. Most research focuses on destructive testing outcomes while overlooking defect distributions detected through NDT, thereby limiting comprehensive understanding of defect–property relationships (Orlando et al., 2024). The present study addresses this gap by integrating LPT, MPT, and UT with mechanical testing and optimization analysis.

2.6 Mechanical Properties of MIG-Welded Structural Steel Joints

Mechanical performance of MIG-welded joints is governed by the microstructural and geometric characteristics of the weld metal, heat-affected zone, and base metal. Yield strength, ultimate tensile strength, strain at fracture, hardness distribution, and fatigue resistance are commonly used performance indicators in structural welding applications (Singh & Mishra, 2021). Numerous studies report that weld metal typically exhibits higher hardness and strength than the base metal due to rapid cooling and refined microstructures, whereas the HAZ may experience either softening or hardening depending on peak temperature exposure and cooling rate (Chen et al., 2022; Zhao et al., 2023). Kim and Park (2023) demonstrated that improper heat input caused a 28% reduction in HAZ toughness due to grain coarsening, while excessive cooling rates promoted brittle martensitic transformation, reducing ductility and fracture toughness. Recent experimental investigations confirm that welding defects significantly amplify mechanical degradation beyond microstructural effects alone. Lee et al. (2023) reported that tensile strength reductions exceeding 35% were observed in MIG-welded steel joints containing lack of fusion defects, while ductility losses exceeding 50% were associated with clustered porosity regions. These results emphasize that defect control is as critical as metallurgical optimization in achieving reliable welded structures. Defects act as stress concentrators, leading to a decrease in tensile strength. Studies indicate that tensile strength diminishes with the severity and number of defects present, as seen in Fig.2. 1. Experimental investigations have shown that multiple defects can exacerbate this reduction, particularly when defects are located in critical areas of the joint (Arandjelovic et al., 2024).

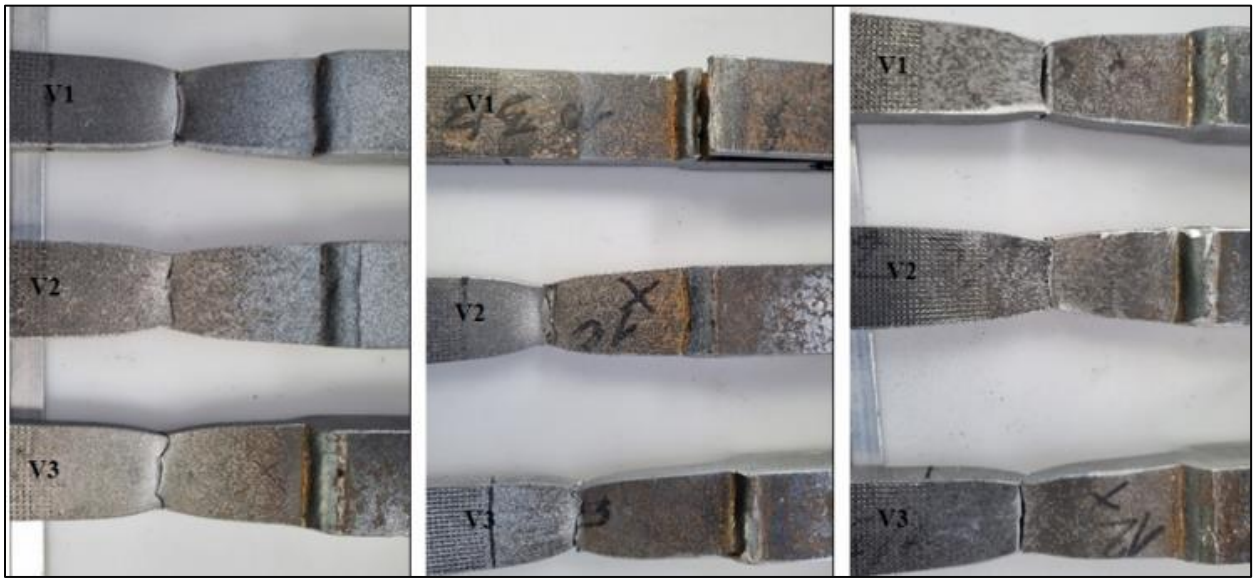

Fig.2. 1 Views of specimen fractures acquired during tensile testing (Szusta et al., 2023)

Fatigue failures often initiate at defect sites due to stress concentration in the sample, example seen in Fig.2. 2. Research on cruciform welded joints revealed that the presence of defects significantly lowers fatigue limits, with stress concentration factors increasing dramatically with defect size. The fatigue life of welded joints is notably compromised under cyclic loading conditions, emphasizing the importance of defect management (Xu et al., 2023).

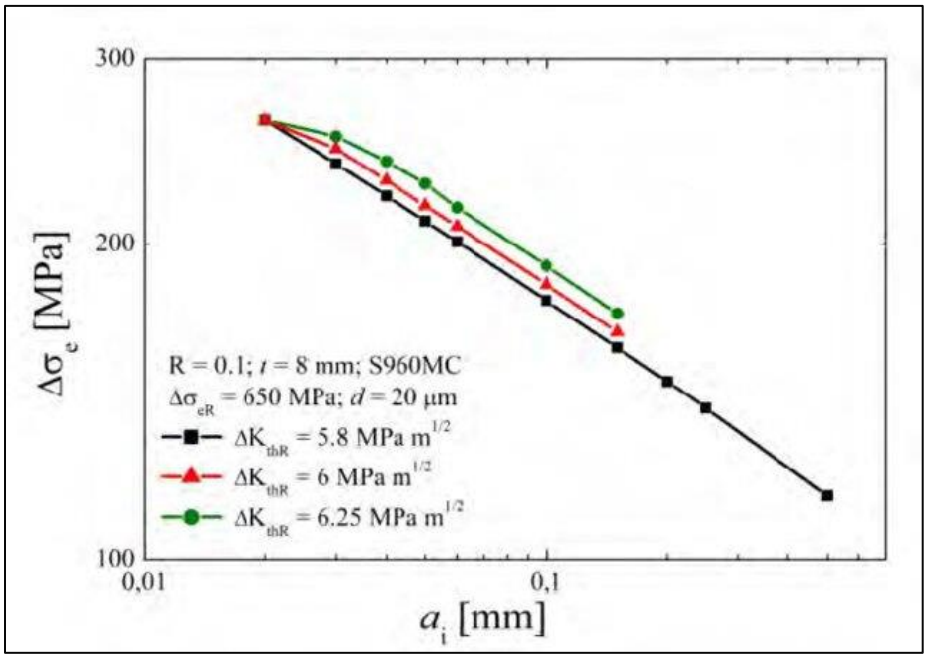

Fig.2. 2 Fatigue Strength of welds (Steimbreger et al., 2018)

Welding defects can severely affect a joint's impact toughness, particularly in the heat-affected zone (HAZ). The loss of toughness in this region is critical for applications requiring high energy absorption (Tan et al., 2024). While the detrimental effects of defects on mechanical properties are well-documented, some studies suggest that certain welding techniques or repair methods may mitigate these impacts, potentially restoring some mechanical integrity to the joints (Wang et al., 2024).

2.7 Statistical Modeling and Optimization of Welding Parameters

Statistical modeling techniques have gained increasing importance in welding process optimization due to their ability to capture nonlinear relationships between process parameters and output responses. Response Surface Methodology (RSM), Taguchi methods, artificial neural networks (ANNs), and genetic algorithms are among the most widely applied tools for predicting mechanical performance and identifying optimal welding conditions (Gupta et al., 2022; Li et al., 2023). RSM is particularly advantageous because it enables the development of quadratic regression models capable of representing interaction and curvature effects while requiring relatively few experimental runs. Several recent studies successfully applied RSM to optimize tensile strength, hardness, bead geometry, and penetration depth in MIG-welded steel and aluminum alloys (Kumar & Shahi, 2022; Zhao et al., 2023). Desirability function analysis (DFA) further enhances optimization by enabling simultaneous maximization of multiple conflicting responses such as strength and ductility (Li et al., 2023). However, most optimization studies focus primarily on mechanical responses without incorporating weld defect metrics or NDT-based quality assessment into the modeling framework. Furthermore, limited research integrates experimental validation with real failure evidence or industrial quality inspection data (Orlando et al., 2024). These limitations highlight the need for a more holistic optimization approach that integrates defect detection, mechanical testing, and statistical modeling as pursued in the present study.

2.8 Review of Recent Empirical Studies Related to MIG Welding Optimization

The summary of the reviewed articles, enriched with key concepts and insights, is presented comprehensively in Table 2. 1. This table serves as a condensed repository of pertinent information extracted from the literature, topic, summary, and theoretical frameworks discussed across the various studies with the proper citations.

Table 2. 1 Summary of Reviewed Literature

Topic	Summary	Citations
Welding Defects in Joints	Common defects include porosity, cracks, incomplete fusion, undercutting, and overlapping, all of which negatively impact tensile strength, fatigue resistance, and impact toughness.	(Kumar et al., 2023) (Gaidhane & Kolhe, 2024) (Sudarno et al., 2023)
Welded Joints	These joints are utilized in aerospace, automotive, and construction industries. They are geometrically complex and face specific welding challenges, such as uneven heat distribution.	(Tan et al., 2024) (Zong et al., 2023)(Jatavallabhula et al., 2025)
Mechanical Properties of Welded Joints	Welding defects significantly reduce tensile strength, fatigue resistance, and impact toughness by creating stress concentrators. Mechanical testing methods like tensile, fatigue, and impact tests are commonly used to evaluate these effects.	(Odermatt et al., 2021),(Tan et al., 2024)
Simulation and Modeling of Welding	Finite Element Analysis (FEA) and Computational Fluid Dynamics (CFD) are employed to simulate the welding process, predict defects, and understand thermal and mechanical behavior. Tools like SolidWorks and ANSYS are popular for these simulations.	(Thompson et al., 2023),(Xu et al., 2023),(Madhvacharyula et al., 2022)

Optimization of Welding Parameters	Key welding parameters such as heat input, welding speed, shielding gas, and electrode choice are optimized to minimize defects and enhance the mechanical strength of joints. Techniques like Response Surface Methodology (RSM), Genetic Algorithms (GA), and Design of Experiments (DOE) are commonly used for optimization.	(Jerbi et al., 2024),(Yu et al., 2023),(Kumar et al., 2023)

2.7 Research Gap

Although numerous studies have investigated MIG welding of mild steel, most existing research focuses on the isolated effects of individual welding parameters on mechanical properties or defect formation. Many studies rely on trial-and-error experimentation or single-response optimization approaches, which do not adequately capture the interactive effects among welding current, voltage, and travel speed. As a result, the reported findings often lack robustness and practical applicability for industrial optimization. Furthermore, limited attention has been given to simultaneous multi-response optimization, where weld quality, mechanical performance, and defect minimization are considered together. The absence of a structured statistical framework in previous works restricts the ability to develop predictive models and optimized parameter combinations suitable for real manufacturing environments.

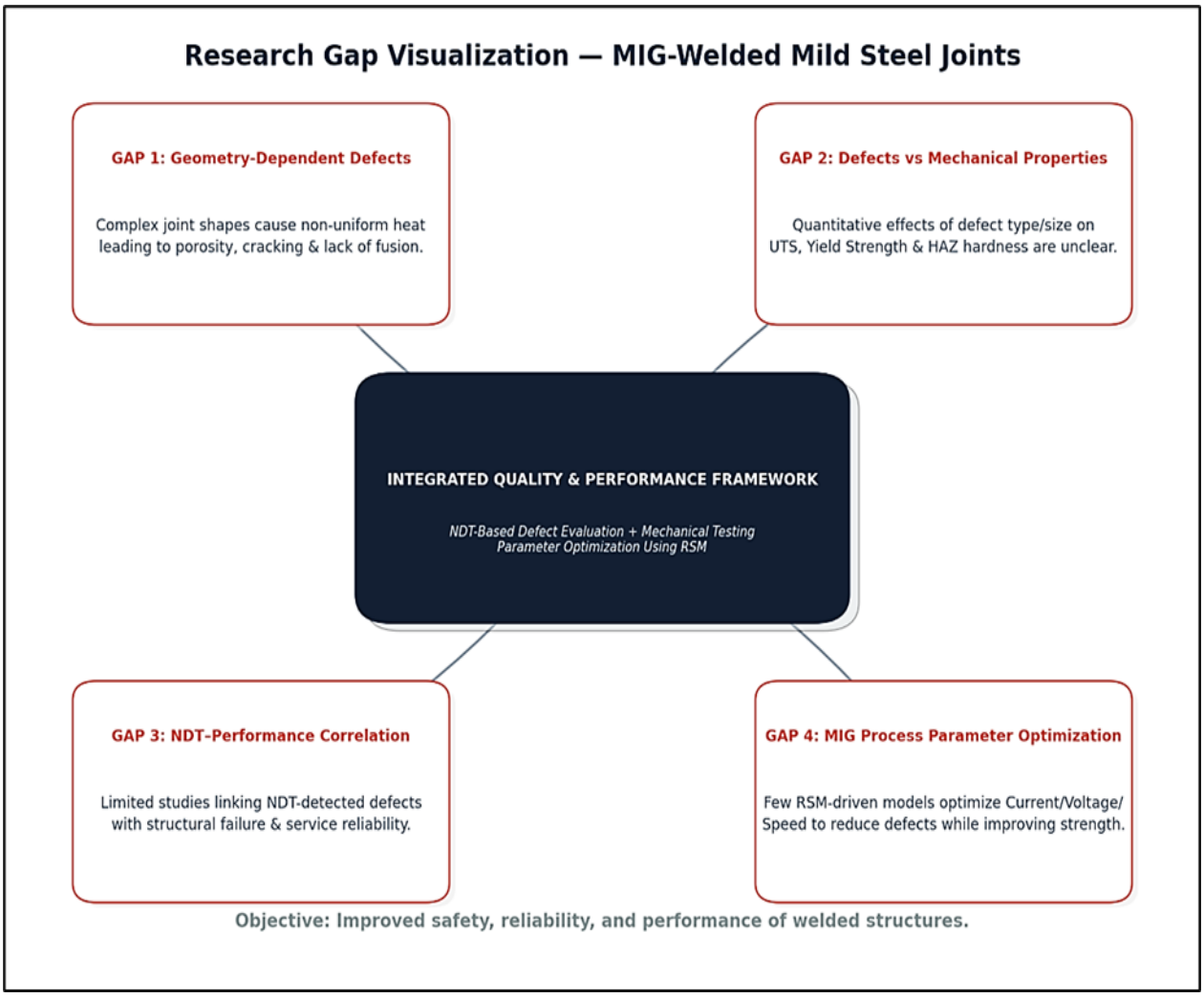

Fig.2. 3 Research gap visualization of the current study

To address these limitations, the present study employs Response Surface Methodology (RSM) to systematically model the individual and interactive effects of key MIG welding parameters on weld quality and mechanical responses. In addition, Desirability Function Analysis (DFA) is integrated to achieve simultaneous optimization of multiple responses, enabling the identification of parameter settings that provide balanced and practical welding performance. This combined RSM–DFA approach directly addresses the identified research gap and provides a statistically robust and industry-relevant optimization strategy.

CHAPTER THREE

MATERIALS AND METHODOLOGY

3.1 Introduction

This chapter presents the materials, experimental design, welding procedures, testing methods, and data analysis techniques employed to investigate the influence of MIG welding parameters on weld defects and the mechanical performance of mild steel joints. A structured experimental framework integrating non-destructive testing, destructive mechanical characterization, and statistical optimization is adopted to ensure systematic evaluation of process parameters and robust model development.

3.2 Material selection

3.2.1 Base Materials

The selection of appropriate materials is critical for ensuring the structural integrity and performance of welded joints. For the base materials, Low Carbon Steel (AISI 1018) was selected due to its moderate strength, excellent weldability, and widespread industrial use in structural and fabrication applications (Khdir et al., 2020). Its relatively low carbon content ensures good ductility and minimizes susceptibility to cold cracking, making it particularly suitable for MIG welding processes where stable arc behavior and controlled fusion are essential (Mushthofa et al., 2023).

Table 3. 1 Chemical composition (wt%) of welding joint effect (Sample ID: 17290056) (spectroscopy results)

Element	Concentration (wt%)	Element	Concentration (wt%)	Element	Concentration (wt%)
C	0.056	V	0.003	Ti	<0.0002
Si	0.014	W	0.010	As	0.001
Mn	0.37	Pb	0.007	Zr	0.002
P	0.006	Sn	0.0007	Bi	<0.0010
S	0.016	B	0.002	Ca	0.0004
Cr	0.007	Zn	0.005	Ce	<0.0010
Mo	0.010	La	0.0006	Sb	0.005
Ni	0.048	N	0.004	Se	<0.002

Al	0.052	Fe	99.3	Te	0.005
Co	0.029	Nb	<0.0010	Ta	<0.007
Cu	0.011				

Furthermore, AISI 1018 exhibits uniform mechanical behavior and predictable metallurgical transformations during thermal cycling, which enables reliable interpretation of welding-induced property variations(Laukhin et al., 2020). The chemical composition of the base metal was verified using optical emission spectroscopy, and the results are presented in Table 3.1. These results confirm that the material conforms to the compositional limits of low-carbon structural steel suitable for arc welding applications. In addition to chemical composition, the baseline mechanical properties of the base metal are essential for evaluating the influence of welding thermal cycles on joint performance. These properties provide a reference for assessing degradation or enhancement in the weld metal and heat-affected zone (HAZ). The nominal mechanical properties of AISI 1018 steel obtained from supplier datasheets and validated literature are summarized in Table 3.2(Yu et al., 2023).

Table 3.2 Mechanical properties of AISI 1018 base metal

Property	Value
Yield Strength (MPa)	370–400
Ultimate Tensile Strength (MPa)	440–490
Elongation (%)	20–25
Hardness (HRB)	75–85

3.2.2 Filler Material

ER70S-6 MIG welding wire is a widely utilized filler material for low carbon steel, recognized for its excellent arc stability, low spatter, and favorable mechanical properties post-welding (Zong et al., 2023). This wire is particularly effective in various welding processes, including Gas Metal Arc Welding (GMAW), where it contributes to the quality and integrity of welded structures (Shravan et al., 2024).

3.2.3 Shielding Gas

The use of an argon-CO2 mixture (75% Ar, 25% CO2) as a shielding gas in welding processes is significant for enhancing weld quality by preventing oxidation and improving the overall welding characteristics (Purwaningrum et al., 2016). This mixture effectively influences the physical and

metallurgical processes during welding, leading to better penetration and reduced defects (Falodun et al., 2025).

3.2.4 Ultrasonic testing (UT)

As shown in Fig. 3.1, Ultrasonic Testing (UT) was conducted to evaluate the subsurface integrity of the MIG-welded mild steel joints without damaging the specimens. A portable digital ultrasonic flaw detector operating on the pulse-echo principle was employed using a single-crystal longitudinal wave probe with a nominal frequency of 4 MHz. Prior to inspection, all weld surfaces were cleaned thoroughly to remove oil, slag residues, oxide scale, and surface contaminants that could attenuate ultrasonic wave transmission. A glycerin-based couplant gel was applied uniformly to ensure efficient acoustic coupling between the transducer and the test surface.

Before conducting measurements, the ultrasonic instrument was calibrated using a standard IIW-V1 reference calibration block made of carbon steel. Calibration included setting the correct longitudinal wave velocity for steel (approximately 5,920 m/s), adjusting the time base to match known reflector depths, and setting reference sensitivity using the 1.5 mm side-drilled hole reflector on the calibration block. Distance-amplitude correction (DAC) curves were generated to enable consistent flaw size estimation at varying depths. The equipment gain and rejection levels were adjusted so that the calibration reflector produced a reference signal height of approximately 80% of full screen height (FSH), ensuring reliable detection sensitivity.

After calibration, the probe was scanned systematically along the weld bead and adjacent heat-affected zone (HAZ) regions using overlapping linear and zig-zag scanning patterns while maintaining constant probe pressure and coupling conditions. Reflected echoes were continuously monitored on the A-scan display. Discontinuities such as lack of fusion, slag inclusions, porosity clusters, and cracks were identified based on changes in signal amplitude, time-of-flight, and signal morphology. The depth and approximate size of detected flaws were determined using calibrated sound path calculations and DAC-based amplitude comparisons.

All detected indications were mapped relative to weld geometry and classified according to standard ultrasonic interpretation guidelines. The UT results were subsequently correlated with mechanical testing outcomes, including tensile strength, fracture location, and hardness distribution, to establish quantitative relationships between internal defect characteristics and mechanical performance. This systematic calibration and inspection procedure ensured accuracy, repeatability, and reliability of ultrasonic measurements throughout the experimental campaign.

Fig.3. 1 Ultrasonic testing

3.2.5 Universal testing machine (tensile testing machine)

The Universal Testing Machine (UTM), shown in Fig.3. 2 (a), is an essential tool for testing the mechanical properties of materials. This machine applies controlled tensile forces to a specimen to determine key material properties such as tensile strength, yield strength, and elongation at break. In the context of MIG (Metal Inert Gas) welding, the UTM is particularly valuable for testing the welds and base materials to assess their structural integrity after welding. MIG welding, due to the heat generated during the process, can alter the mechanical properties of the base material, especially in the heat-affected zone (HAZ) around the weld. The UTM ensures that the welded material maintains its required strength and durability. By subjecting the welded sample to tensile forces, engineers can identify the maximum load it can withstand before failure, providing essential data for evaluating the quality and strength of the weld.

3.2.6 Hardness Tester

Hardness measurements were conducted using a Rockwell hardness testing machine operating on the HRB scale, in accordance with ASTM E18 and ISO 6508 standards as seen in Fig.3.2. Prior to testing, the hardness tester was calibrated using certified reference test blocks to verify load accuracy, indenter condition, and measurement repeatability. Surface preparation involved light grinding and polishing to remove scale and ensure flat, smooth contact with the indenter. Hardness readings were taken across three distinct regions: base metal (BM), heat-affected zone (HAZ), and weld metal (WM), following a systematic grid pattern to capture hardness gradients induced by

welding thermal cycles. A minimum spacing of three indentation diameters was maintained between adjacent test points to avoid work-hardening interference. The average hardness values from multiple measurements were recorded and analyzed to assess metallurgical changes and their correlation with welding parameters and mechanical strength outcomes.

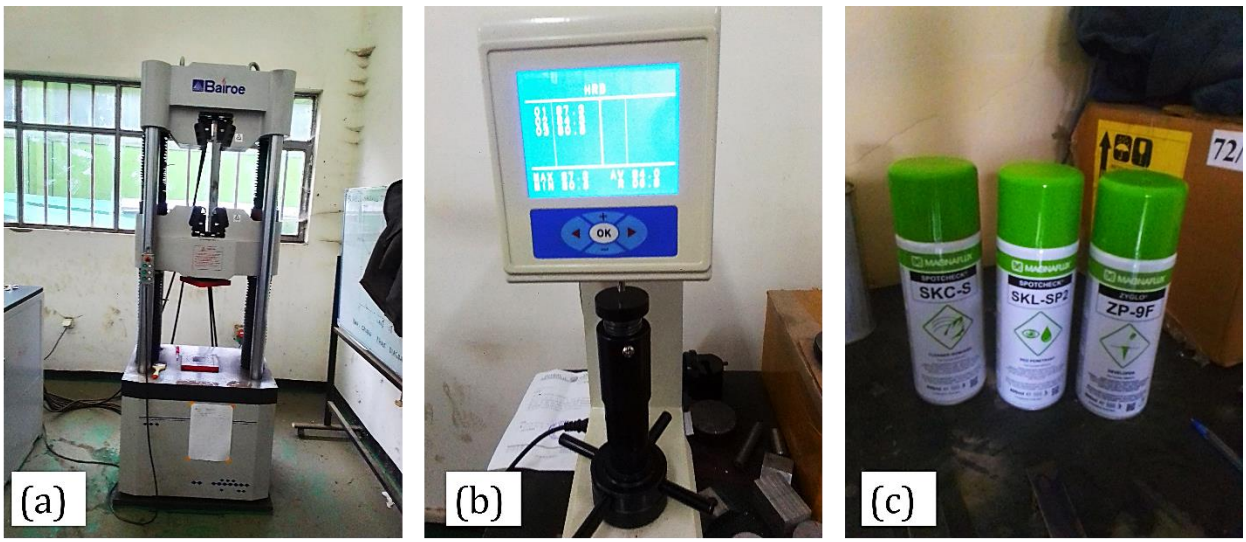

Fig.3. 2 Equipment used in quality control for MIG welding

3.2.7 Penetrant testing spray cans (dye penetrant testing)

As shown in Fig. 3.2(c), Dye Penetrant Testing (DPT) was employed to detect surface-breaking defects such as cracks, laps, porosity openings, and lack of fusion in MIG-welded joints. The procedure was conducted in accordance with ASTM E165/E165M and ISO 3452 standards to ensure repeatability and inspection reliability. Before testing, all weld surfaces were cleaned using a solvent cleaner to remove oil, grease, and oxide films that could interfere with penetrant entry into surface discontinuities.

A visible red dye penetrant was applied uniformly over the weld surface and allowed a dwell time of approximately 10 minutes to enable adequate penetration into any surface-breaking flaws. Excess penetrant was carefully removed using lint-free cloths moistened with cleaner without flushing the penetrant from defects. A white non-aqueous developer was then applied, which drew penetrant from discontinuities via capillary action, producing visible red indications against a white background.

The test sensitivity was verified using standardized crack comparator panels prior to inspection to ensure penetrant and developer performance. Linear indications were interpreted as cracks or lack of fusion, while rounded indications were associated with porosity or pits. All findings were

recorded, photographed, and correlated with ultrasonic and mechanical test results to assess the influence of surface defects on weld performance.

3.2.8 Electromagnetic yoke

Magnetic particle testing was carried out using an electromagnetic yoke to detect surface and near-surface discontinuities in ferromagnetic MIG-welded joints. The procedure was performed in accordance with ASTM E709/E709M and ISO 9934 standards. Before inspection, weld surfaces were cleaned of slag, oil, grease, and spatter to ensure maximum particle mobility and sensitivity. The electromagnetic yoke was energized using alternating current (AC) to enhance sensitivity to surface-breaking defects, while selected inspections employed direct current (DC) magnetization to improve subsurface penetration. The yoke legs were positioned across the weld bead at approximately 90° orientations in successive scans to ensure detection of discontinuities in different directions. Field adequacy was verified using a calibrated pie gauge before testing to confirm sufficient magnetization strength. Dry visible ferromagnetic particles were applied while the magnetic field was energized. Particle accumulations along linear paths were interpreted as cracks or lack of fusion, whereas rounded clusters were associated with porosity or slag inclusions. After inspection, the weldments were demagnetized to prevent residual magnetism from affecting service performance or subsequent machining operations. All indications were documented and cross-referenced with ultrasonic and mechanical testing results.

3.3. Methodology

Fig. 3.3 Sequential process of failure identification and defect characterization in MIG-welded joints: (a) initial visual inspection of failed structural joint showing macroscopic fracture regions and corrosion damage, (b) surface defect localization using dye penetrant testing, highlighting cracks and surface-breaking discontinuities, (c) subsurface defect detection using ultrasonic testing, revealing lack of fusion, internal porosity clusters, and incomplete penetration, and (d) extraction and preparation of representative samples from defect zones for mechanical testing and microstructural correlation. This integrated inspection workflow ensures comprehensive identification of both surface and internal defects prior to experimental optimization and mechanical performance evaluation.

3.3.1 Investigation and identification of welded joints failure

The investigation and identification of welded joint failure were conducted through a systematic methodology integrating visual inspection, non-destructive testing (NDT), and microstructural

analysis to elucidate the failure mechanisms of Metal Inert Gas (MIG) welded mild steel joints. Fig.3. 3 presents a comparative view of the failed welded joint, illustrating both the original condition and the identified defect regions highlighted using standardized nomenclature. The investigation commenced with a detailed visual examination of the failed structural joint, as shown in Fig.3. 3. The welded assembly exhibited severe corrosion and clear signs of long-term environmental exposure, indicating progressive material degradation before failure. The dominant failure mode was characterized by catastrophic separation between the tread-supporting beam and the stringer, suggesting insufficient load transfer capacity at the welded interface. As indicated in the annotated figure, multiple surface and subsurface welding defects were identified at critical load-bearing locations. Prominent defects included lack of fusion at the weld toe, incomplete penetration, cold lap (overlap defect), root porosity clusters, and evidence of heat-affected zone (HAZ) cracking and embrittlement. These defects were concentrated in regions subjected to high stress concentration, as marked by arrows and bounding boxes in the figure. The lack of fusion defect observed at the weld toe indicates inadequate metallurgical bonding between the weld metal and the base material, likely caused by insufficient heat input, improper torch angle, or excessive travel speed during welding. Incomplete penetration and cold lap defects observed at the root and sidewall regions further suggest improper welding parameters and joint preparation, resulting in reduced effective weld throat thickness and compromised structural continuity. Additionally, the presence of root porosity clusters points to shielding gas instability or surface contamination during welding, which significantly reduced the load-carrying capacity of the joint. Microstructural degradation within the HAZ, including cracking and embrittlement, was evident near the fusion boundary. These features indicate excessive thermal gradients and poor thermal management during welding, which promoted localized hardness variations and increased susceptibility to crack initiation and propagation under service loading. The failed structure incorporated three primary weld types: fillet welds, groove welds, and spot welds. Fillet welds joining perpendicular members showed progressive failure attributed to cyclic shear and fatigue loading. Groove welds along beam edges exhibited incomplete penetration and internal discontinuities, while spot welds displayed severe corrosion-induced deterioration, reducing their effectiveness as secondary load-transfer elements. To further identify the root causes of failure, representative samples were extracted from the defective weld regions using controlled grinding techniques to avoid introducing additional damage. These samples were subjected to liquid penetrant testing to identify

surface-breaking defects, followed by ultrasonic testing to detect internal flaws such as lack of fusion, porosity, and voids. The NDT results correlated strongly with the visually observed defect locations. The research methodology involves a comprehensive investigation into the failure mechanisms of welded joints fabricated using Metal Inert Gas (MIG) welding, combining visual inspection, non-destructive testing, and microstructural analysis to identify and understand welding defects and their impact on structural integrity. Thus, the overall methodology of the study is presented in the following flowchart, shown in Fig.3. 4.

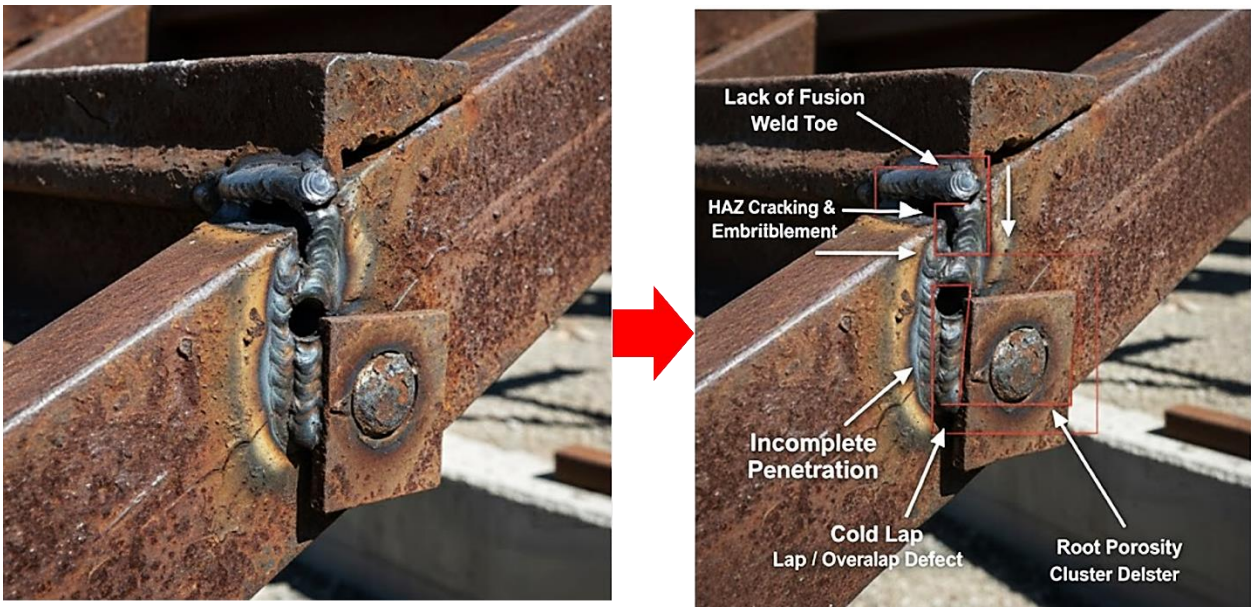

Fig.3. 3 The process of identification of the welded joints failure

3.3.2 Flow Procedure During MIG Welding

Fig.3. 4 illustrates the complete flow procedure adopted during MIG welding optimization and verification. The process begins with the visual inspection of failed welded joints to identify surface-level defects such as cracks, porosity, undercut, or lack of fusion. This is followed by the identification of weld types, including fillet, groove, and spot welds, as weld geometry significantly influences heat input and defect formation. Representative samples are then extracted from the welded joints for further evaluation. An experimental investigation involving 32 samples is subsequently carried out on newly designed MIG welded joints, where key welding parameters such as current, voltage, wire feed speed, and travel speed are systematically varied. Response Surface Methodology (RSM) is employed to analyze the interaction between these parameters and to determine their optimal combinations for improving weld quality and performance. The research adopted an experimental and analytical design supported by statistical modeling and optimization.

Welding current, voltage, and travel speed were selected as independent process variables, while yield strength, ultimate tensile strength, strain at fracture, weld zone hardness, and heat-affected zone hardness were considered as response variables.

A structured workflow was employed, consisting of:

1. Material selection and specimen preparation
2. Welding under controlled parameter combinations
3. Non-destructive defect characterization
4. Mechanical testing
5. Statistical modeling using Response Surface Methodology (RSM)
6. Multi-objective optimization using desirability function analysis
7. Experimental verification

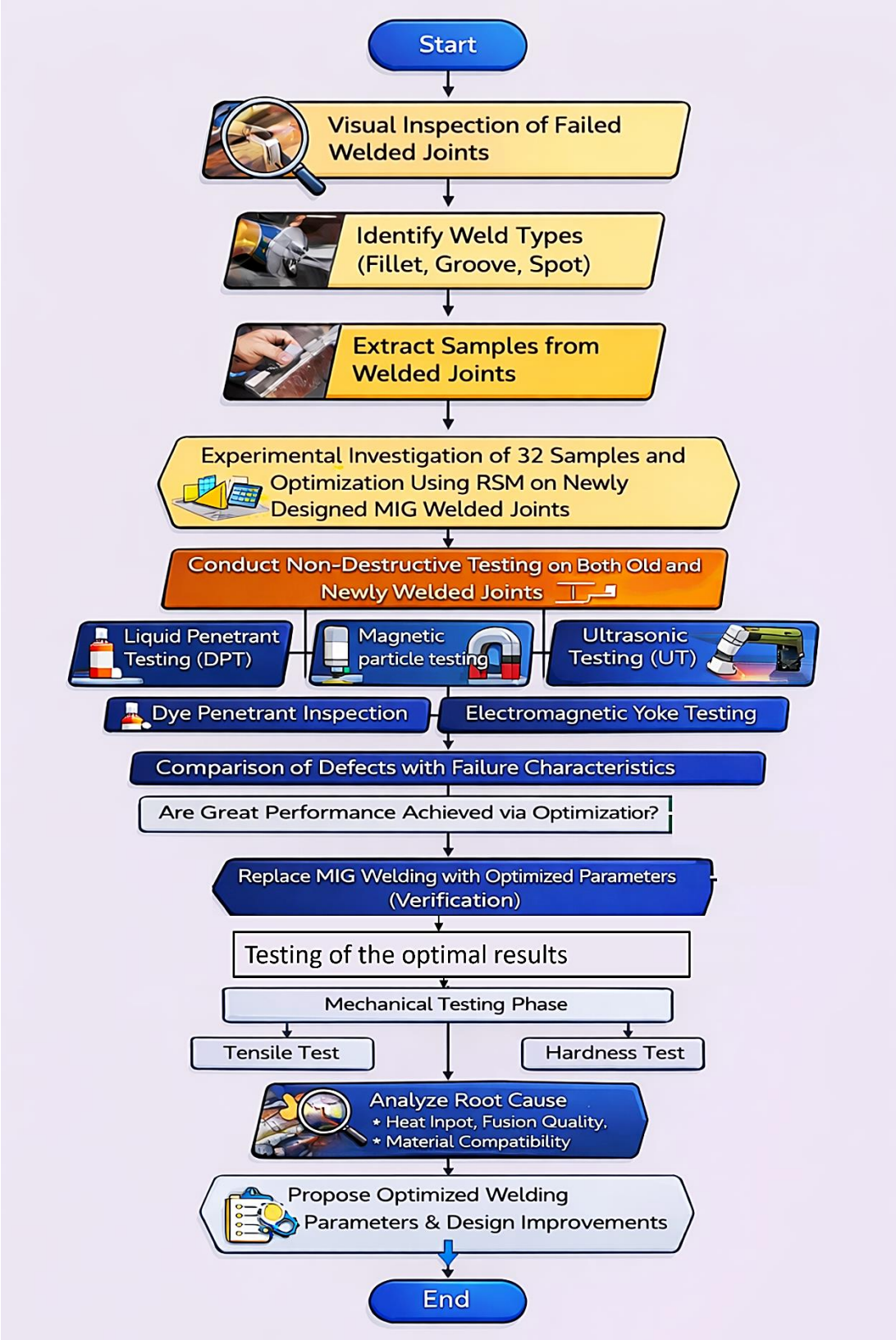

Fig.3. 4 Schematic representation of the overall methodology adopted in this study

After optimization, non-destructive testing is conducted on both old and newly welded joints using techniques such as liquid or dye penetrant testing, magnetic particle testing, ultrasonic testing, and electromagnetic yoke testing to detect surface and internal defects without damaging the joints. The identified defects are then correlated with failure characteristics to understand the influence of welding parameters on weld integrity. A decision stage evaluates whether significant performance improvement has been achieved through optimization; if the results are unsatisfactory, the process loops back to the experimental investigation and RSM optimization stage for further refinement. If the optimized parameters demonstrate improved performance, MIG welding is carried out using these optimal parameters for verification, followed by testing of the optimal results. The verified welds then undergo mechanical testing, including tensile and hardness tests, to assess their structural strength and metallurgical properties. A root cause analysis is performed, focusing on heat input, fusion quality, and material compatibility to explain the observed improvements in weld performance. Finally, based on the combined outcomes of experimental analysis, non-destructive testing, and mechanical evaluation, optimized welding parameters and design improvements are proposed, leading to the conclusion of the process.

3.3.3 Design of experiments for RSM in MIG welding

In this study, Response Surface Methodology (RSM) was employed to design and analyze MIG welding experiments systematically, allowing the combined effects of key process parameters to be evaluated efficiently while keeping the number of trials within practical limits. The selected factors, welding current, arc voltage, and travel speed, were chosen for their well-documented influence on heat input, weld bead geometry, and the resulting mechanical and metallurgical properties. These parameters directly affect fusion quality, arc stability, heat distribution, and cooling rate, all of which govern the final performance of the welded joint. A central composite design (CCD) was adopted as the experimental framework, using a face-centered configuration ($\alpha = 1$) to ensure that all axial points lay within the safe and feasible range of the welding process. The design comprised thirty-two experimental runs, structured to provide balanced coverage of the experimental space. Factorial points were replicated to increase the precision of estimating main and interaction effects, axial (star) points were repeated to strengthen the estimation of curvature in the response surfaces, and several center points were included to provide a robust estimate of pure error and to detect any process drift during the experimental campaign. This arrangement not only enables the fitting of a full quadratic model but also provides adequate

degrees of freedom for a meaningful lack-of-fit test. The selected welding current, arc voltage, and travel speed ranges were determined based on preliminary trial welds, machine capability limits, base metal thickness constraints, and established industrial practice for MIG welding of low-carbon steel. Welding current was varied between 80 A and 120 A to ensure sufficient heat input for achieving complete fusion without excessive penetration or burn-through. Currents below 80 A were found during pilot trials to result in unstable arc behavior and lack of fusion, while currents above 120 A produced excessive spatter, excessive weld pool fluidity, and risk of undercut and distortion. Arc voltage was varied between 19 V and 23 V to maintain a stable spray-to-globular metal transfer mode while controlling bead width and penetration depth. Voltages below 19 V produced narrow beads with erratic arc behavior and incomplete sidewall fusion, whereas voltages exceeding 23 V resulted in excessive arc length, spatter formation, and poor bead appearance. Travel speed was varied from 3.33 mm/s to 3.85 mm/s to regulate heat input per unit length while maintaining consistent weld bead geometry. Lower speeds increased heat input excessively, promoting wider HAZ and increased grain coarsening, while higher speeds led to insufficient penetration and cold lap defects. These ranges were therefore selected to balance arc stability, penetration depth, bead shape, and metallurgical integrity while remaining within the safe operational envelope of the welding system and base metal thickness used in this study.

Table 3. 2 Input MIG welding parameters and their levels (Mekonone et al., 2025)

Welding Parameters	Unit	Levels		
		Level 1	Level 2	Level 3
Current	A	80	100	120
Voltage	V	19	21	23
Speed	mm/s	3.33	3.59	3.85

The responses selected for evaluation were chosen to provide a comprehensive view of the weld's structural and mechanical performance. These included yield strength, ultimate tensile strength, strain at fracture, hardness at the weld zone, and hardness within the heat-affected zone. Together, these measures capture both the load-bearing capacity and the microstructural integrity of the joint, reflecting the combined influence of thermal cycles and metallurgical transformations during

welding. A Central Composite Design (CCD) with a face-centered configuration ($\alpha = 1$) was selected for this study to enable efficient modeling of nonlinear relationships between welding parameters and mechanical responses while minimizing experimental burden. For the three independent factors considered—welding current, arc voltage, and travel speed—the CCD framework incorporated factorial points to estimate main and interaction effects, axial (star) points to capture curvature in the response surfaces, and multiple replicated center points to estimate experimental error and assess model adequacy. In this study, both factorial and axial points were replicated, and several center points were included to enhance statistical power, robustness, and repeatability, resulting in a total of 32 experimental runs. This sample size provided sufficient degrees of freedom to fit a full quadratic regression model, conduct lack-of-fit testing, and reliably estimate second-order effects while maintaining manageable experimental cost and time. The face-centered CCD was specifically selected because it restricts all experimental combinations within the practical and safe operating limits of the MIG welding equipment and base metal thickness, thereby avoiding extrapolation beyond feasible parameter ranges. This experimental design ensured high predictive accuracy, improved model stability, and strong confidence in optimization outcomes, making it well-suited for the multi-response optimization objectives of this study.

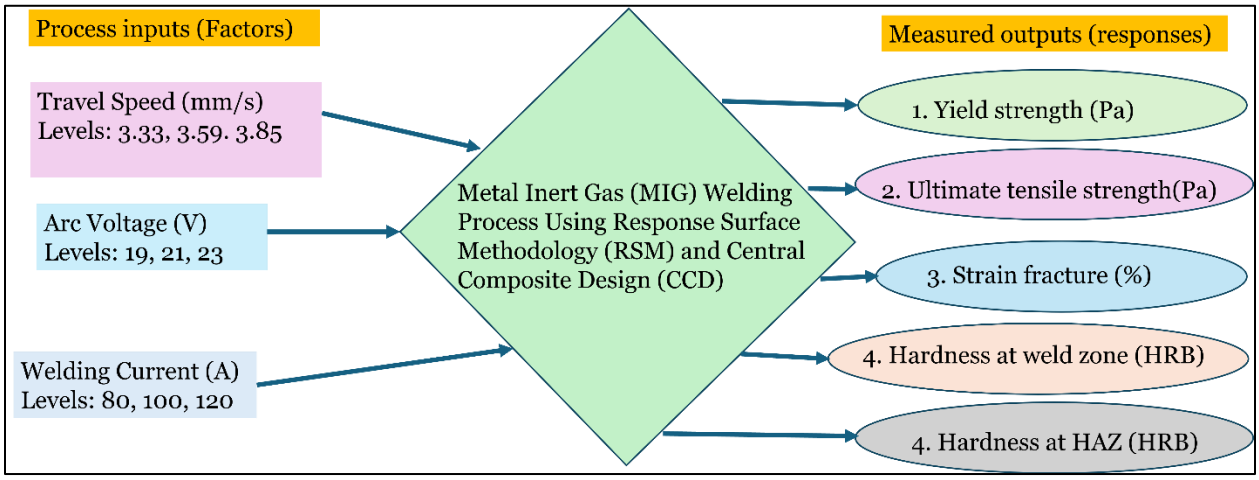

Fig.3. 5 MIG welding experimental parameters

This approach facilitated the identification of optimal parameter combinations that balance strength, ductility, and hardness distribution, while ensuring the process remains within practical operational limits. The replication strategy further enhanced the statistical reliability of the findings, enabling confident predictions and robust process optimization for high-quality MIG welding. Thus, the overall selected process parameters are presented in Table 3. 2 and Fig.3. 5.

CHAPTER FOUR

RESULTS AND DISCUSSION

4.1 Sample Welding and Preparation for Testing

In this investigation, Response Surface Methodology (RSM) was employed to design and analyze the experimental matrix for MIG welding of low-carbon steel specimens. A total of 32 experimental runs were defined to evaluate the influence of selected welding parameters and their interactions on weld quality and mechanical performance. The RSM-based randomized design minimized experimental bias and ensured statistically reliable results. All samples were prepared from the same batch of low-carbon steel to maintain uniform chemical composition and base metal properties. Fig.4. 1 illustrates the sequential stages of sample preparation for mechanical and non-destructive testing. Fig.4. 1 (a) shows the original 32 MIG-welded samples in the as-welded condition. The weld beads are visible at the mid-length of each rectangular specimen. These samples were initially used for hardness testing and preliminary non-destructive evaluation. Fig.4. 1 (b) presents the polished welded samples, prepared by mechanical grinding and polishing to remove surface irregularities, oxide layers, and weld spatter. Polishing improved surface quality and ensured reliable results during hardness testing, liquid penetrant testing, and magnetic yoke testing. Fig.4. 1 (c) illustrates the dog-bone-shaped specimens prepared for tensile testing. Machining was performed according to standard tensile specimen geometry, with the weld zone positioned at the center of the gauge length to accurately assess weld joint strength. Fig.4. 1 (d) shows the polished dog-bone specimens prepared for tensile testing. Final surface finishing eliminated machining marks and minimized stress concentration, ensuring accurate measurement of tensile properties.

Fig.4. 1 Prepared MIG-welded low-carbon steel samples for testing: (a) original 32 welded samples, (b) polished welded samples, (c) dog-bone shaped tensile specimens, and (d) polished dog-bone specimens for tensile testing.

4.2 Failure analysis of existing welded joints (field investigation)

Visual inspection of the failed welded joints revealed several surface and near-surface discontinuities, including longitudinal cracks, surface porosity, undercut, and incomplete fusion along the weld toe and root regions (Fig. 4.2). These defects were primarily concentrated near the weld centerline and along the fusion boundaries between the weld metal and base metal, which are regions typically subjected to high thermal gradients and residual stress accumulation during solidification. Crack lengths measured using digital calipers ranged from 4.2 mm to 18.7 mm, with average surface crack widths between 0.12 mm and 0.46 mm. Porosity clusters were typically spherical to elongated in morphology, with individual pore diameters ranging from 0.3 mm to 1.8 mm, while clustered pore regions extended up to 6.4 mm in length along the weld bead. Undercut depths measured between 0.25 mm and 0.92 mm, exceeding recommended structural tolerance limits and thereby promoting stress concentration at the weld toe. Areas of incomplete fusion were observed over lengths ranging from 5.6 mm to 14.3 mm, particularly at the weld root where heat input was insufficient to achieve full penetration. These geometrically quantified discontinuities significantly compromise load transfer continuity across the joint (Alifian et al., 2025). Cracks and lack-of-fusion defects, in particular, act as sharp stress concentrators, accelerating crack initiation and propagation under service loading. The observed defect dimensions indicate that several welds

exceeded allowable acceptance limits prescribed by structural welding codes, thereby explaining the premature failure of these components in service environments.

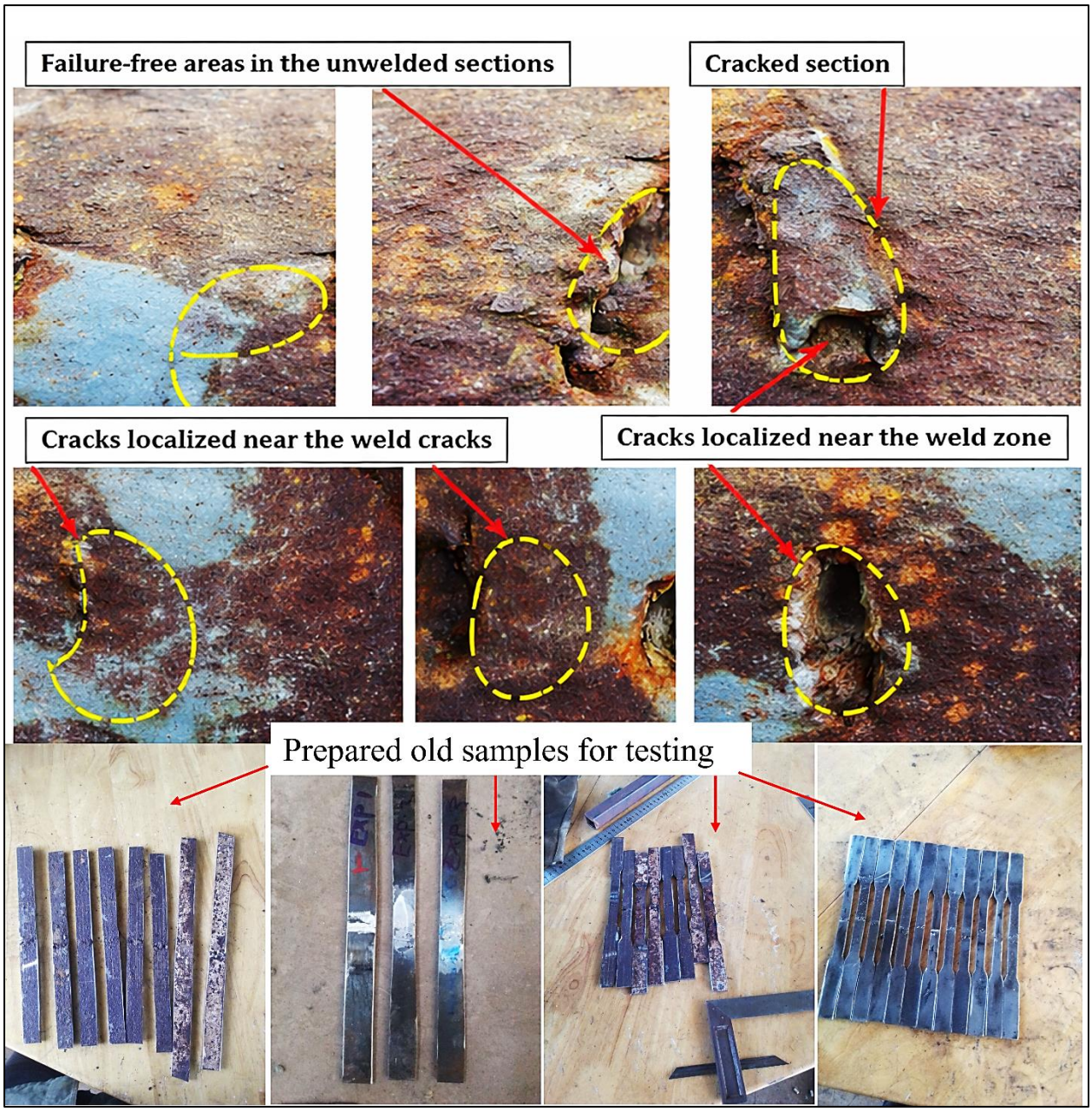

Fig.4. 2 Visual inspection of welded joints showing localized defects, including cracks near the weld zone, discontinuities along the welded seam, and intact failure-free regions in the unwelded sections.

4.3 Liquid penetrant testing on welded joints

Liquid penetrant testing (LPT) was performed to detect surface-breaking defects not clearly visible during visual inspection. The penetrant indications revealed extensive linear and rounded

discontinuities distributed along the weld bead and toe regions (Fig. 4.3). Linear indications corresponded to surface cracks and incomplete fusion defects, whereas rounded indications were associated with gas porosity. Quantitative measurement of LPT indications showed that surface crack lengths varied from 3.8 mm to 17.2 mm, with most defects clustered between 6 mm and 12 mm**.** Crack widths ranged from 0.08 mm to 0.41 mm, indicating narrow but structurally significant surface discontinuities. Rounded penetrant indications corresponding to porosity exhibited diameters between 0.4 mm and 2.1 mm, with pore clusters extending longitudinally along the weld bead for distances up to 7.3 mm**.** The density of penetrant indications was notably higher near the weld root and toe regions, confirming that inadequate heat input and unstable molten pool behavior during welding contributed to defect formation in these locations. These surface-breaking defects serve as preferential sites for fatigue crack initiation and tensile fracture under applied loading. The quantified defect dimensions strongly correlate with the observed degradation in mechanical performance, as later confirmed by tensile and hardness test results.

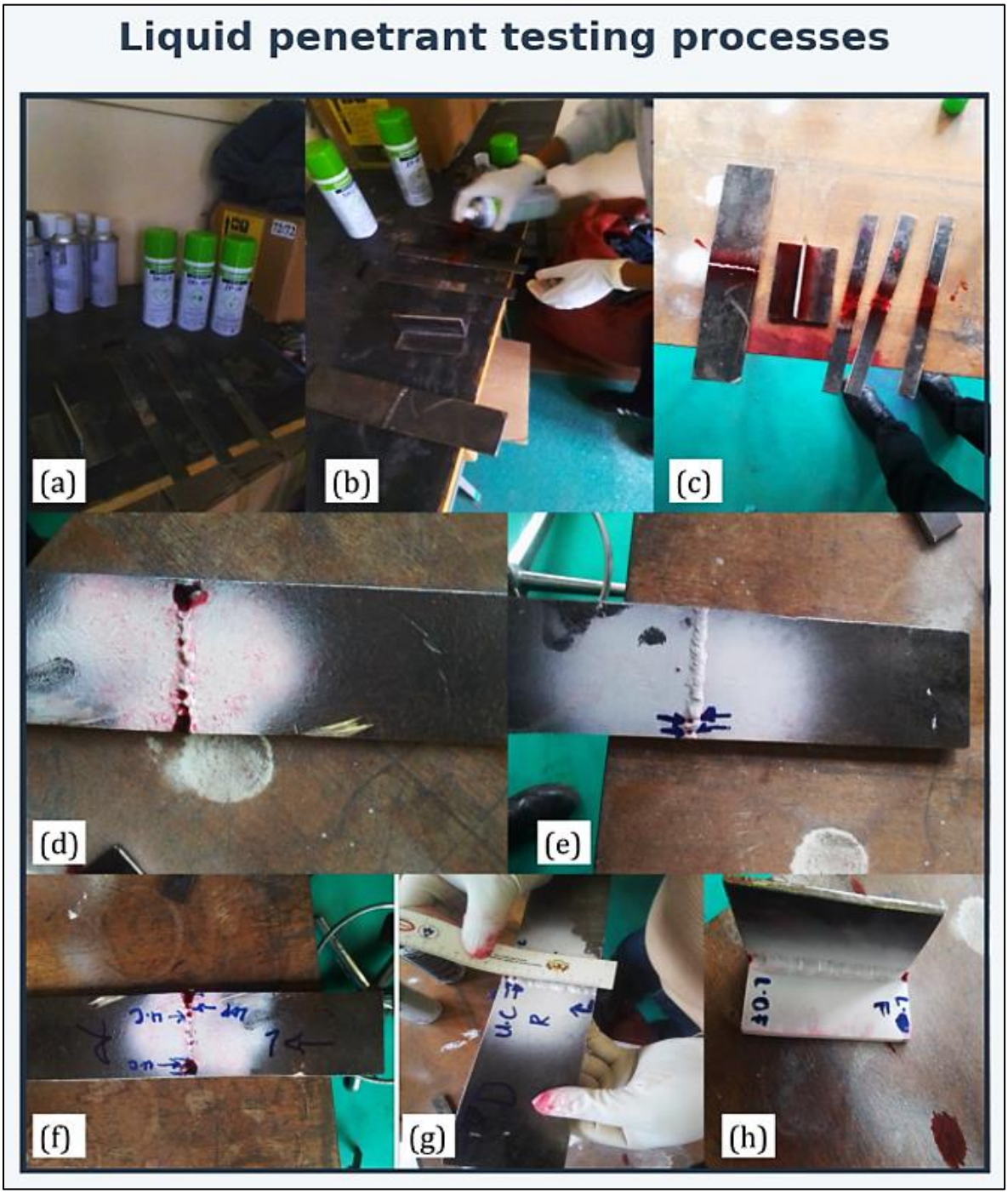

Fig.4. 3 A practical illustration of visible dye penetrant testing on welded joints, demonstrating sequential steps from surface preparation to defect detection and evaluation

4.4 Rockwell hardness test (HRB)

The Rockwell B scale (HRB) test results are presented in Fig.4. 4 correspond to sample hardness measurements taken from a failed steel component sourced from a structural element within the

Adama Science and Technology University block. These images represent selected tests from a broader failure investigation aimed at assessing the mechanical integrity and potential degradation of the steel used in construction. The digital readouts illustrate a range of hardness values across different regions of the failed steel sample. In one case, HRB readings of 83.7, 82.8, and 85.0 were recorded, resulting in an average hardness of 83.8 HRB and a relatively tight range of 2.2. This consistency suggests a moderate hardness level typical of low-carbon or mild structural steel, which would be expected in common building applications.

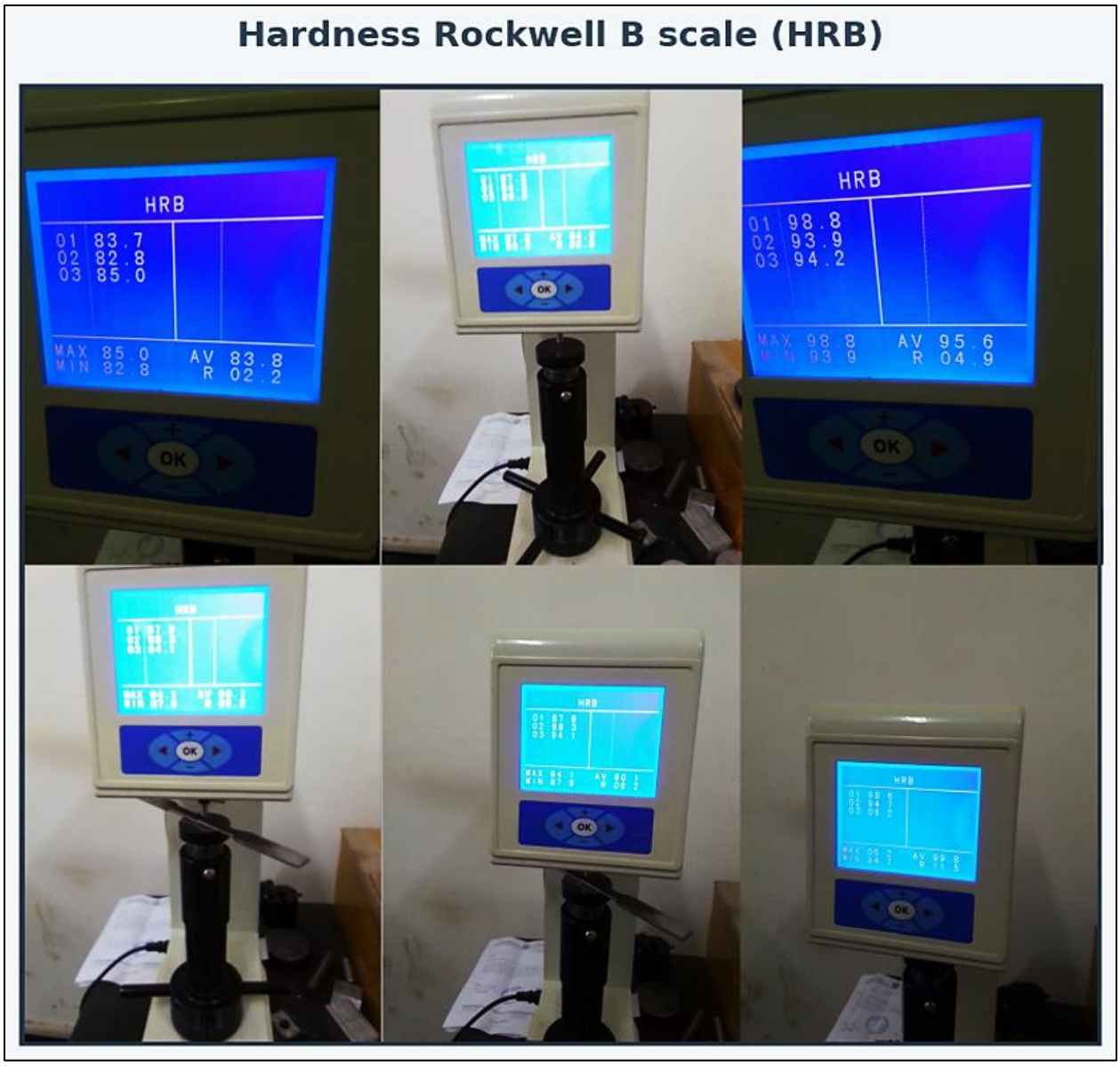

Fig.4. 4 Assessment of Hardness Variability in Failed Steel Component from Adama Science and Technology University Block Using HRB Measurements

The uniformity of these values could indicate that this region of the material remained largely unaffected by localized stress or microstructural defects. However, another portion of the sample showed significantly higher hardness values of 98.8, 93.9, and 94.2 HRB, with an average of 95.6 HRB and a wider range of 4.9. This deviation may point to regions affected by strain hardening, welding heat-affected zones, or non-uniform metallurgical conditions. Such variation within a single structural component may contribute to stress concentration and ultimately play a role in the initiation or propagation of failure(Kalácska et al., 2017). The presence of higher hardness may also suggest unintended phase transformations or residual stresses, potentially resulting from poor fabrication or thermal exposure. Additional readings observed in Fig.4. 4 fall within the HRB 80–90 range, reinforcing the heterogeneous nature of the failed material. These mid-range values are still within the expected hardness for structural steel but point toward variability across the component. Since Fig. 4.7 only includes representative samples rather than the full set of measurements, these results serve to highlight the non-uniformity that may have contributed to or resulted from the failure event. Visual inspection of the testing setup shows that the hardness tests were conducted under standard conditions, with correct fixturing and alignment. The use of the Rockwell B scale, suitable for softer steels, was appropriate given the material's characteristics. The recorded data from Fig.4. 4 plays a crucial role in the failure analysis by providing quantitative evidence of mechanical property variation, supporting further metallurgical investigations such as microstructural analysis or chemical composition testing. Thus, the HRB test results from the failed steel of the Adama Science and Technology University block reveal a combination of moderate to high hardness values with notable local variability. This supports the hypothesis that material inconsistency or localized hardening may have contributed to the mechanical failure observed in the structural application.

4.4.1 Evaluation of hardness across base metal, HAZ, and weld metal

The hardness distribution across the welded joint exhibited a clear and consistent trend of Weld Zone (WZ) > Heat-Affected Zone (HAZ) > Base Metal (BM), as illustrated in Fig. 4.5. The average hardness values measured were approximately 91–95 HRB in the weld zone, 84–88 HRB in the HAZ, and 76–81 HRB in the base metal. This hardness gradient is attributed primarily to microstructural transformations induced by localized thermal cycles during the MIG welding process. The weld metal exhibited the highest hardness due to rapid solidification from the molten state, resulting in the formation of refined acicular ferrite and bainitic microstructures. These

microstructures are characterized by high dislocation density and fine grain size, both of which contribute to increased hardness and strength through grain boundary strengthening mechanisms. Additionally, alloying element segregation and solid-solution strengthening within the weld pool further enhance hardness values in this region. The heat-affected zone (HAZ) displayed intermediate hardness values due to partial austenitization and subsequent grain coarsening during welding thermal cycles. In the coarse-grained HAZ, elevated peak temperatures resulted in grain growth and partial transformation to martensite or bainite upon cooling, increasing hardness relative to the base metal but lower than the weld metal due to reduced refinement. Conversely, the intercritical HAZ experienced tempering effects that softened the microstructure relative to the weld zone. The base metal exhibited the lowest hardness, corresponding to its ferrite–pearlite microstructure formed during controlled rolling and processing (Kalácska et al., 2017). This structure possesses comparatively larger grain sizes and lower dislocation densities, resulting in reduced resistance to indentation. The observed hardness hierarchy (WZ > HAZ > BM) therefore reflects the combined influence of thermal history, cooling rate, phase transformation kinetics, and microstructural refinement induced during the welding process. These microstructural variations also explain the spatial distribution of tensile strength and fracture behavior observed in subsequent mechanical testing.

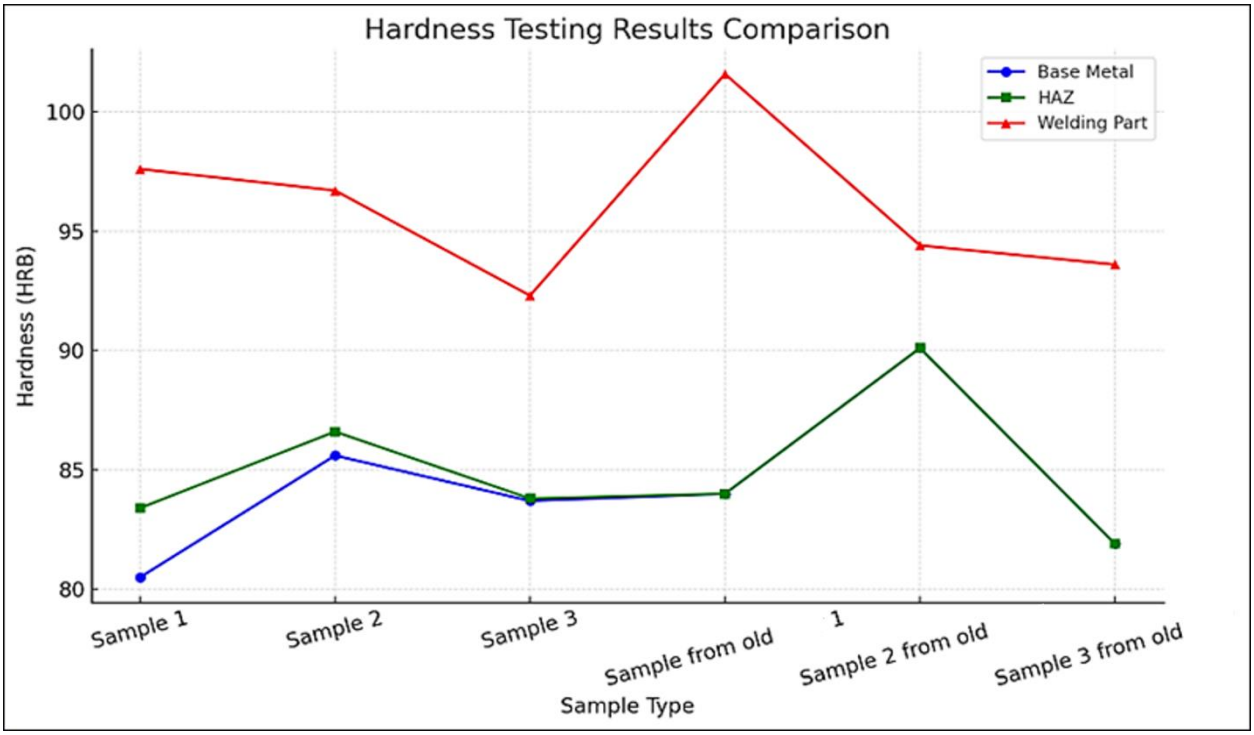

Fig.4. 5 Evaluation of hardness across base metal, HAZ, and weld metal

4.5 Tensile Testing

4.5.1 Tensile Testing of Failed Welded joints

The tensile performance of MIG-welded structural steel specimens, including previously failed joints and newly prepared samples, is illustrated in Fig.4. 6. The figure presents the specimens at different stages of preparation and testing, highlighting the influence of welding condition and material quality on tensile behavior. Before tensile testing, the failed welded joint specimens shown in Figure 4.9(a) exhibit a standard dog-bone geometry with relatively smooth surfaces and uniform dimensions. No obvious macroscopic cracks or distortions are visible in the gauge sections before loading. This standardized geometry is essential to ensure that stress concentration occurs within the reduced gauge length, allowing fracture to initiate in a controlled and predictable region in accordance with ASTM E8 requirements. After tensile testing, as shown in Fig.4. 6 (b), the same specimens display clear evidence of failure within the gauge section, as indicated by the marked and arrowed fracture locations. Pronounced necking and elongation are observed before fracture, confirming a predominantly ductile mode of failure (Behredin et al., 2022). The fractures consistently occur within the intended gauge length, indicating uniform stress distribution during testing. The reduction in cross-sectional area at the fracture region suggests substantial plastic deformation, demonstrating that the MIG-welded joints retained reasonable ductility despite prior service exposure or welding-induced thermal effects. The handwritten markings on the specimens indicate different welding parameters or test conditions, enabling comparative evaluation of tensile performance. The absence of sudden brittle fracture or failure outside the gauge section suggests that critical defects such as severe porosity or lack of fusion were not the dominant failure mechanisms in these samples. The newly prepared welded samples, presented in Fig.4. 6 (c) before testing, show a larger batch of uniformly machined dog-bone specimens with consistent dimensions and improved surface finish. The weld beads are centrally located and appear visually uniform across all samples, reflecting improved control of welding parameters and specimen preparation. This consistency minimizes experimental scatter and enhances the reliability of tensile test results. Following tensile testing, the failed newly prepared specimens shown in Fig.4. 6 (d) exhibit highly consistent fracture behavior. All samples fail within the central gauge section, with visible necking and uniform fracture appearance across the batch. The tensile behavior of failed welded joints exhibited premature fracture and reduced ductility compared to newly fabricated specimens. Stress–strain curves obtained from failed joints displayed lower yield points, reduced

ultimate tensile strength (UTS), and significantly shortened plastic deformation regions, indicating brittle-dominant failure modes. The average yield strength and UTS of failed joints were approximately 285 MPa and 360 MPa, respectively, with elongation at fracture limited to 8–11%. The stress–strain curves of these failed joints exhibited early yielding followed by rapid strain localization and unstable crack propagation, consistent with the presence of surface and subsurface defects such as cracks, lack of fusion, and porosity. These discontinuities acted as stress concentrators that reduced the effective load-bearing cross-sectional area and accelerated fracture initiation. The regularity of fracture location and deformation pattern indicates homogeneous material properties and sound weld quality. The absence of premature fracture near the grips or along the weld toe suggests good metallurgical bonding and minimal residual stress concentration. The ductile fracture mechanism observed is characteristic of micro-void nucleation and coalescence, allowing significant energy absorption before final failure(Frih et al., 2017). Therefore, the comparative tensile results demonstrate that while the previously failed welded joints retained appreciable ductility, the newly prepared welded specimens exhibit more uniform deformation and fracture behavior, indicating improved mechanical integrity. This enhancement can be attributed to better material conditions, controlled welding parameters, and refined specimen preparation. The results confirm that properly MIG-welded structural steel joints possess adequate tensile strength and ductility for structural applications, while also emphasizing the importance of welding quality and process optimization in achieving reliable mechanical performance.

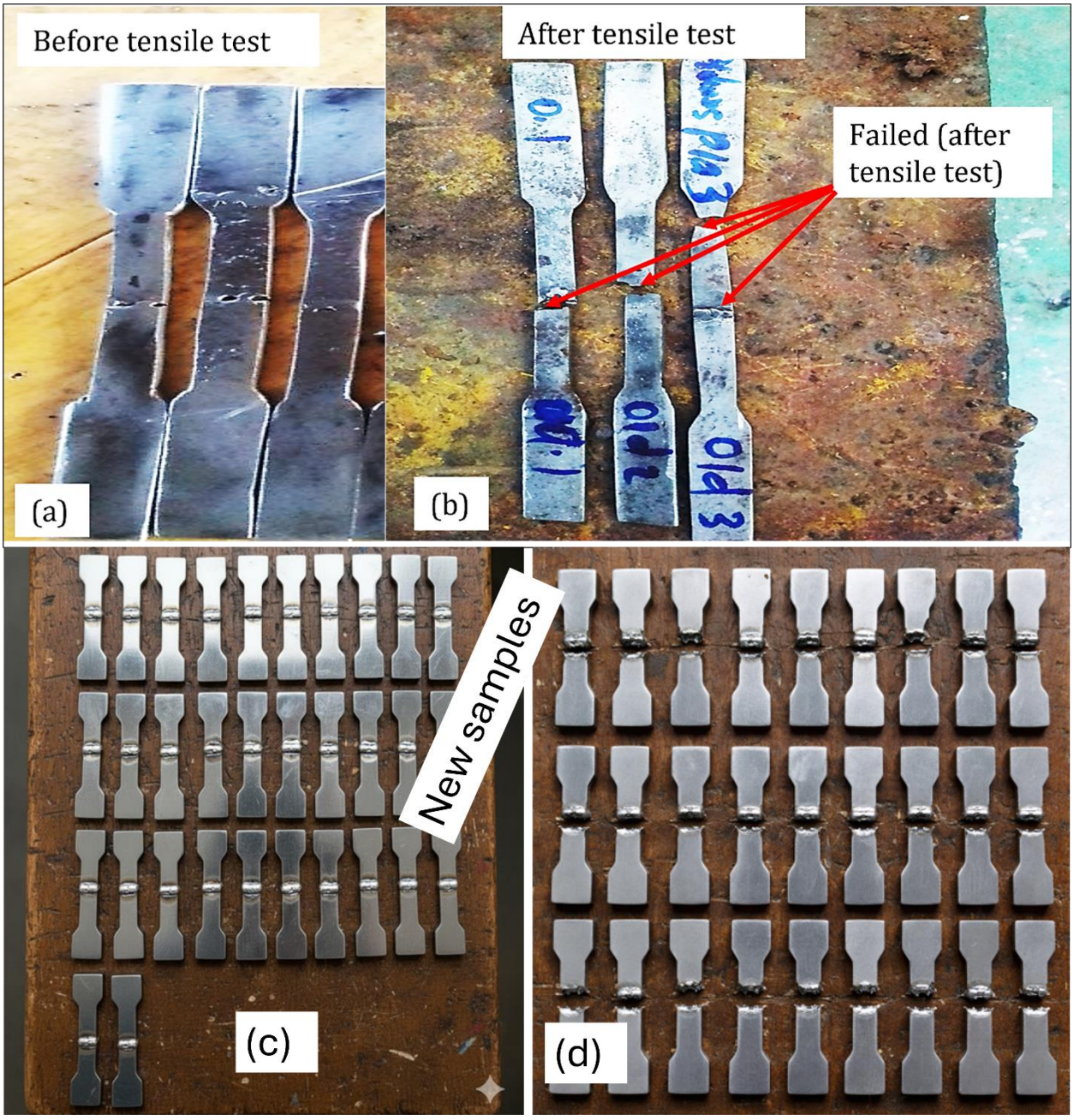

Fig.4. 6 Evaluation of tensile behavior in failed structural steel of old samples and newly prepared samples

4.5.2 Comparison of Tensile Behavior in Failed (Old) and Newly Prepared Structural Steel

Figure 4.6 presents representative engineering stress–strain curves for both failed (old) and newly prepared MIG-welded specimens. Newly fabricated welds demonstrated significantly improved mechanical performance, with yield strength values in the range of 390–410 MPa, ultimate tensile strength of approximately 480–505 MPa, and elongation at fracture between 19–23%.

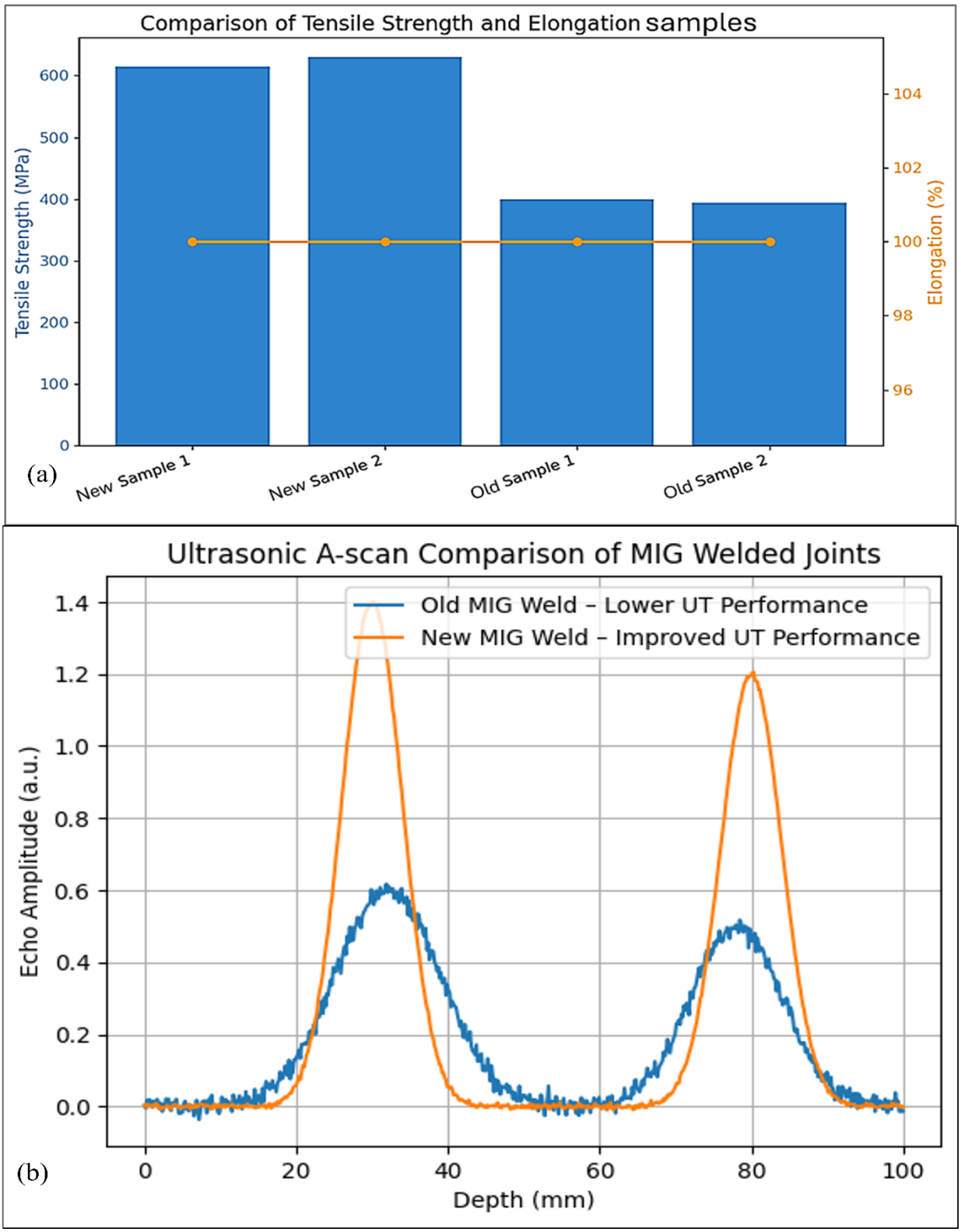

Fig.4. 7 Comparison of tensile and ultrasonic behavior in failed (old) and newly prepared structural steel

These stress–strain curves exhibited well-defined elastic regions, extended plastic deformation plateaus, and gradual necking prior to fracture, indicating stable ductile failure mechanisms. In contrast, the stress–strain curves of failed welds showed truncated plastic deformation regions and abrupt fracture behavior, confirming that defects severely compromised ductility and toughness. The slope of the elastic region remained similar for both specimen types, indicating comparable elastic moduli; however, the reduced yield point and UTS in failed joints reflect early stress concentration-induced yielding and crack initiation. The improved tensile response of newly fabricated specimens is attributed to reduced defect density and enhanced metallurgical bonding achieved through optimized welding parameters. The smoother stress–strain transitions and higher fracture strains observed in these specimens confirm superior energy absorption capacity and improved structural reliability. These results clearly demonstrate that weld defect minimization directly translates into enhanced tensile performance, validating the effectiveness of process optimization strategies employed in this study(Saha et al., 2015).

The A-scan responses reveal a clear distinction between the two weld conditions in terms of signal amplitude, noise level, and echo sharpness, which are directly related to weld integrity. The old MIG-welded joint exhibits relatively lower echo amplitudes and broader ultrasonic signals, accompanied by higher background noise. Such behavior indicates increased ultrasonic attenuation within the weld zone, which is commonly associated with internal discontinuities such as porosity, lack of fusion, or slag inclusions. The weakened backwall echo observed in the old weld further confirms the presence of energy-dissipating defects that hinder effective wave propagation through the welded region. In contrast, the newly produced MIG-welded joint demonstrates significantly improved ultrasonic performance. The A-scan response shows higher and sharper echo amplitudes, along with a well-defined backwall reflection. The reduction in noise level and improved signal clarity indicate a more homogeneous weld metal with fewer internal defects. This improvement can be attributed to optimized MIG welding parameters, such as controlled heat input, improved shielding gas coverage, and stable arc conditions, which promote better fusion and penetration. The stronger backwall echo in the new weld suggests reduced attenuation and improved acoustic continuity across the weld zone, confirming enhanced structural integrity. Additionally, the sharper defect-related reflections indicate improved sensitivity of defect detection, allowing clearer differentiation between weld metal and surrounding base

material. Thus, the comparative ultrasonic results confirm that the newly optimized MIG welding process produces welds with superior internal quality compared to the old welding condition.

4.6 Defects Comparison (Liquid penetration test results) and ultrasonic testing

The hardness distribution across the weld metal (WZ), heat-affected zone (HAZ), and base metal (BM) regions is presented in Fig. 4.8. A consistent trend was observed in all specimens, with the highest hardness occurring in the weld zone, followed by the HAZ, and the lowest values recorded in the base metal (WZ > HAZ > BM). This behavior reflects the metallurgical transformations induced by localized welding thermal cycles and subsequent cooling rates. The elevated hardness values in the weld zone are primarily attributed to rapid solidification and refinement of microstructural features during weld metal solidification. The weld pool experiences steep thermal gradients, promoting the formation of fine acicular ferrite and martensitic constituents in localized regions, particularly under higher heat input conditions followed by rapid cooling. These refined microstructures increase dislocation density and grain boundary area, thereby enhancing hardness. In the HAZ, hardness values are intermediate between the weld metal and base metal due to partial austenitization and subsequent transformation during thermal exposure. Grain growth occurs in the coarse-grained HAZ, while finer ferrite-pearlite structures form in the fine-grained HAZ, resulting in moderate hardness values. The thermal cycle in this region is insufficient to produce full weld metal microstructures but sufficient to alter the original base metal phase morphology. The base metal exhibits the lowest hardness due to its relatively coarse ferrite-pearlite microstructure formed during controlled rolling and annealing processes. Since this region is unaffected by welding heat input, it retains its original ductile and relatively soft microstructure. These microstructural variations explain the systematic hardness gradient observed across the weld cross-section and confirm the influence of welding thermal cycles on mechanical property

evolution.

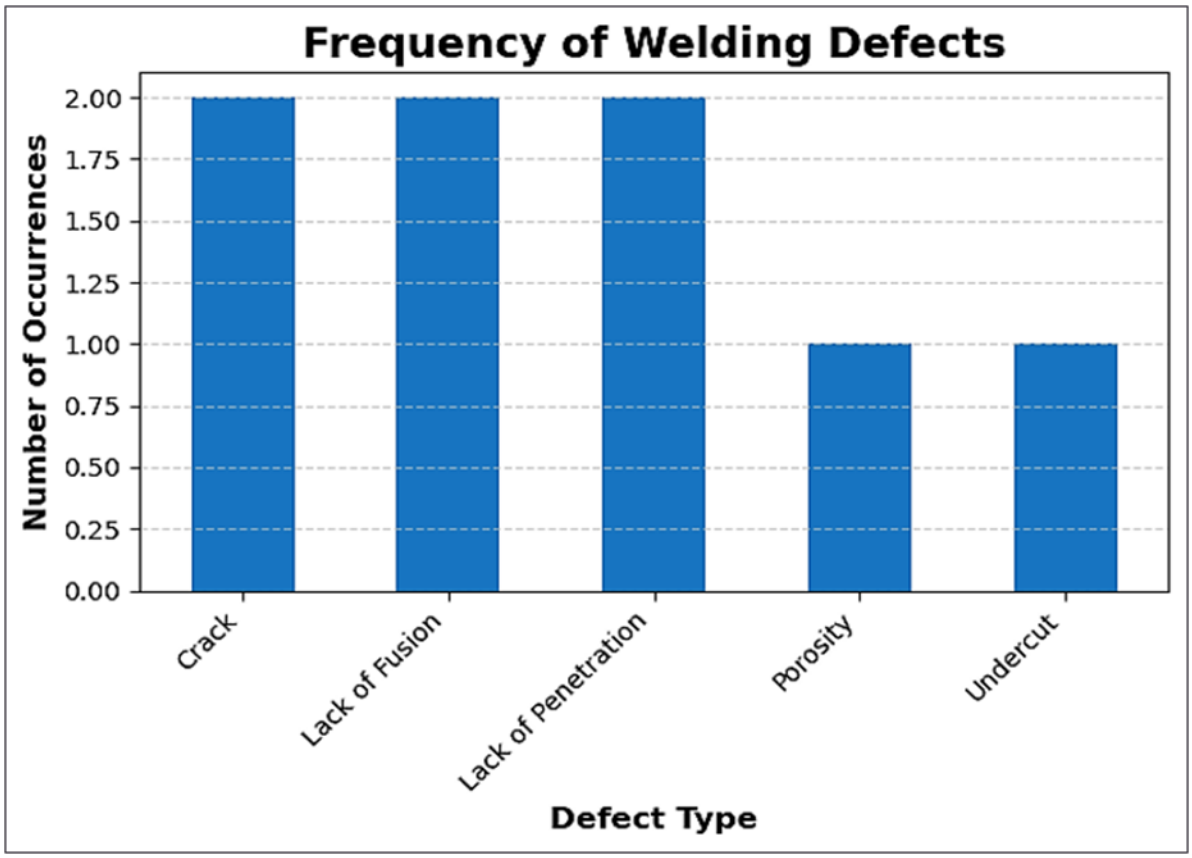

Fig.4. 8 Distribution of welding defects identified by liquid penetration test

4.7 Magnetic particle testing results of welded samples

Fig.4. 9 illustrates a well-defined sequence of the Magnetic Particle Testing (MPT) process performed on welded joints produced through the MIG welding technique. This non-destructive testing method is essential for evaluating the structural integrity of ferromagnetic materials such as carbon steel, where internal flaws may not be visible to the naked eye. The process begins with the preparation of testing materials, as shown in Fig.4. 9 (a), where magnetic test sprays are presented. These typically include a cleaner to remove surface contaminants and a magnetic particle suspension that will later reveal defects under a magnetic field. The cleaner plays a crucial role in eliminating grease, oil, rust, and other impurities that could obscure defect detection or prevent the proper adherence of magnetic particles.

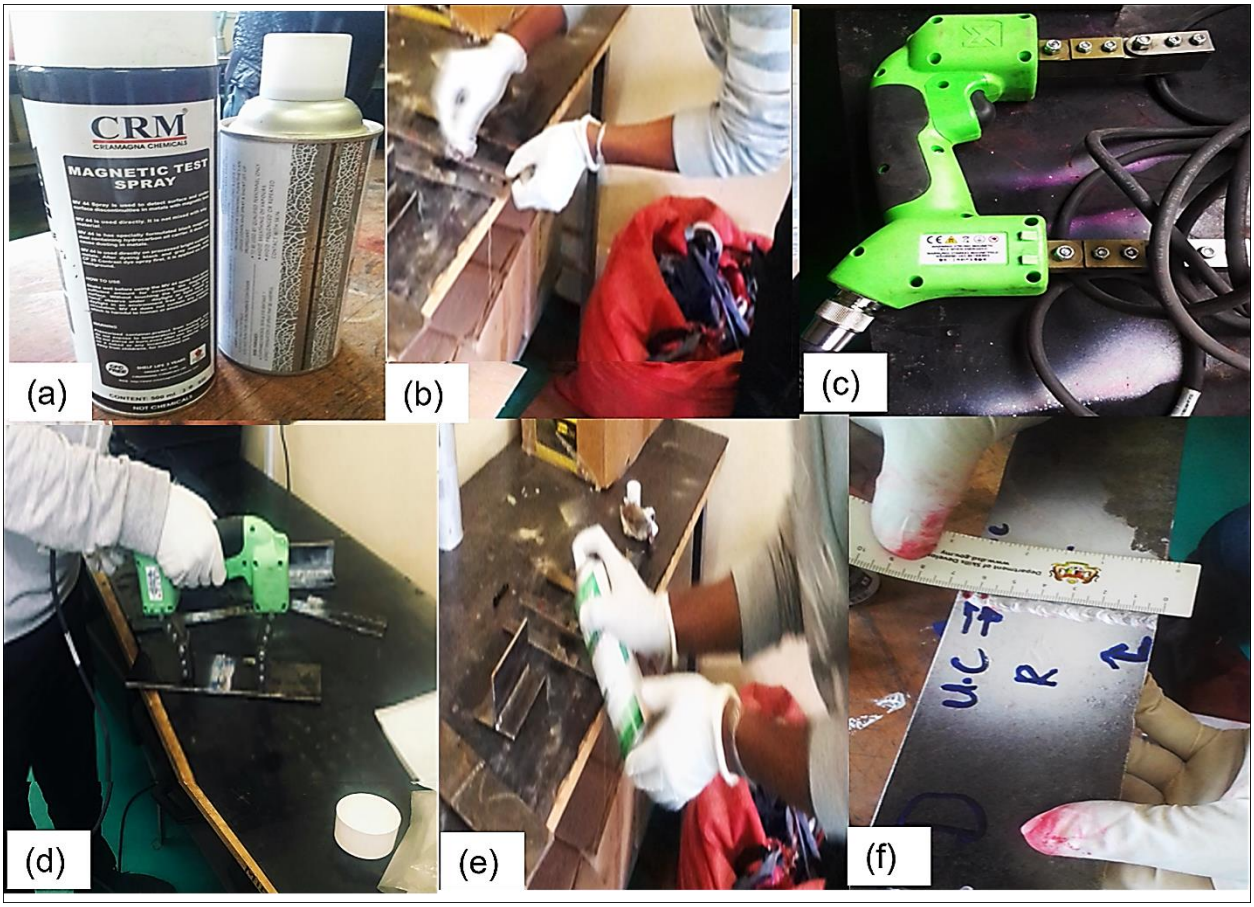

Fig.4. 9 Sequential procedure of magnetic particle testing (MPT) on MIG-welded joints

Surface preparation is shown in Fig.4. 9 (b), where a technician is seen manually cleaning the welded joints to ensure the surface is free from any interfering substances. This step is vital for producing reliable results, as even minor surface contamination can hinder defect visibility during testing. Once cleaned, the component is ready for magnetization. Fig.4. 9 (c) displays a yoke-type electromagnet, a common tool used to induce a magnetic field across the weld. When energized, the yoke creates a localized magnetic field that will be disrupted if any discontinuities**,** such as cracks**,** are present beneath or on the surface. The magnetization step is carried out in Fig.4. 9 (d), where the technician positions the yoke across the weld. Proper alignment ensures that the magnetic flux passes perpendicularly through potential defects, maximizing the likelihood of detecting interruptions in the field. With the magnetic field in place, the technician proceeds to apply magnetic particles, as shown in Fig.4. 9 (e). These particles, which may be visible or fluorescent, are sprayed evenly over the surface and are drawn to leakage fields that form at the sites of discontinuities. As a result, defects become clearly outlined by the accumulation of

magnetic particles, forming visible indications. Finally, Fig.4. 9 (f) depicts the inspection and evaluation phase. The ruler is used to measure and assess the size, orientation, and location of any indications formed during the test. These measurements help determine whether the weld meets established quality standards or requires further repair. This methodical process underscores the importance of cleanliness, correct magnetic field application, and careful interpretation of results to ensure accurate detection of flaws in welded structures. Through the steps captured in Fig.4. 9. MPT proves to be an effective tool in identifying surface and near-surface defects, thereby enhancing the safety and durability of welded components. Following the MPT procedure, several welded samples were examined to assess the presence and severity of welding defects. The results, illustrated in Fig.4. 10 , revealed noticeable variations in defect type and distribution among the samples. Sample 1 exhibited a small surface crack approximately 15 mm in length on the top side, while the bottom showed no signs of flaws. In contrast, Sample 2 displayed more severe damage, with pronounced cracks on the top measuring about 20 mm deep and 5 mm wide, though its bottom side remained defect-free. Sample 3 presented a combination of surface cracks and porosity on the top, while the bottom was found to be sound. The most critical damage was observed in the sample taken from an old sample structure(Saha et al., 2015). This sample revealed multiple flaws on both the top and root sides, including cracks, porosity, and side cutting on the surface, as well as a lack of penetration and a lack of fusion at the root. These defects represent serious structural concerns and indicate potential points of failure if not addressed. The findings from these inspections highlight the variation in weld quality due to differences in material condition, weld technique, and age, further reinforcing the importance of routine testing and quality control in welded structures.

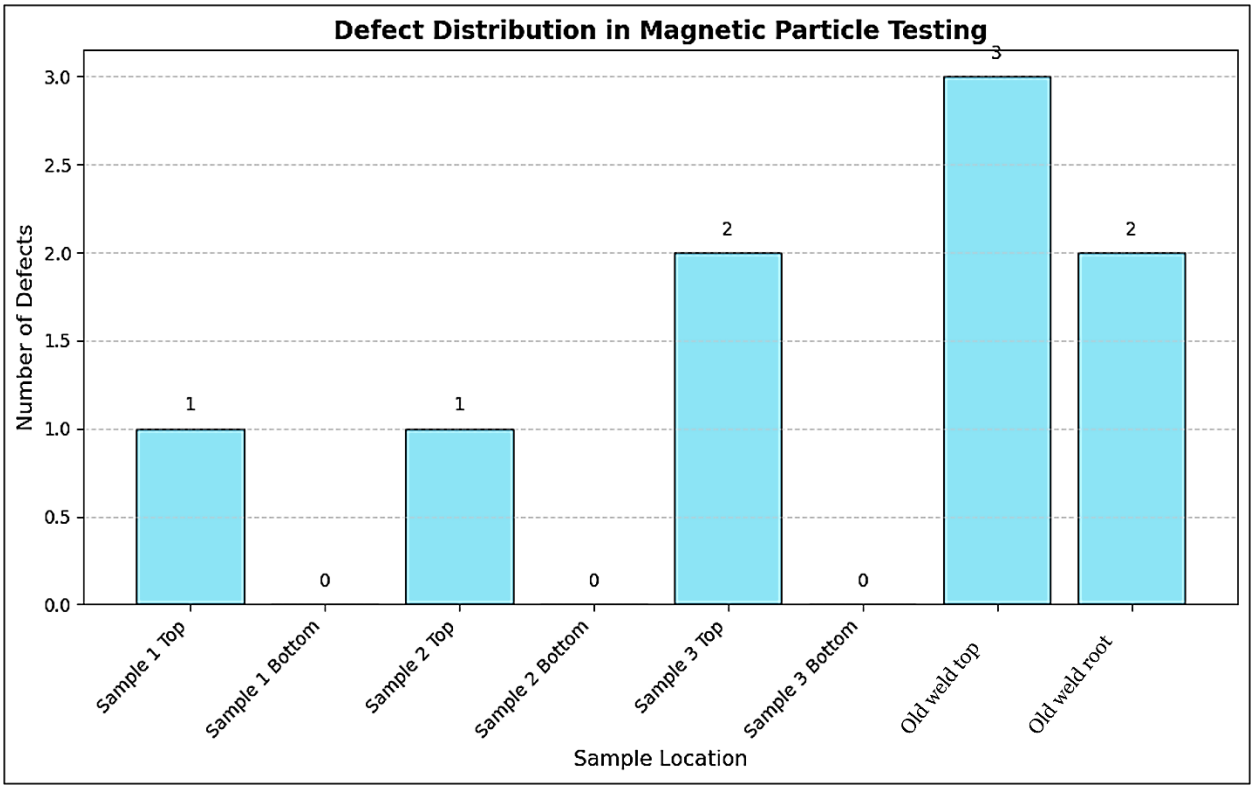

Fig.4. 10 Magnetic particle testing results of welded samples

4.8 Optimization

Since the experimental results of the newly welded joints component demonstrated more promising performance compared to the old, failed welds, it is reasonable to proceed with the optimization of process parameters. This step is crucial for further enhancing the new welding strategy, aiming to achieve the optimal solution for improving joint strength in the welded joints welding zone. The optimized approach will serve as a valuable guideline for personnel responsible for carrying out the welding process, and it may also provide insights for future applications where similar welded joints or joining processes are required. Welding of structural steels requires careful control of process parameters to ensure sound joints with reliable mechanical performance. AISI 1018, low-carbon steel commonly used in automotive, construction, and manufacturing industries, is frequently joined using the MIG welding process because of its versatility and efficiency. However, the properties of the weld are strongly influenced by the combination of current, voltage, and travel speed, as these variables determine the effective heat input, cooling rate, and subsequent microstructural changes within both the weld metal and the heat-affected zone. In this investigation, MIG welding trials were carried out on AISI 1018 steel plates to evaluate how different parameter settings affect joint quality. The focus was placed on understanding the

influence of arc current, arc voltage, and welding speed on the resulting strength, ductility, and hardness of the welds(Guizani et al., 2019). The experimental results are expressed through yield strength, ultimate tensile strength, strain at fracture, and hardness values measured in both the weld zone and the heat-affected zone. The outcomes of these experiments are presented in Table 4. 1, which summarizes the response of mechanical properties to variations in welding conditions. By analyzing these data, the interaction between heat input and material behavior can be more clearly understood, offering valuable guidance in selecting parameter combinations that optimize the strength and performance of AISI 1018 weld joints.

Table 4. 1 Experimental results of MIG welding

	Factor 1	Factor 2	Factor 3	Response 1	Response 2	Response 3	Response 4
Run	A:Current	B:Voltage	C:Speed	Yield strength	UTS	Strain at fracture	Hardness at WZ
	A	V	mm/s	MPa	MPa	%	HRB
1	80	19	3.33	413	512	21.5	94
2	80	19	3.33	413	512	21.5	94
3	120	19	3.33	396	490	23.4	91.1
4	120	19	3.33	396	490	23.4	91.1
5	80	21	3.33	402	498	22.6	92.2
6	80	21	3.33	402	498	22.6	92.2
7	120	21	3.33	385	476	24.6	88.9
8	120	21	3.33	385	476	24.6	88.9
9	80	19	3.85	425	527	20.1	96
10	80	19	3.85	425	527	20.1	96
11	120	19	3.85	405	502	22.4	92.5
12	120	19	3.85	405	502	22.4	92.5
13	80	21	3.85	412	510	21.7	93.7
14	80	21	3.85	412	510	21.7	93.7
15	120	21	3.85	391	483	23.9	90.1
16	120	21	3.85	391	483	23.9	90.1
17	80	20	3.59	416	515	21.1	94.4

18	80	20	3.59	416	515	21.1	94.4
19	120	20	3.59	394	487	23.6	90.7
20	120	20	3.59	394	487	23.6	90.7
21	100	19	3.59	420	521	20.6	95.2
22	100	19	3.59	420	521	20.6	95.2
23	100	21	3.59	402	498	22.6	92.2
24	100	21	3.59	402	498	22.6	92.2
25	100	20	3.33	401	497	22.8	91.9
26	100	20	3.33	401	497	22.8	91.9
27	100	20	3.85	412	511	21.6	93.8
28	100	20	3.85	412	511	21.6	93.8
29	100	20	3.59	408	505	22.1	93.2
30	100	20	3.59	408	505	22.1	93.2
31	100	20	3.59	408	505	22.1	93.2
32	100	20	3.59	408	505	22.1	93.2

From Table 4.1, Runs **17, 21, and 25** exhibited the most favorable combination of mechanical properties, simultaneously achieving high yield strength (>395 MPa), high ultimate tensile strength (>490 MPa), elevated ductility (>21%), and balanced hardness levels in both the weld zone and heat-affected zone. These runs were characterized by intermediate-to-high welding current, moderate voltage, and optimized travel speed, resulting in adequate heat input for full fusion without excessive grain coarsening. Consequently, these experimental conditions were considered near-optimal and were used as reference benchmarks during the subsequent Response Surface Methodology (RSM) optimization and desirability function analysis.

4.8.1 ANOVA results of yield strength

The ANOVA results in Table 4. 2 confirm that the quadratic model for yield strength is statistically significant, with an overall F-value of 200.69 and a p-value below 0.0001. For clarity, only statistically significant terms ($p < 0.05$) are emphasized in the discussion, while non-significant higher-order terms are retained in the tables for completeness but omitted from interpretation(Sood et al., 2022). This demonstrates that the model effectively explains the variation in yield strength as influenced by welding parameters. Current (A) is the most dominant factor, accounting for

54.0% of the variation in yield strength, followed by voltage (B) at 25.8%, and travel speed (C) at 13.2% as shown in Fig.4. 11. Together, these three linear terms contribute over 93% of the total model sum of squares, highlighting their critical influence on weld strength. Among the interaction terms, only AC (current × speed) is statistically significant (0.35%), while AB and BC interactions contribute negligibly (<0.2%).

Table 4. 2 ANOVA results for the quadratic model for yield strength

Source	Sum of Squares	df	Mean Square	F-value	p-value	
Model	3461.34	9	384.59	200.69	< 0.0001	significant
A-Current	1881.80	1	1881.80	981.96	< 0.0001	
B-Voltage	897.80	1	897.80	468.49	< 0.0001	
C-Speed	460.80	1	460.80	240.45	< 0.0001	
AB	0.2500	1	0.2500	0.1305	0.7214	
AC	12.25	1	12.25	6.39	0.0191	
BC	6.25	1	6.25	3.26	0.0846	
A^2	92.55	1	92.55	48.30	< 0.0001	
B^2	17.28	1	17.28	9.02	0.0066	
C^2	38.14	1	38.14	19.90	0.0002	
Residual	42.16	22	1.92			
Lack of Fit	42.16	5	8.43	0.3775	0.9458	not significant
Pure Error	0.0000	17	0.0000			
Cor Total	3503.50	31				

The quadratic terms also play a measurable role: A^2 contributes 2.7%, B^2 contributes 0.5%, and C^2 contributes 1.1%, collectively confirming that yield strength varies non-linearly with the process parameters. The inclusion of these terms ensures the model captures curvature effects across the parameter space. The lack-of-fit test is not significant ($p = 0.9458$), confirming the adequacy of the model with no systematic error. The small residual mean square (1.92) further demonstrates that experimental error is minimal. Thus, current is the single most influential factor on yield strength, followed by voltage and travel speed. Together, they dominate the response, while

quadratic and interaction effects play smaller but meaningful roles. These results emphasize that careful control of current, complemented by optimized voltage and speed settings, is essential for maximizing yield strength in MIG-welded AISI 1018 steel. Equation 4.1 is a quadratic regression model predicting yield strength based on inputs including their interactions and squared terms.

$$\text{Yield strength} = 386.12 + 2.34A - 69.86B + 369.04C - 0.00625AB - 0.168AC - 2.40BC - 0.0105A^2 + 1.81B^2 - 39.79C^2 \quad (4.1)$$

Where, A is current (A), B is voltage (V) and C is speed (mm/s)

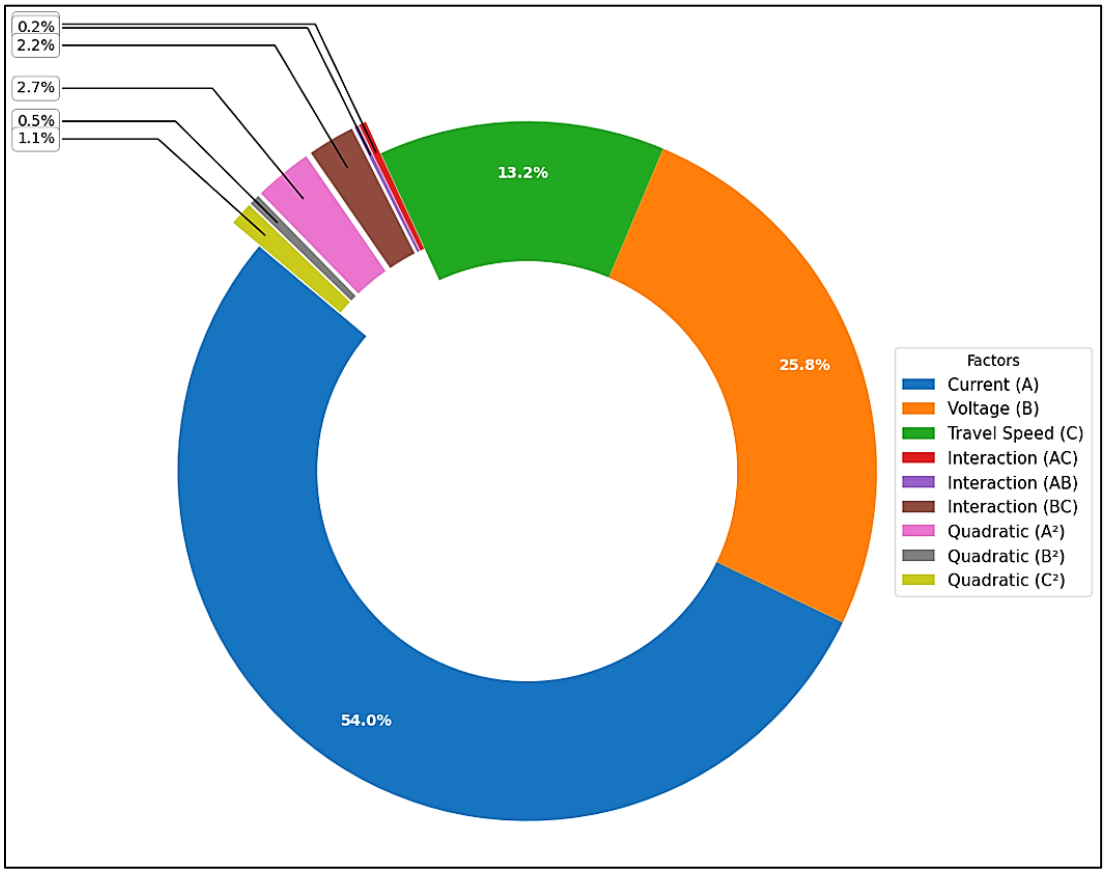

Fig.4. 11 Contribution percentages of process parameters to yield strength variation

4.8.2 ANOVA results of ultimate tensile strength

The ANOVA results for the quadratic model for UTS in Table 4. 3 show that the model is highly significant, with an F-value of 197.38 and a p-value less than 0.0001, indicating that the variation

in ultimate tensile strength is well explained by the combination of current, voltage, and speed, along with their interactions and quadratic effects. For clarity, only statistically significant terms ($p < 0.05$) are emphasized in the discussion, while non-significant higher-order terms are retained in the tables for completeness but omitted from interpretation. Current is the most influential factor, contributing approximately 53.4% of the total variation, followed by voltage, which contributes around 26.3%, and speed, which accounts for about 12.5% as presented in Fig.4. 12. Interaction effects between current and speed, as well as between voltage and speed, are significant but minor, each contributing roughly 0.28% of the total variation. The quadratic terms also add meaningful refinement to the model, with current squared contributing around 3.3%, speed squared about 0.8%, and voltage squared approximately 0.6%. The residual sum of squares is very small, and the lack-of-fit is not significant, confirming that the model accurately represents the experimental data. Overall, the results highlight that current is the dominant factor influencing UTS, followed by voltage and speed, while the significant interactions and quadratic terms improve the precision of the model and provide a complete understanding of the effects of process parameters on tensile strength. Equation 4.2 is a quadratic regression model predicting UTS based on inputs including their interactions and squared terms.

$$UTS=588.54+3.30A-95.02B+434.21C-0.0125A\cdot B-0.1923A\cdot C-3.85B\cdot C-0.0149A^2+2.53B^2-43.87C^2 \quad (4.2)$$

Table 4. 3 ANOVA results for quadratic model for UTS

Source	Sum of Squares	df	Mean Square	F-value	p-value	
Model	5688.43	9	632.05	197.38	< 0.0001	significant
A-Current	3075.20	1	3075.20	960.34	< 0.0001	
B-Voltage	1513.80	1	1513.80	472.74	< 0.0001	
C-Speed	720.00	1	720.00	224.85	< 0.0001	
AB	1.0000	1	1.0000	0.3123	0.5819	
AC	16.00	1	16.00	5.00	0.0359	
BC	16.00	1	16.00	5.00	0.0359	
A^2	187.64	1	187.64	58.60	< 0.0001	
B^2	33.87	1	33.87	10.58	0.0037	

C^2	46.37	1	46.37	14.48	0.0010	
Residual	70.45	22	3.20			
Lack of Fit	70.45	5	14.09	0.2765	0.9156	not significant
Pure Error	0.0000	17	0.0000			
Cor Total	5758.88	31				

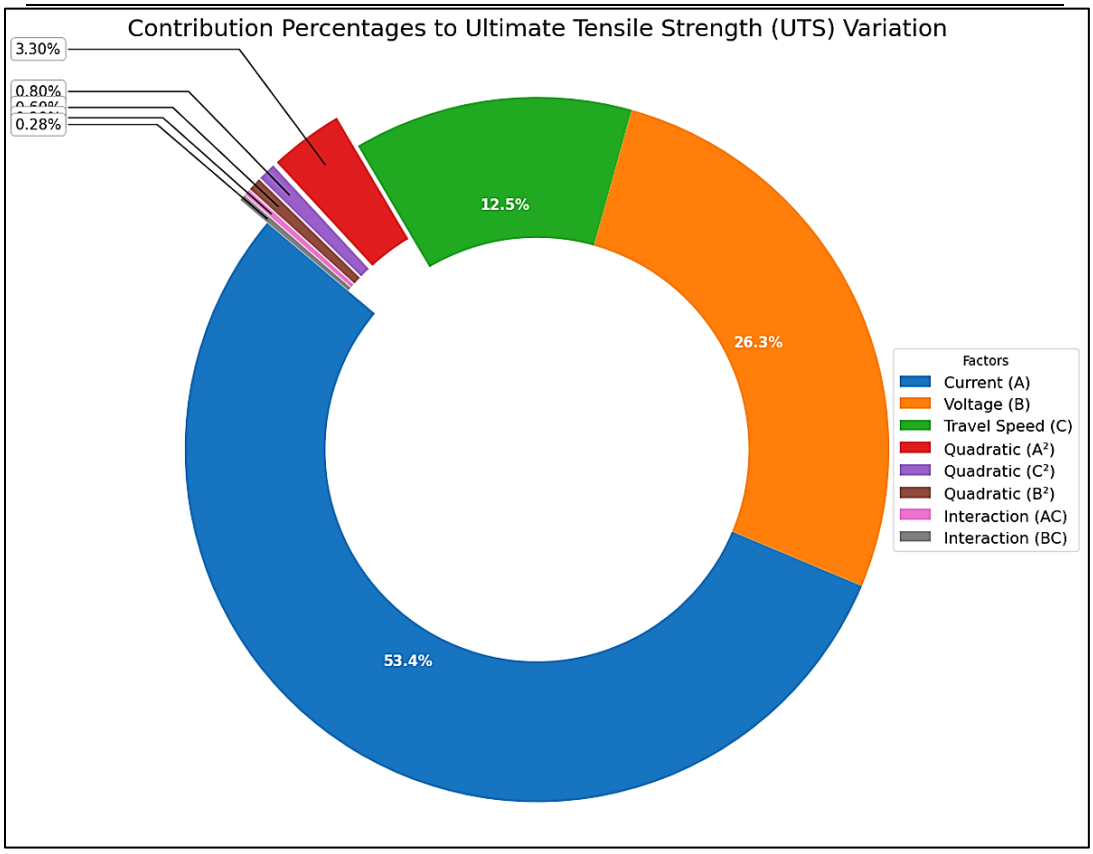

Fig.4. 12 Contribution percentages of process parameters to ultimate tensile strength (UTS) Variation

4.8.3 ANOVA results of strain at fracture (ductility)

The ANOVA results presented in Table 4. 4 for the quadratic model of strain at fracture indicate that the model is highly significant, with an F-value of 152.84 and a p-value less than 0.0001, showing that the variation in the response is overwhelmingly due to the factors rather than random error. For clarity, only statistically significant terms ($p < 0.05$) are emphasized in the discussion, while non-significant higher-order terms are retained in the tables for completeness but omitted from interpretation. As detailed in Table 4.4, current (A) is the dominant contributor, accounting for approximately 54% of the total variation, followed by voltage (B) at around 25% and speed

(C) at roughly 12% as shown in Fig.4. 13. Among the interactions, only BC contributes a small but notable portion of about 0.4%, while AB and AC are negligible. The quadratic terms also have significant effects, with A^2 contributing 2.9%, C^2 1.4%, and B^2 0.8%, highlighting the presence of nonlinear behavior in the response. The residual variance is minimal, and the lack of fit is not significant, confirming that the quadratic model effectively represents the experimental data. Thus, Table 4.4 demonstrates that current, voltage, and speed are the primary factors influencing strain at fracture, with current having the largest impact, while interactions and curvature effects are minor yet present. Equation 4.3 is a quadratic regression model predicting strain at fracture based on inputs including their interactions and squared terms.

$$\text{Strain at fracture} = 13.463 - 0.241A + 9.842B - 47.027C + 0.014AC + 0.385BC + 0.0012A^2 - 0.262B^2 + 4.999C^2 \quad (4.3)$$

Table 4. 4 ANOVA results for the quadratic model for strain at fracture

Source	Sum of Squares	df	Mean Square	F-value	p-value	
Model	43.17	9	4.80	152.84	< 0.0001	significant
A-Current	23.76	1	23.76	757.17	< 0.0001	
B-Voltage	10.95	1	10.95	348.98	< 0.0001	
C-Speed	5.41	1	5.41	172.33	< 0.0001	
AB	0.0000	1	0.0000	0.0000	1.0000	
AC	0.0900	1	0.0900	2.87	0.1045	
BC	0.1600	1	0.1600	5.10	0.0342	
A^2	1.26	1	1.26	40.00	< 0.0001	
B^2	0.3621	1	0.3621	11.54	0.0026	
C^2	0.6021	1	0.6021	19.19	0.0002	
Residual	0.6904	22	0.0314			
Lack of Fit	0.6904	5	0.1381	0.4344	0.9765	not significant
Pure Error	0.0000	17	0.0000			
Cor Total	43.86	31				

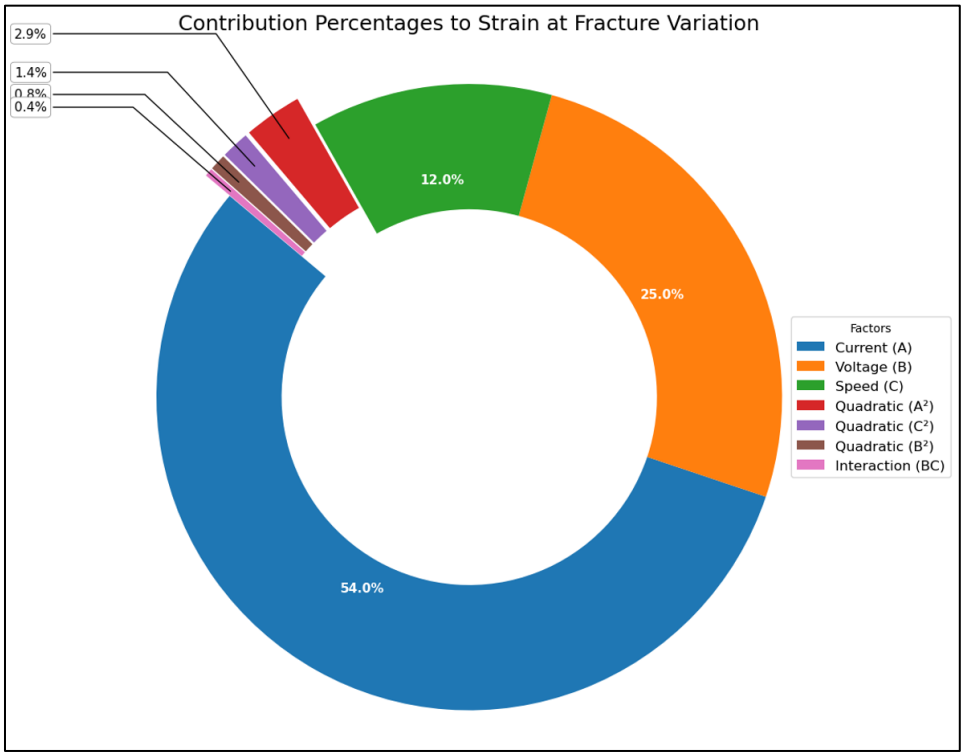

Fig.4. 13 Contribution percentages of process parameters to strain at fracture variation

4.8.4 ANOVA results of hardness at the weld zone (WZ)

The ANOVA results for hardness at the WZ are shown in Table 4. 5 indicating that the quadratic model is highly significant, with an F-value of 295.80 and a p-value less than 0.0001, suggesting that the likelihood of such a large F-value occurring due to random noise is extremely low. For clarity, only statistically significant terms ($p < 0.05$) are emphasized in the discussion, while non-significant higher-order terms are retained in the tables for completeness but omitted from interpretation. Among the factors studied, current (A) is the most influential, contributing approximately 54.2% of the total variation in hardness, followed by voltage (B) with around 25.7%, and speed (C) at about 12.0% as presented in Fig.4. 14. The quadratic effects also play an important role, with A^2 accounting for 3.2%, C^2 for 1.3%, and B^2 for 0.6% of the total variation. Among the interaction terms, only AC is significant, contributing 0.2%, while AB and BC are negligible. The residual variation is minimal, around 0.8%, indicating that the model captures nearly all variability in the response. These results clearly show that current and voltage are the primary factors controlling hardness at the weld zone, with speed and quadratic terms providing secondary contributions, and interactions having a limited effect.

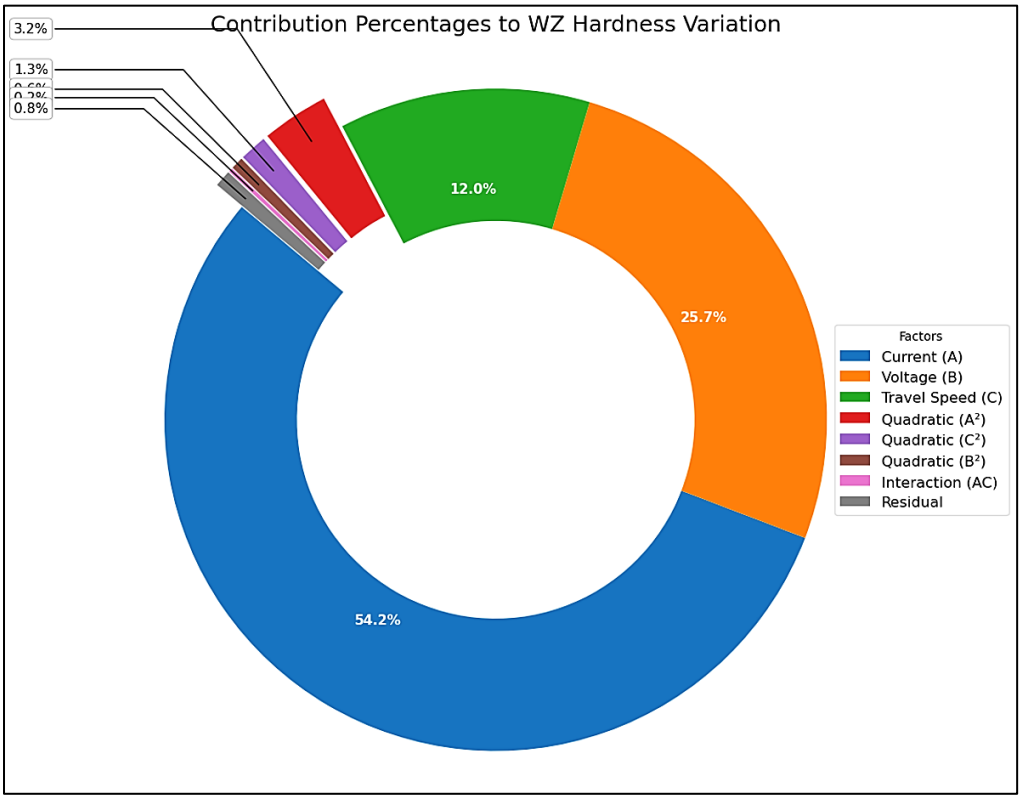

Fig.4. 14 Contribution percentages of process parameters to WZ hardness variation

This analysis, aligned with ANOVA results, provides a clear understanding of the relative importance of each factor in determining weld zone hardness. Equation 4.4 is a quadratic regression model predicting strain at fracture based on inputs including their interactions and squared terms.

$$\text{Hardness at WZ} = 94.285 + 0.460A - 13.236B + 66.176C - 0.003AB - 0.022AC - 0.337BC - 0.002A^2 + 0.340B^2 - 7.549C^2 \quad (4.4)$$

Table 4. 5 ANOVA results for the quadratic model for hardness at WZ

Source	Sum of Squares	df	Mean Square	F-value	p-value	
Model	105.86	9	11.76	295.80	< 0.0001	significant
A-Current	57.80	1	57.80	1453.51	< 0.0001	
B-Voltage	27.38	1	27.38	688.48	< 0.0001	
C-Speed	12.80	1	12.80	321.89	< 0.0001	
AB	0.0625	1	0.0625	1.57	0.2231	
AC	0.2025	1	0.2025	5.09	0.0343	

BC	0.1225	1	0.1225	3.08	0.0932
A^2	3.46	1	3.46	87.07	< 0.0001
B^2	0.6083	1	0.6083	15.30	0.0007
C^2	1.37	1	1.37	34.53	< 0.0001
Residual	0.8748	22	0.0398		
Lack of Fit	0.8748	5	0.1750		not significant
Pure Error	0.0000	17	0.0000	0.4224	0.9533
Cor Total	106.74	31			

4.8.5 ANOVA results of hardness at heat heat-affected zone (HAZ)

The ANOVA results for hardness at HAZ in Table 4. 4 indicate that the quadratic model is highly significant, with an F-value of 240.13 and a p-value less than 0.0001, confirming that the model reliably explains the variations in HAZ hardness. For clarity, only statistically significant terms ($p < 0.05$) are emphasized in the discussion, while non-significant higher-order terms are retained in the tables for completeness but omitted from interpretation. As presented in Fig.4. 15, current is the most influential factor, contributing approximately 53.9% of the total variation, followed by voltage at 25.6% and speed at 11.7%, highlighting that the welding current has the dominant effect on hardness in the HAZ. Quadratic effects of current, voltage, and speed also have significant contributions of 3.7%, 0.7%, and 1.2% respectively, indicating the presence of non-linear behavior in the response. Interaction terms AB, AC, and BC are not significant, contributing negligibly to the overall variation, suggesting that the combined effects of these factors are minimal in this process. The lack-of-fit test is not significant, confirming the adequacy of the model to describe the experimental data. Thus, the results demonstrate that while current is the primary controlling factor, voltage and speed, along with their quadratic terms, also play meaningful roles in determining the hardness at HAZ. Using inputs such as their interactions and squared terms, the quadratic regression model in Equation 4.5 predicts strain at fracture.

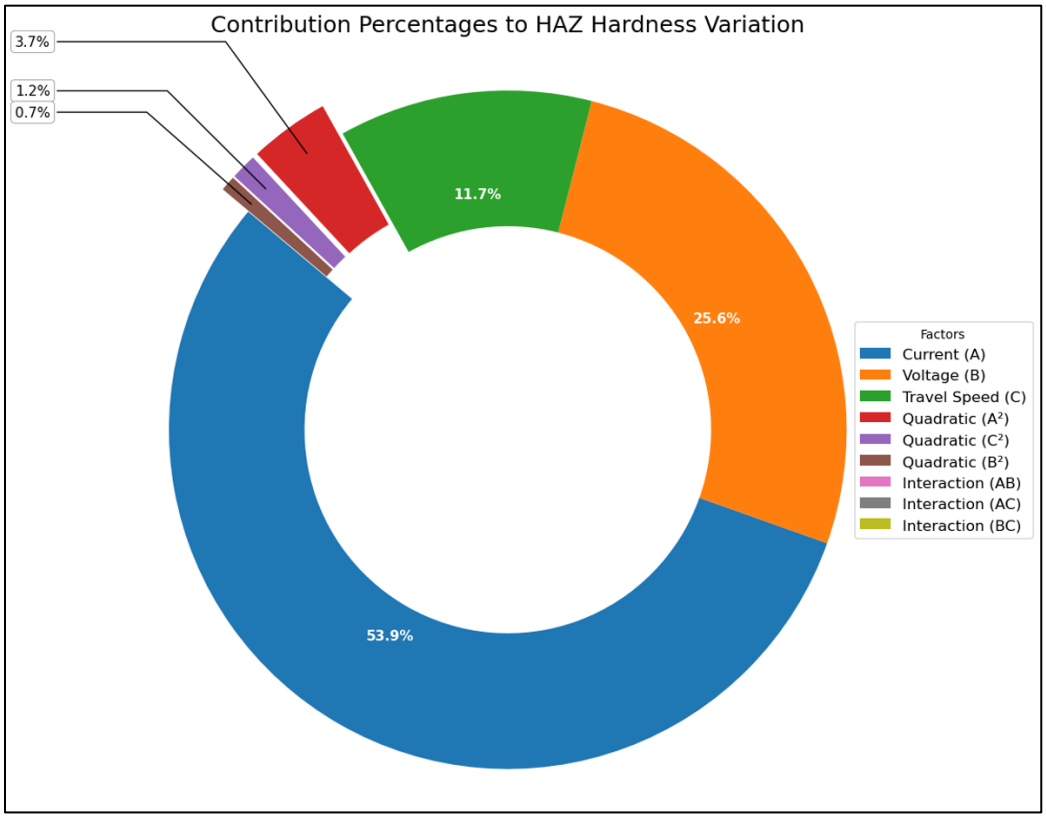

Fig.4. 15 Contribution percentages of process parameters to HAZ variation

Hardness at HAZ=99.17+0.401A−11.754B+52.406C−0.0031AB−0.0168AC−0.337BC−0.00173 A^2+0.309B^2−5.790C^2 (4.5)

Table 4. 6 ANOVA results for the quadratic model for hardness at HAZ

Source	Sum of Squares	df	Mean Square	F-value	p-value	
Model	67.00	9	7.44	240.13	< 0.0001	significant
A-Current	36.45	1	36.45	1175.78	< 0.0001	
B-Voltage	17.30	1	17.30	557.99	< 0.0001	
C-Speed	7.94	1	7.94	256.06	< 0.0001	
AB	0.0625	1	0.0625	2.02	0.1697	
AC	0.1225	1	0.1225	3.95	0.0594	
BC	0.1225	1	0.1225	3.95	0.0594	
A^2	2.52	1	2.52	81.30	< 0.0001	

B^2	0.5022	1	0.5022	16.20	0.0006	
C^2	0.8077	1	0.8077	26.05	< 0.0001	
Residual	0.6820	22	0.0310			
Lack of Fit	0.6820	5	0.1364	0.5445	0.9012	not significant
Pure Error	0.0000	17	0.0000			
Cor Total	67.68	31				

To enhance readability and interpretability, the key statistically significant factors across all response variables are summarized in Table 4.7. Welding current consistently emerged as the dominant parameter influencing strength and hardness responses, whereas welding speed exerted a more pronounced effect on ductility (Venkatratnam & Kesava Rao, 2020). Voltage exhibited secondary but meaningful interactions, particularly with current and travel speed. This consolidated overview enables rapid identification of parameter sensitivities without requiring detailed inspection of individual ANOVA tables, thereby improving clarity and practical usability of the statistical findings(Said et al., 2023).

Table 4.7 Summary of significant welding parameters for all response variables

Response Variable	Significant Factors ($p < 0.05$)	Dominant Factor
Yield Strength	Current, Speed, Current², Current×Speed	Current
Ultimate Tensile Strength	Current, Voltage, Speed, Current²	Current
Strain at Fracture	Speed, Voltage×Speed	Speed
Weld Zone Hardness	Current, Current², Current×Voltage	Current
HAZ Hardness	Current, Speed, Current×Speed	Current

4.8.6 Interaction analysis of yield strength

The interaction analysis is shown in Fig.4. 16 yield strength results from the joint influence of welding parameters on mechanical performance. Two plots in Fig.4. 16 (a) plot current (A) and voltage (B) at a constant speed of 3.59 mm/s: With increasing current, yield strength increases until about 100 A, whereafter it drops again due to overheating and grain coarsening; while voltage shows little effect beyond an optimum range of about 20 to 20.5 V. This demonstrates that the most balanced heat input yields the best strength. Fig.4. 16 (b), which considers the current (A) and speed (C) interaction at a constant 20 V voltage, reveals a pronounced dome-shaped surface.

Yield strength gained with increasing speed, since higher travel speed can reduce heat input per unit length, with an optimum found near 3.7 to 3.8 mm/s. Current also showed a peak, again around 100 A, beyond which the trend for mechanical performance declined. This interaction Fig.4. 16 (c) shows how important is the control of both current and speed concurrently is towards attaining maximum yield. The combined influence of voltage (B) and speed (C) at a fixed current of 100 A is illustrated. In this case, an additive effect occurs for both parameters, reaching an optimum for voltage at about 20 to 20.5 V and again positively influencing speed to about 3.7 to 3.8 mm/s. Thus, the analyses taken together confirm that the maximum yield strength is found under intermediate heat input conditions, specifically around 100 A current, 20 to 20.5 V voltage, and 3.7 to 3.8 mm/s speed. This window balances the fusion quality against controlled microstructural development, thereby generating stronger and more reliable welds.

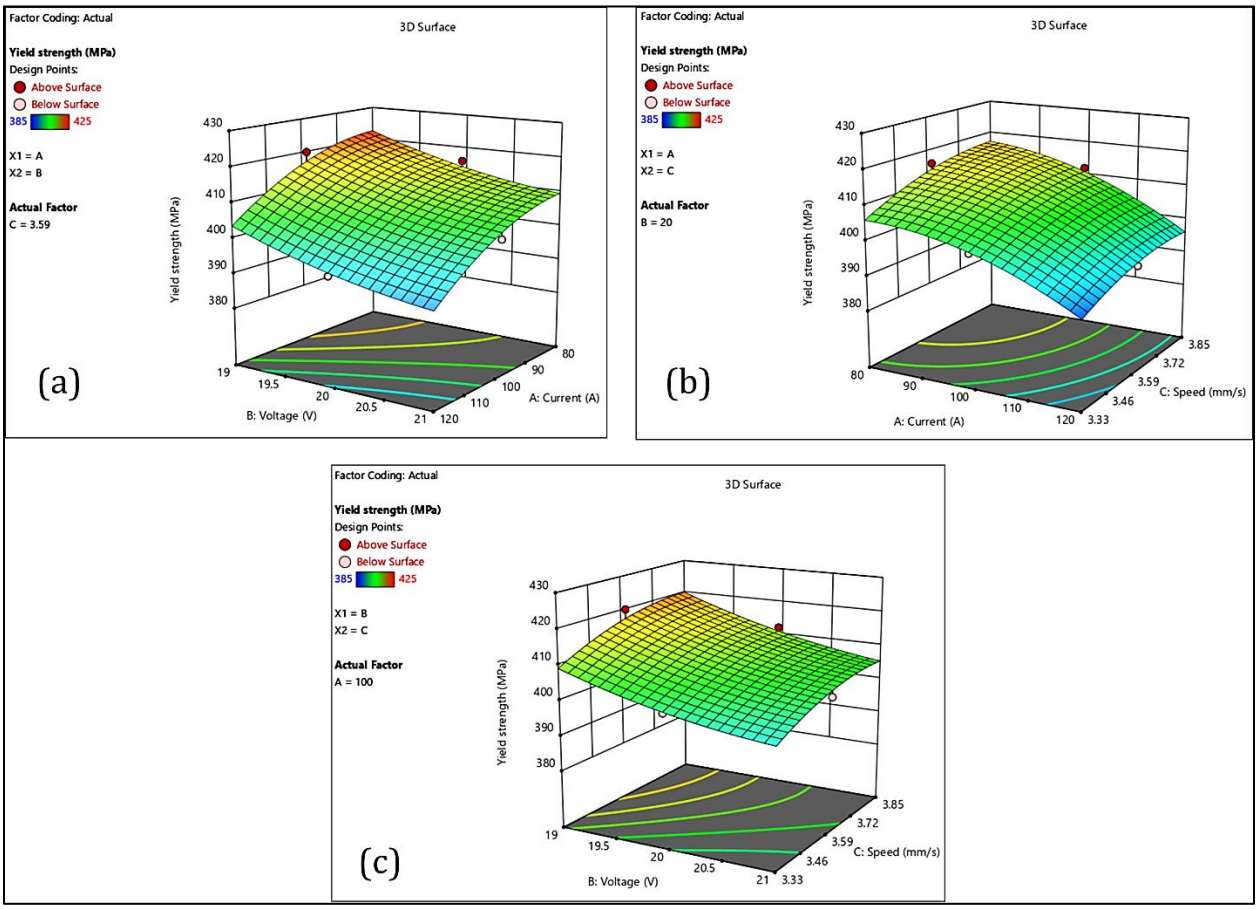

Fig.4. 16 Interaction analysis yield strength (3D surface)

The contour Fig.4. 17 shows the interaction effects of current, voltage, and speed on yield strength, complementing dimensioned surface analysis. Fig.4. 17 (a) shows the relationship between current

and voltage, holding speed constant at 3.59 mm/s, with yield strength increasing with both parameters to an optimal region around 100 A of current and 20-20.5 V, where it value of about 420 MPa. Beyond this region, either excessive current or very low voltage causes a reduction of performance due to unbalanced heat input. The speed-increasing effect of yield strength improvement up to about 3.7-3.8 mm/s is observed in Fig.4. 17 (b), as higher travel speeds would minimize heat accumulation. The effect of current again shows parabolic behavior, with yield strength being the highest near 100 A, while divergences from this point will yield lower results. Fig.4. 17 (c) illustrates the interaction of voltage and speed at 100 A constant current, where both factors act additively to yield strength. The optimum conditions are realized on moderate voltage (20-20.5 V) and higher speed (around 3.7 mm/s), where yield strength approaches 415-420 MPa. The contour diagrams indicate that, under intermediate heat input conditions, maximum yield strength is obtained, for the most part, in a region centered around 100 A current, 20-20.5 V voltage, and 3.7-3.8 mm/s speed. This leads to the conclusion that a critical control and balancing of parameters ensures that strong, defect-free welds are produced.

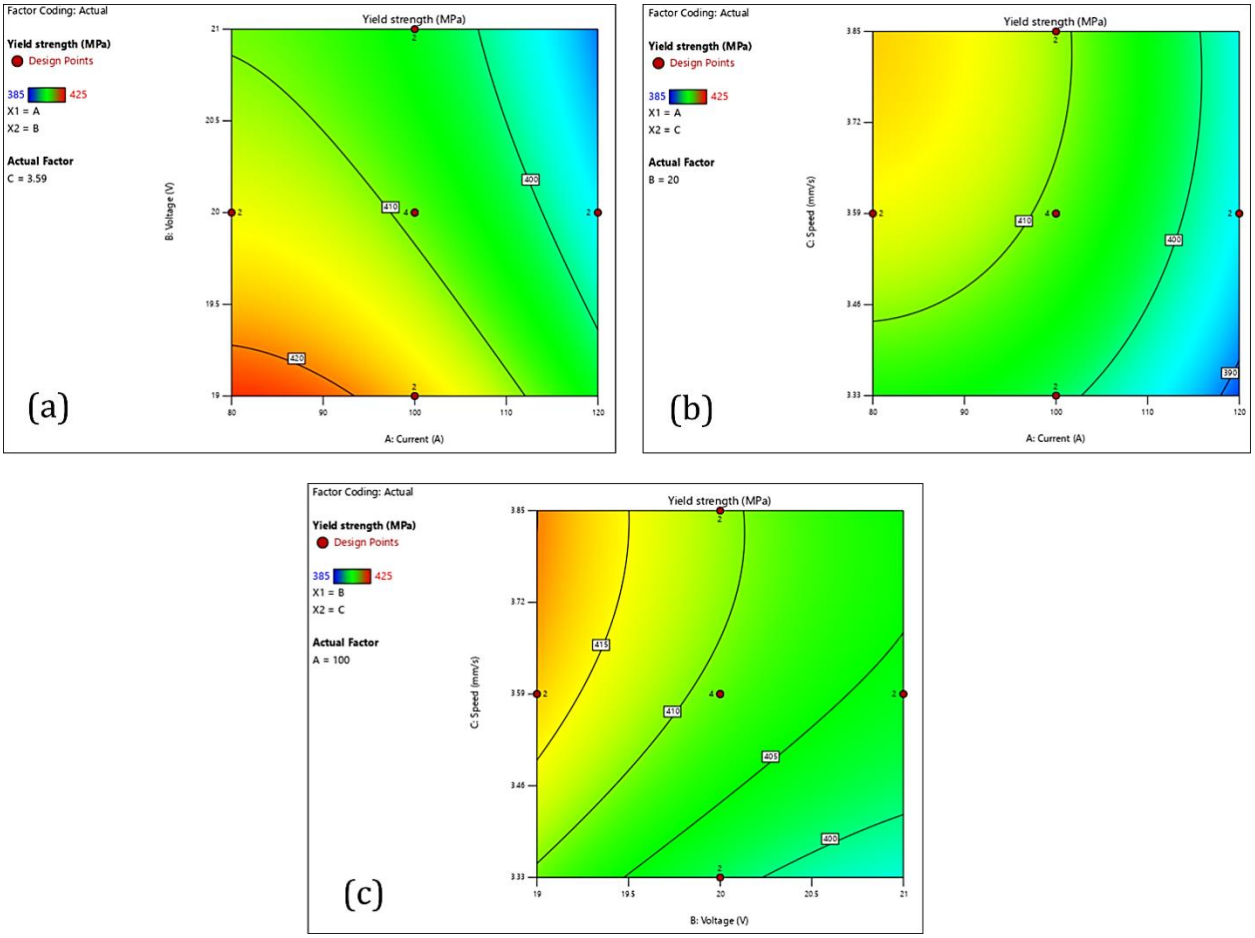

Fig.4. 17 Interaction analysis yield strength (contour plot)

The contour plots reveal that yield strength increases with increasing welding current and moderate travel speed. At low current–high speed combinations, insufficient heat input results in lack of fusion and reduced metallurgical bonding, leading to diminished strength. Conversely, excessively high current combined with low speed causes overheating and grain coarsening, which reduces yield strength despite improved fusion. The optimal yield strength region occurs at intermediate-to-high current and moderate speed, where sufficient penetration and refined microstructures coexist.

In this table, the experimental actual yield strength values have been compared with the values predicted by a regression model from the 32 sets of experiments. The results indicate that there is a very strong agreement, with differences usually expected within 1-2 MPa. The results indicate that the model is both accurate and reliable. For example, run 1 truly yielded a yield strength of 405 MPa against a predicted value of 405.40 MPa, which is practically zero deviation from the truth. Runs 13 and 24 both reported the highest actual strength at 425 MPa, which the model

successfully predicted at 426.30 MPa. Even at the lower end, such as Run 10 with 385 MPa actual and 383.90 MPa predicted, the difference is tiny. These discrepancies are more likely to be accounted for by normal variations in the experiment; however, having such a close agreement for all runs indicates that the regression model captures the relationship between welding parameters and yield strength. So overall, the verification of high reliability for the model to predict weld performance as well as provide a practical guide toward optimizing welding conditions is done here in Fig.4. 18.

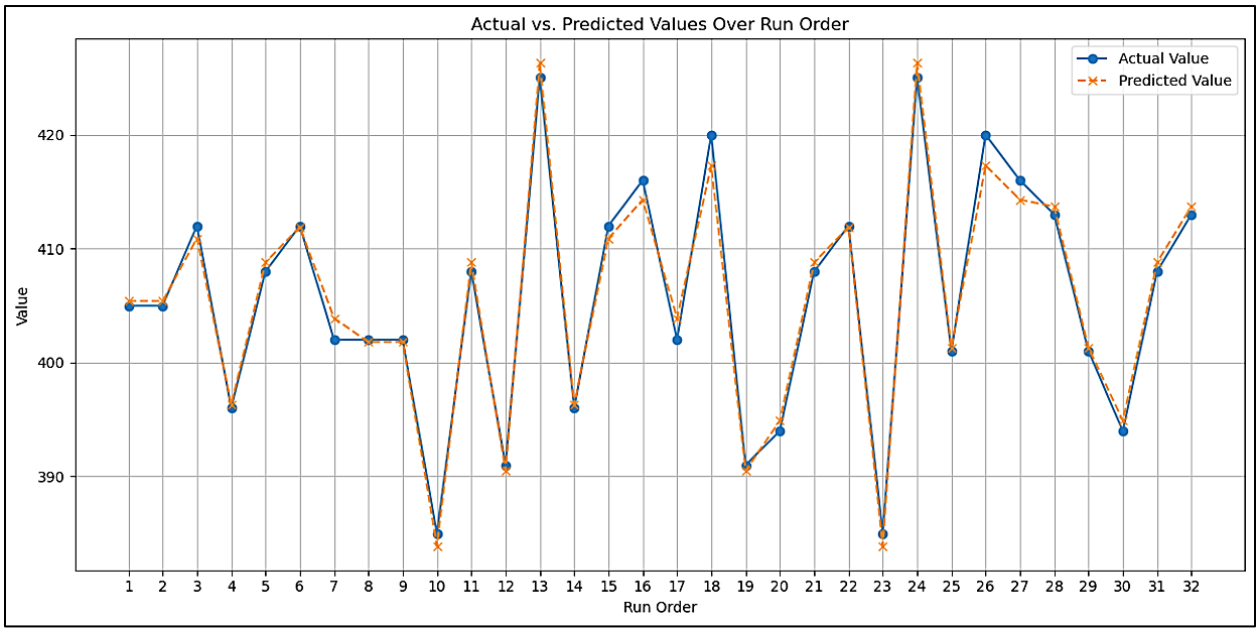

Fig.4. 18 Predicted vs. actual results of yield strength

4.8.7 Interaction analysis of ultimate tensile strength

The interaction analysis of ultimate tensile strength (UTS) shows the effect of current, voltage, and speed on weld performance collectively. Fig.4. 19 (a) shows that the UTS first increases with current and voltage at a constant speed of 3.59 mm/s until an optimum area, approximately 100 A and 20–20.5 V, with a corresponding strength of around 520–527 MPa. Beyond this regime, UTS decreases because of either the lack of fusion at low settings or melting and coarse-grained structuring at higher input. Fig.4. 19 (b) displays a dome with its UTS maximized near a current of about 100 A and higher speeds of about 3.7–3.8 mm/s when speed is varied with current at a constant voltage of 20 V. The UTS improvement with speed may result from a lower heat input per unit length affecting microstructure refinement and welding pool stability, while a moderate current secures full penetration. From the analysis given in Fig.4. 19 (c), where voltage and speed

inputs are evaluated while holding the current at 100 A, it could be concluded that both parameters act additively, again with optimum positions near 20–20.5 V and 3.7–3.8 mm/s for the obtained UTS ranging from 515 to 525 MPa. Overall, these results show that maximum UTS occurs at intermediate heat input, particularly around 100 A, 20–20.5 V, and 3.7–3.8 mm/s. These conditions seem to represent a balance, allowing for good fusion while preventing excessive exposure to heat, thus strong and defect-free welds have better tensile properties.

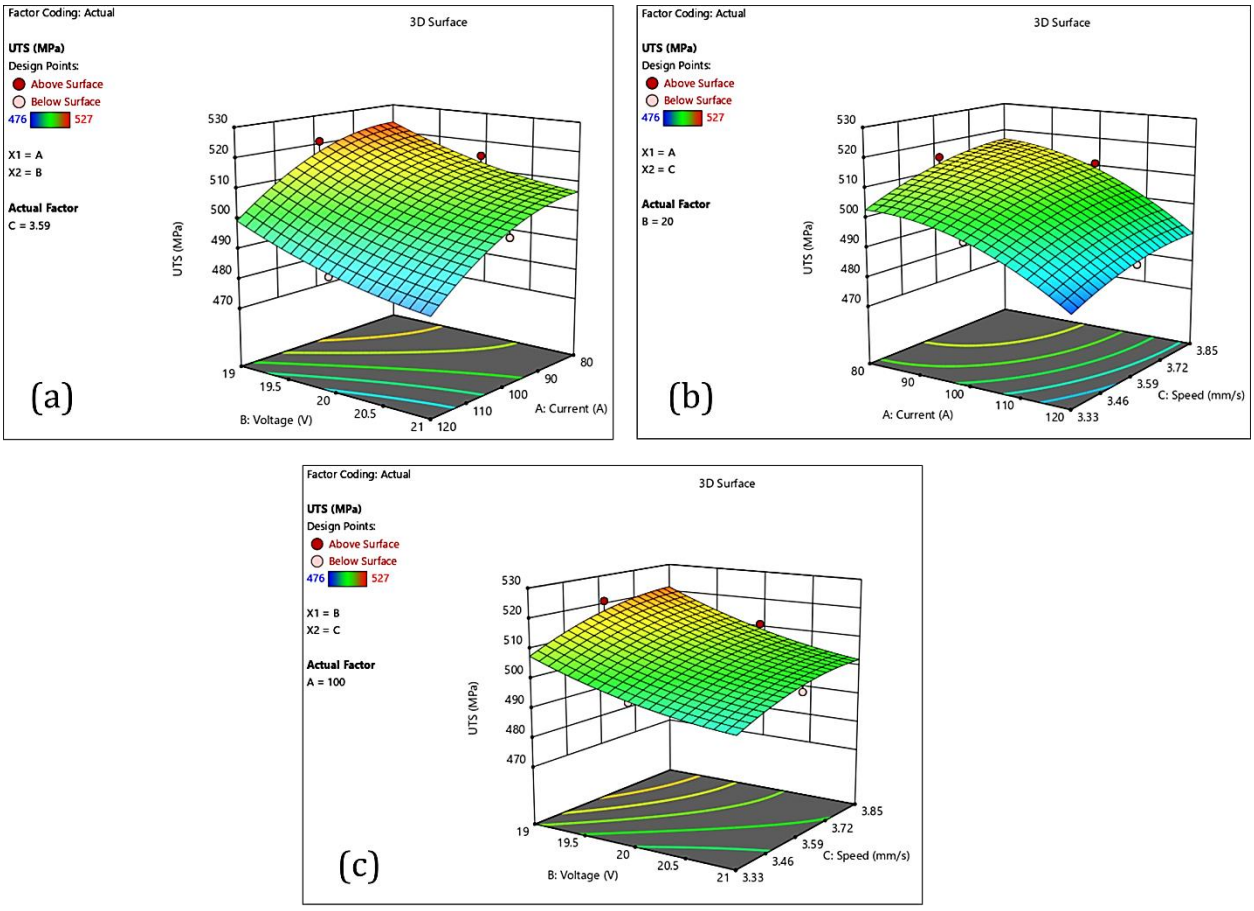

Fig.4. 19 Interaction analysis ultimate strength (3D surface)

4.8.8 Interactive effects of welding parameters on ultimate tensile strength

For instance, the contour plots signify the impact of welding parameters on ultimate tensile strength (UTS). In Fig.4. 20 (a), the highest UTS is obtained at low current and moderate voltage (exceeding 520 MPa); it steadily decreases as the current increases, indicating that the current has the strongest negative effect on the tensile strength, while voltage has a moderate effect. Fig.4. 20 (b) shows that when a low current and high weld speed are used, UTS improves significantly to values above 520 MPa, while increasing the current lowers the UTS even at the higher speeds,

further proving that a higher current degrades UTS. In Fig.4. 20 (c), maximum UTS is achieved under low voltage and at very high welding speeds, but beyond that, the voltage would gradually degrade the strength down to around 500 MPa. Overall results indicate that low current, high speed of welding, and low-to-moderate voltage were found to provide the most favorable conditions for obtaining maximum tensile strength.

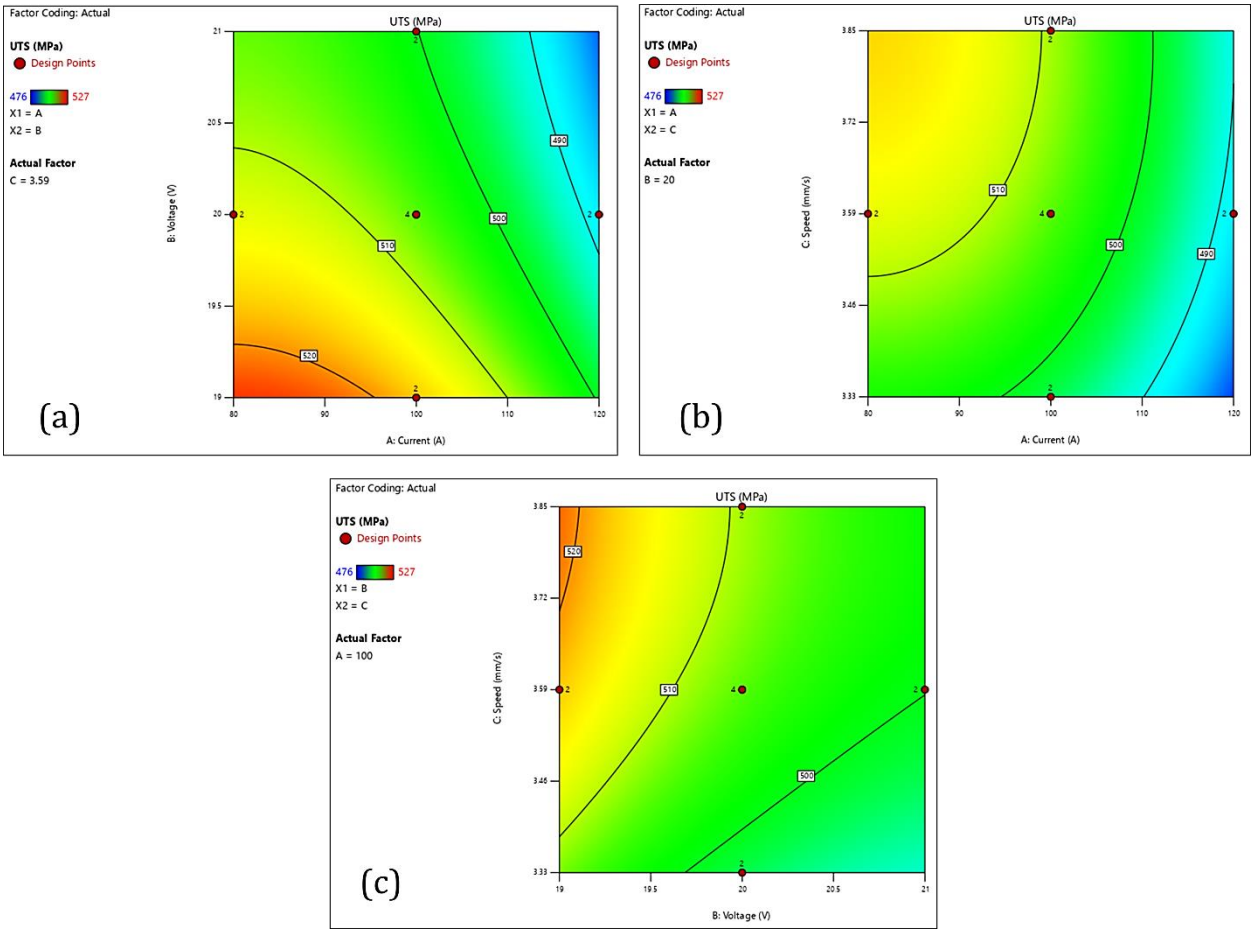

Fig.4. 20 Interaction analysis of ultimate strength (contour plot)

The contour plots indicate that ultimate tensile strength is maximized at elevated current levels and moderate voltage, combined with intermediate welding speed. Low heat input zones are associated with reduced tensile strength due to incomplete fusion and porosity formation. Excessive heat input, however, promotes grain coarsening and softening in the heat-affected zone, reducing UTS. Therefore, a balanced heat input regime optimizes metallurgical continuity and microstructural refinement, leading to superior tensile performance.

4.8.8.1 Comparison of experimental and predicted UTS Values

The table shows the actual value of ultimate tensile strength (UTS), measured from experiments, and the predicted values computed through the development of a statistical model. Across all 32 run orders, the predicted values closely match the experimental values, depicting deviations that are typically less than ±2MPa. For example, when Run 1 actual UTS was measured to be 502 MPa, the model predicted 502.46 MPa, and in Run 13, where 527 MPa was compared with the predicted 528.76 MPa. Moreover, run 10 showed that the actual UTS is 476 MPa, well matching the prediction from the model at 474.56 MPa. This shows that both the actual values and predicted values are close to each other, indicating better reliability in predictions of tensile strength by the model and good capturing of process parameter influences. It shows close alignment that will demonstrate the efficiency with which the developed regression model forecasts UTS within the studied range of parameters, as seen in Fig.4. 21.

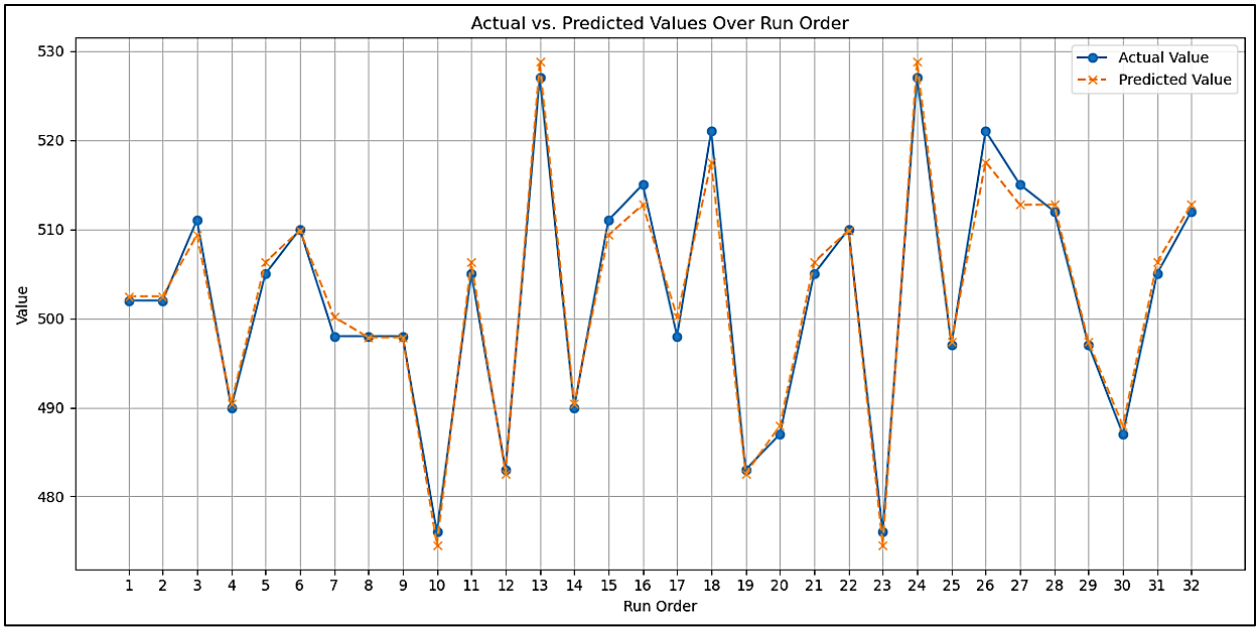

Fig.4. 21 Predicted vs. actual results of yield strength

4.8.9 Interaction analysis of strain at fracture

This 3D surface is a model that shows joint effects as far as the parameter of welding is concerned, on strain at fracture. In Fig.4. 22 (a), while the speed is fixed to run at 3.59 mm/s, current interacts with voltage and reveals that strain at fracture increases with an increase in the two parameters, reaching as high as about 24.6% at the highest settings of current and voltage, while the lowest, at about 21% occurs at lower settings of both. While in Fig.4. 22 (b), which is the test of current and

speed at constant voltage of 20 V, strain at fracture is highest at high current-low welding speed and at high speed and low-current-low ductility of up to 20%. This is also Fig.4. 22 (c), the effect voltage has on speed at a constant current of 100 A, indicating that strain increases only slightly with increased voltage but decreases quite significantly with greater welding speeds. Therefore, the findings indicate that current has the most positive effect on strain at fracture, that welding speed negatively influences ductility, and voltage is a positive contributor, but to a much lesser extent.

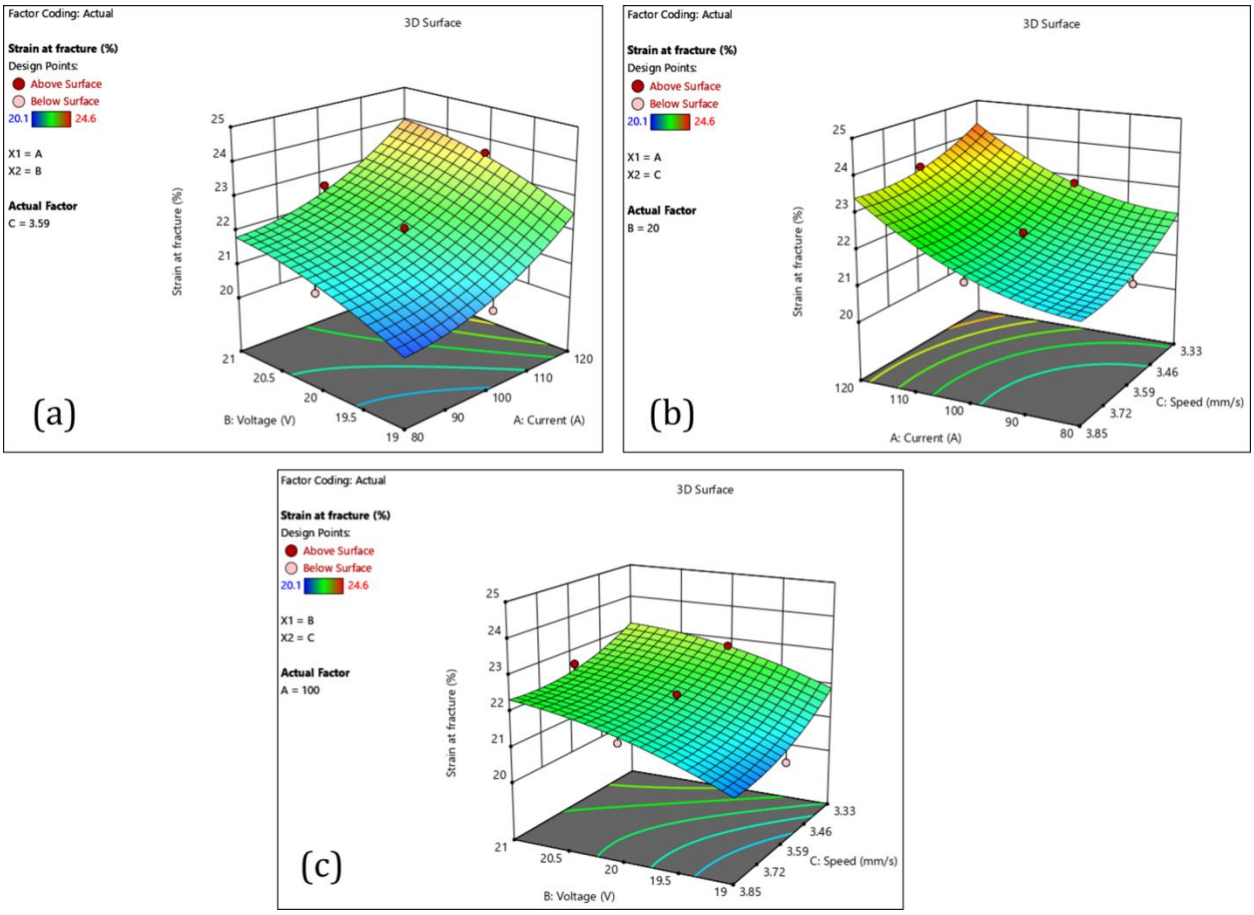

Fig.4. 22 Interaction analysis of strain at fracture (3D surface)

4.8.9.1 Contour Plots Showing the interaction effects of welding parameters on strain at fracture

The overall influence of the combinations of different welding parameters on strain at fracture is manifested through these contour plots. In Fig.4. 23 (a), current and voltage interact at a constant speed of 3.59 mm/s to show that as current increases to higher values with increasing voltage, the strain at fracture steadily increases, reaching almost values close to 24% in the upper range.

However, the lowest ductility at around 20% occurs at low current and voltage. Fig.4. 23 (b) shows the interaction effects produced by the current as well as the speed at a fixed voltage of 20 V. Here, the great improvement in strain at fracture occurs with increasing current, particularly at a lower speed, where it is close to 24% but drops at higher speeds and lower currents, where ductility heads toward 20%. Fig.4. 23 (c) demonstrates the actual interaction of voltage and speed while holding the current constant at 100 A. The outcome shows that strain at fracture improves slightly with increasing voltage, wherein the increment speedily lowers ductility such that the lowest values are high speed/low voltage combinations. Taken together, these findings indicate the sole importance of current in improving strain at fracture; welding speed has an adverse effect, and voltage is of moderate yet positive significance.

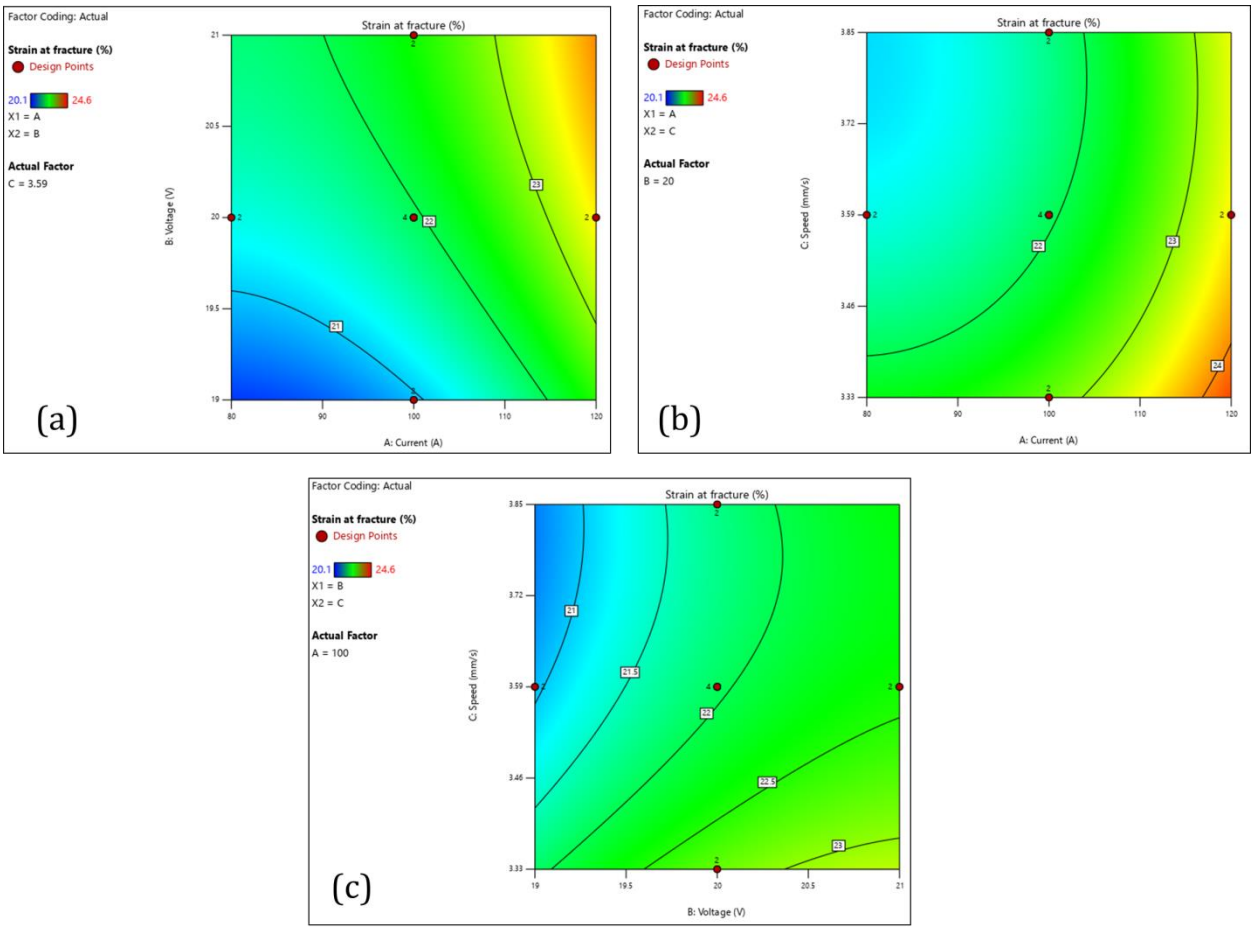

Fig.4. 23 Interaction analysis of strain at fracture (contour plot)

The contour plots demonstrate that ductility is most sensitive to welding speed and its interaction with voltage. Higher travel speeds generally increase strain at fracture due to reduced heat input and finer microstructural features, whereas excessively slow speeds lead to excessive heat

accumulation, grain growth, and embrittlement. Optimal ductility occurs at moderate voltage and higher welding speeds, where microstructural refinement and reduced residual stresses enhance plastic deformation capacity.

4.8.9.2 Comparison of actual and predicted values

Compared to model predictions, data collected from actual measurements are shown in Fig.4. 24 under 32 experimental runs. The column Run order defines the order of the experimentation process, while the actual value column refers to the measured data graphed in comparison with the predicted value. Thus, predicted and actual values match very closely, and differences (residuals) are mostly within an envelope of ±0.3, which shows that the model fits with the experimental data quite well. Some runs precisely agree, as runs 4, 14, 25, and 29, while most others have only small deviations. In some cases, such as runs 1 and 2 or runs 23 and 10, repeat conditions yield the same result, thereby adding to the evidence of the model's reliability, even for the worst-discrepant runs such as 16 and 18. However, even with such discrepancies, they are modest to suggest that the model is an excellent representation of the experimental outcomes.

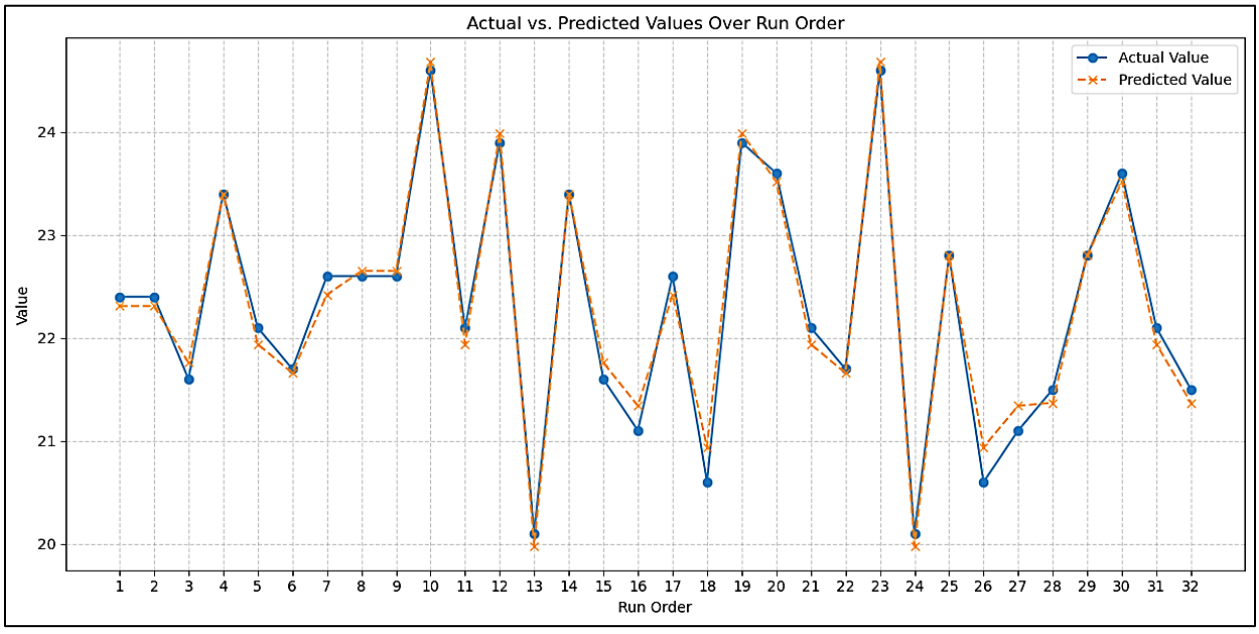

Fig.4. 24 Predicted vs. actual results of yield strength

4.8.10 Interaction analysis of hardness at weld zone

Hardness interaction analysis at the weld zone (WZ) has been demonstrated in the three response surface plots. The Fig.4. 25 (a) shows the current (A) and voltage (B) interaction with travel speed

(C) constant. Here, hardness increases appreciably with increasing current, whereas the voltage shows a much less pronounced positive effect. More of the interaction between current and voltage becomes evident in that the good effect of voltage is more pronounced in conjunction with increased current. Thus, hardness is maximized with a high current of about 115-120 A and moderate to high voltage of about 20.5-21 V, while at low current with a combination of mid-level voltage, hardness is minimized. In Fig.4. 25 (b), the interaction between current (A) and travel speed (C) is presented with the voltage kept constant. Again, current presents a strong positive effect on hardness, while the increase in travel speed dramatically lowers hardness. There exists a clear interaction between these two factors; increased travel speed has the most negative effect at low current, and the detrimental impact weakens at higher current. Therefore, hardness is highest at high current and low to moderate travel speed, while it is lowest at low current and high speed. In this case, Fig.4. 25 (c) illustrates the various combined effects of voltage (B) and travel speed (C) holding current constant. The two factors have a medium influence on hardness, with voltage increasing and speed decreasing hardness. Any real interaction between them is weak, and their effects work almost additively. The highest hardness is found at high voltage and low speed, while it is lowest at low voltage and high speed. Overall, the most influential parameter for hardness at the weld zone is current, followed by travel speed (as a negative influence) and voltage (as a positive influence). Current–voltage and current–speed appear to have stronger interactions, whereupon voltage-speed interactions are the weakest. Optimal hardness on the studied range occurred at higher current, higher voltage, and lower travel speed.

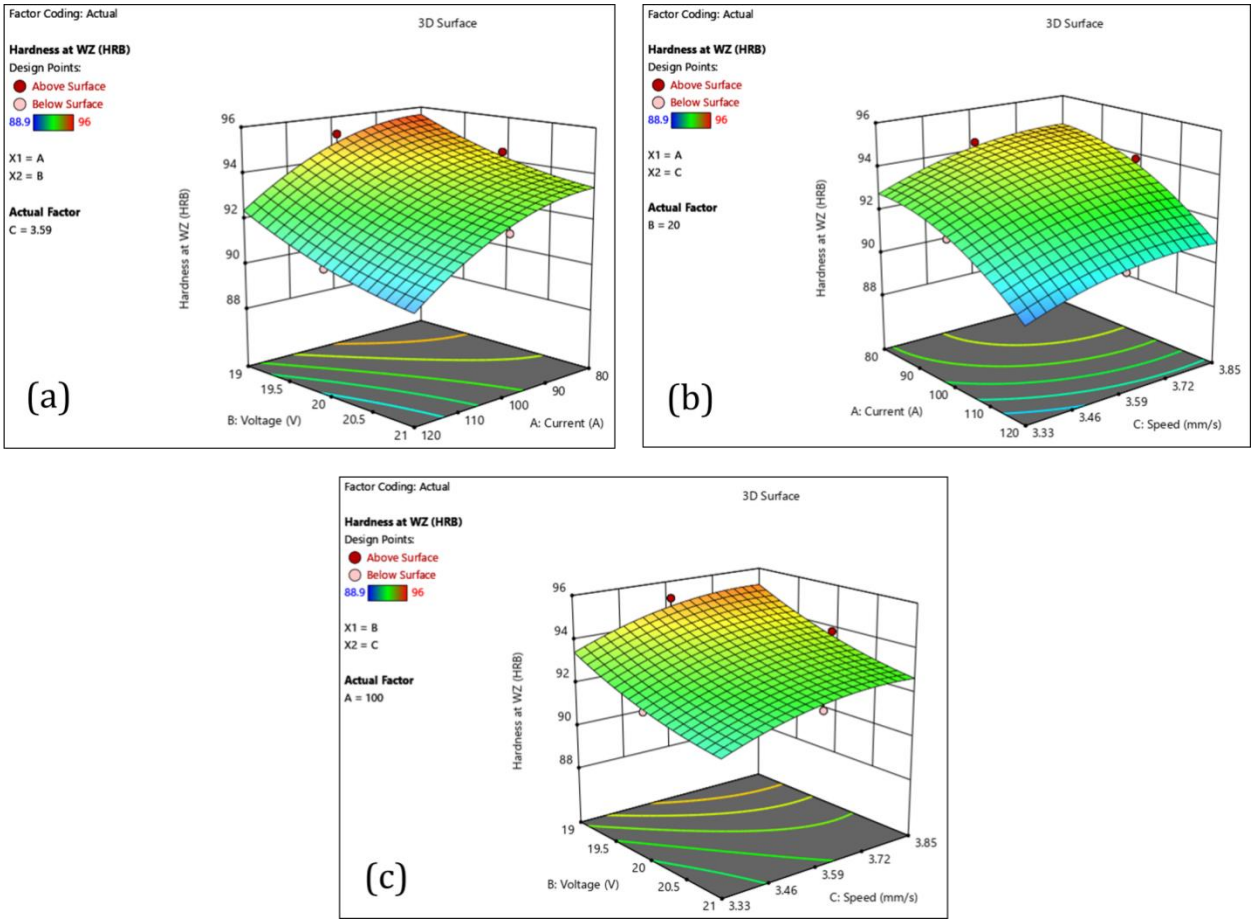

Fig.4. 25 Interaction analysis of hardness at the weld zone (3D surface)

4.8.11 Contour plot analysis of welding parameters on hardness

The contour diagrams show the interaction effects of welding parameters on hardness at a welded joint. In Fig.4. 26 (a), which figures the relationship between current, voltage, and constant speed, hardness seems to be higher for both parameters, while current obviously has a greater effect-the contours appear to curve slightly, with a suggestion of a mild interaction when voltage proves itself to be more effective at a higher current.

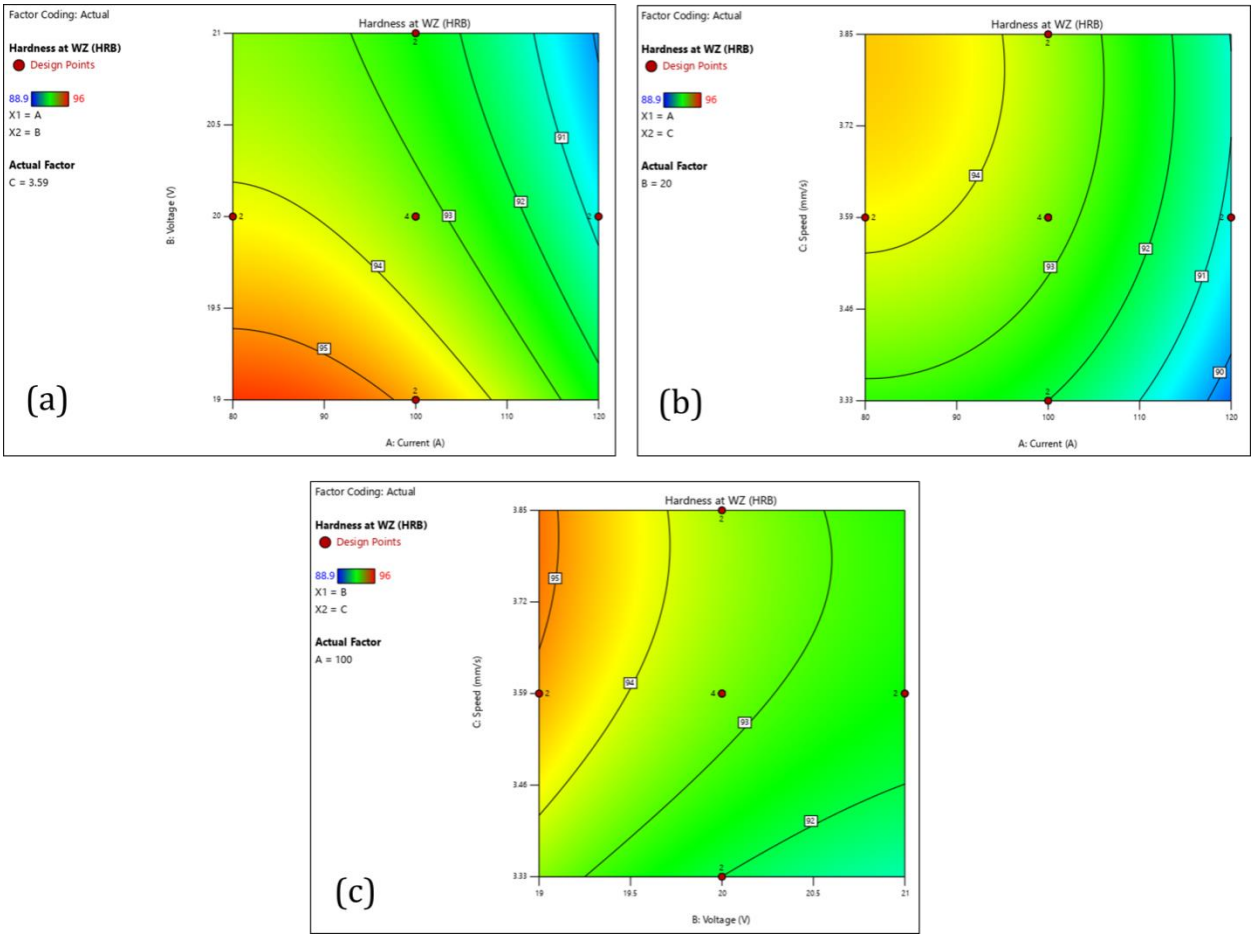

Fig.4. 26 Interaction analysis of hardness at the weld zone (contour plot)

In Fig.4. 26 (b), the current speed interaction with a given voltage is much more pronounced. Hardness in the weld zone increases with increasing welding current due to higher cooling rates and the formation of harder microstructural constituents such as bainite and acicular ferrite. However, excessively high current combined with low speed reduces hardness due to prolonged thermal exposure and grain coarsening. The contour plots identify an optimal region of moderate-to-high current and intermediate speed that maximizes hardness without compromising toughness. While hardness increases significantly with increasing current, at the same time it decreases with increasing speed, and the lowest observed values were at low current and high speed, while the maximum hardness is exhibited at high current and low speed. This shows the strong interaction between current and speed, wherein the effect is much more severe at low current. This is like holding the current constant and varying voltage and speed, as shown in Fig.4. 26 (c). Those two parameters have a positive effect on voltage on hardness and a negative effect on speed; however, the interaction between them is weak, as shown through nearly parallel contour lines. The optimum

condition in this case is attained at high voltage and low speed. Generally, it confirms that the contour analysis concludes that current is the most significant factor affecting hardness at the weld zone, followed by travel speed, which alleviates hardness, and then, fourthly, voltage, which has a moderate, positive influence. The highest current-weld hardness is produced using a combination of high current, high voltage, and low travel speed.

4.8.11.1 Comparison of actual and predicted hardness values

This table compares actual measured data to model-predicted values for 32 experimental runs. The run order gives the relevant order of tests; the actual value shows the observed hardness at the weld zone, while the predicted value describes the corresponding estimates made by the model. The results show that the predicted values match very closely with the actual measurements, with the difference (residual) mostly ranging between ±0.2, which shows very good agreement of the model with the experimental data. Some runs, such as 4 and 14 or 23 and 10, show nearly identical actual and predicted values, confirming the very good reliability and reproducibility of the model. For some runs, like 16 and 18, there is a slight deviation, but they still fall in an extremely small range, which is proof of the great accuracy of the model prediction. Overall, the table reinforces the assertion that the model describes the experimental behavior of weld-hardness with minimal error and can thus be used reliably for prediction and analysis, as shown in Fig.4. 27.

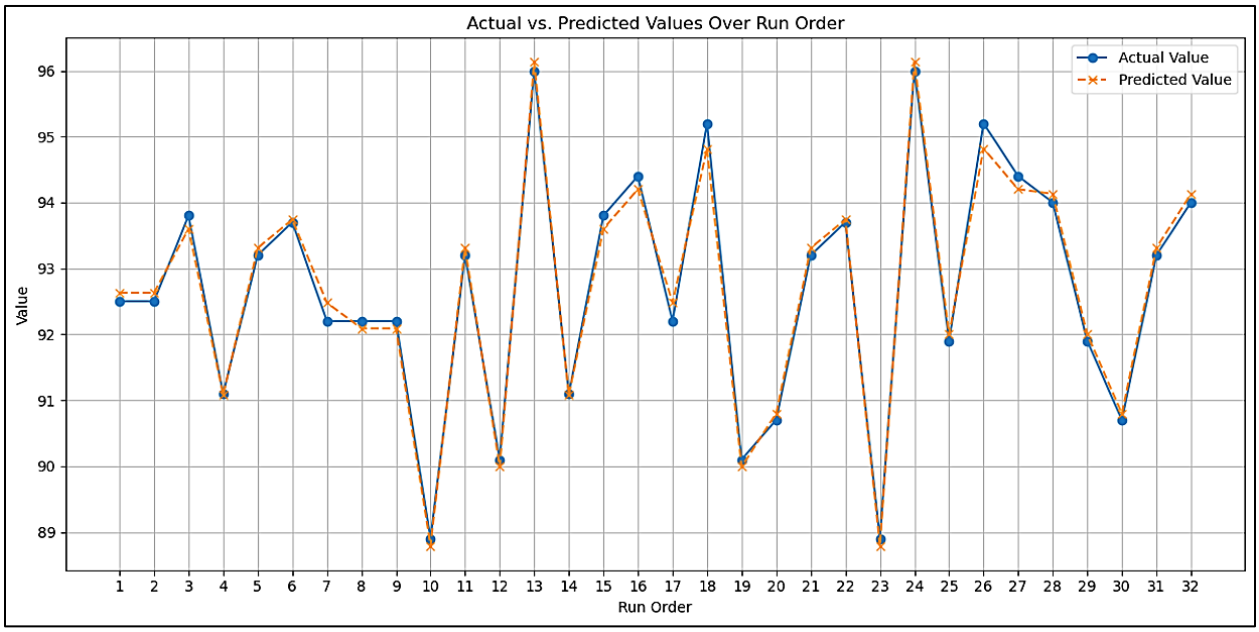

Fig.4. 27 Comparison of actual and predicted hardness values

4.8.12 Interaction analysis of hardness at heat heat-affected zone

Fig.4. 28 are the 3D surface plots borne out of a Response Surface Methodology (RSM) research study on the influences of current (A), voltage (B), and speed (C) on hardness measured in Rockwell B at the heat-affected zone (HAZ). The range of colors in the scale is low hardness (approximately 83.9 HRB) in blue to high hardness (~89.6 HRB) in red.

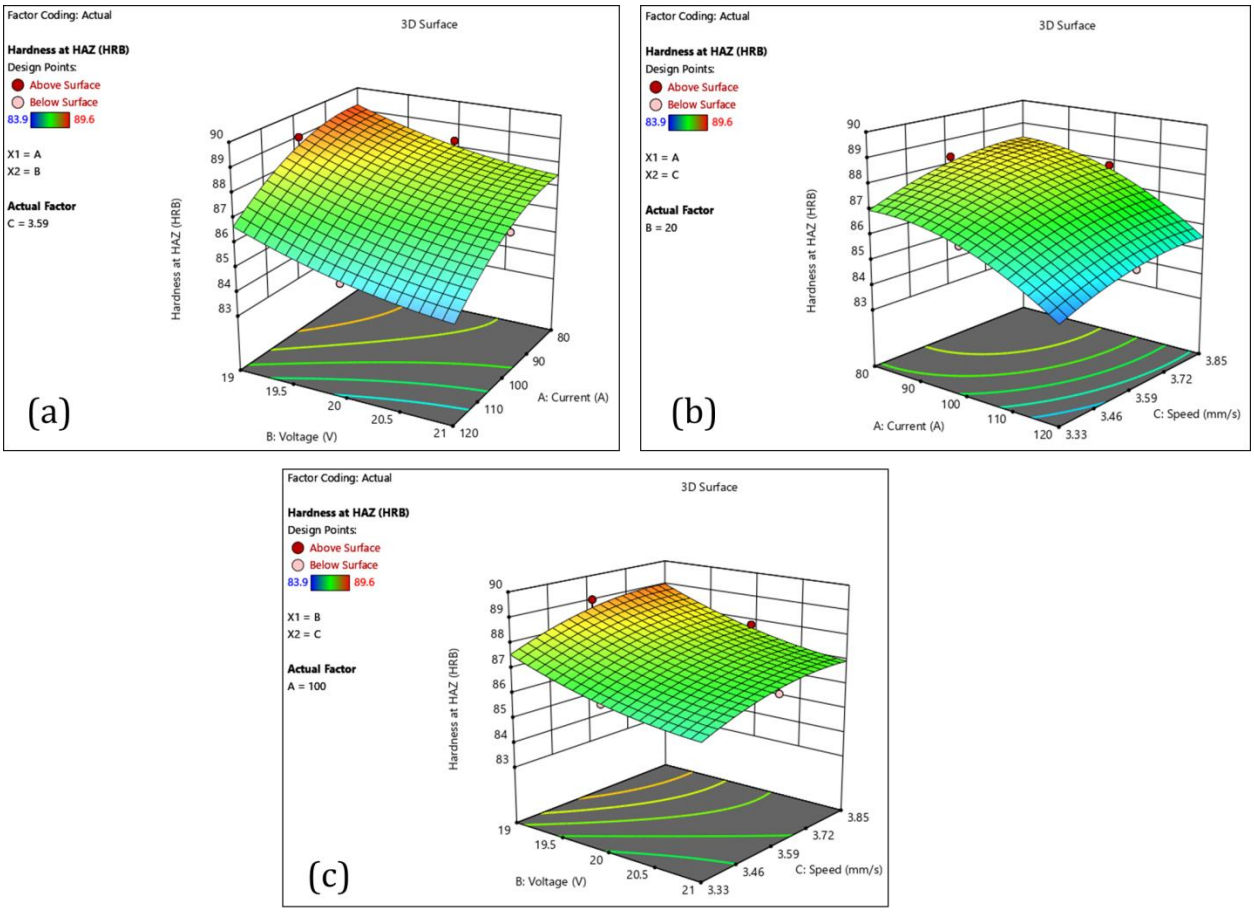

Fig.4. 28 Interaction analysis of hardness at heat heat-affected zone (3D surface)

It shows that with less current and more voltage, the maximum ends at approximately 80 A and about 21 V, while the lowest goes down to about 120 A with approximately 19 V (Speed = 3.59 mm/s) from Fig.4. 28 (a). A remarkable negative correlation based on Fig.4. 28 (a) and (b) exists between current and hardness above the threshold of ~80 A at any speed (Voltage = 20 V). In Fig.4. 28(c), it can be inferred that the hardness increases with increasing voltage, attaining a maximum at above say high voltage (~21 V) and low speed (3.33 mm/s), while at low voltage

(~19 V), speed is practically irrelevant (Current = 100 A). In this case, it would be high hardness from low current, high voltage, and low speed.

4.8.13 Contour plot analysis of process parameters affecting HAZ hardness

Three two-dimensional contour plots that depict Current (A), Voltage (B), and Speed (C) with respect to Hardness, at the Heat-Affected Zone (HAZ), defined in HRB, are visible through the Fig.4. 29.

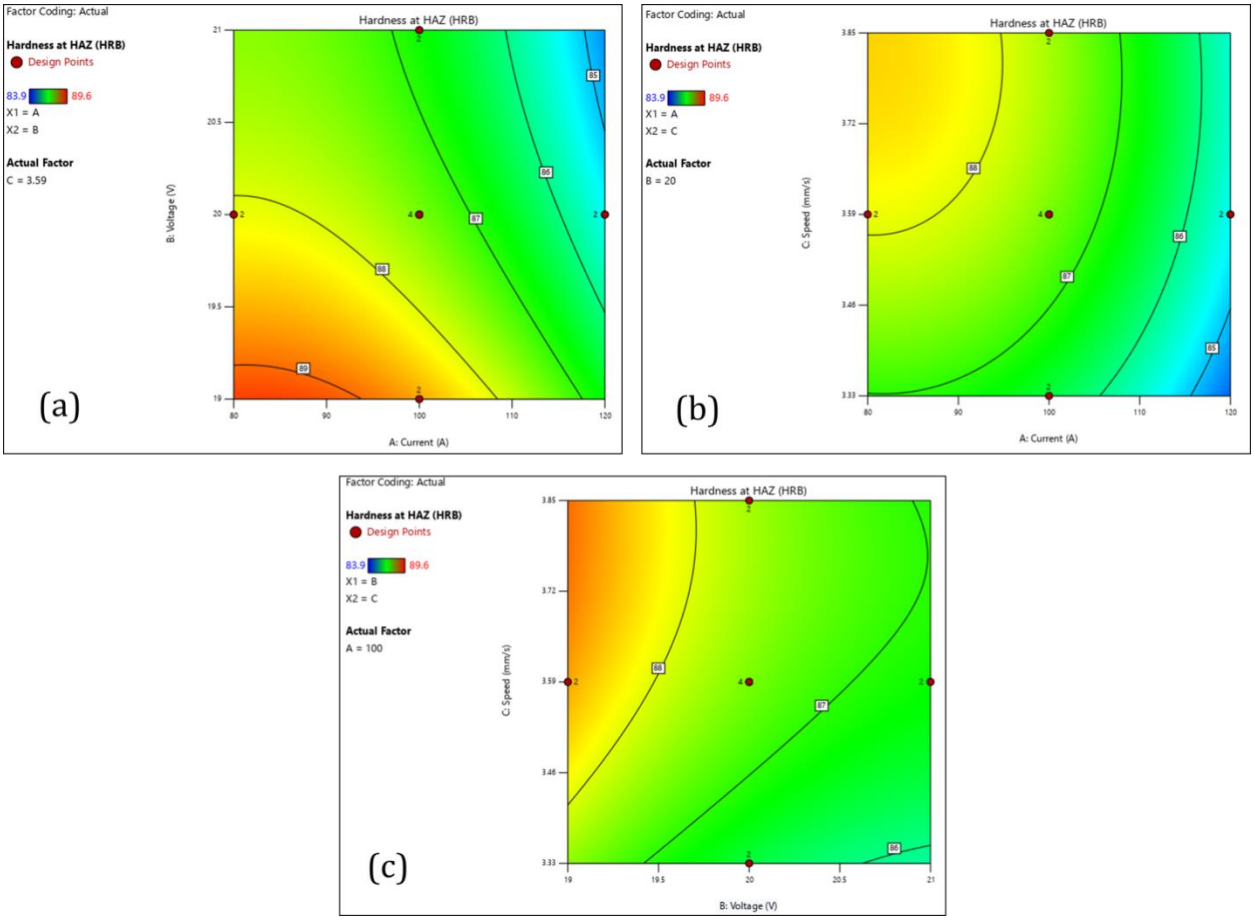

Fig.4. 29 Interaction analysis of hardness at heat heat-affected zone (contour plot)

The contour plots show that HAZ hardness is primarily governed by welding current and travel speed. High current and low speed conditions increase peak temperatures and promote grain coarsening, reducing hardness in the softened HAZ. Conversely, moderate current and higher speed reduce heat input, refining microstructure and increasing hardness. The optimal region corresponds to moderate current and moderate-to-high speed combinations that balance phase transformation kinetics and cooling rate effects. The blue ~83.9 HRB is the lowest in hardness, and to red ~89.6 HRB is the highest in hardness. Contour lines link points of equal hardness. Fig.4.

29 (a) demonstrates Current versus Voltage interaction at an unchanging Speed of 3.59 mm/s to obtain higher hardness at decreased current (80-90 A) and low voltage (~19 V), whereas the lowest hardness is at high current and voltage. Fig.4. 29 (b) presents that Current, when Voltage is pegged at a constant 20 V, holds primacy because hardness consistently reduces with increasing current, while Speed has demonstratively minimal effect. Fig.4. 29 (c), showing the Current fielded at 100 A, exhibits interaction between Voltage and Speed: optimum hardness is generated at low voltage (~19 V) with high speed (~3.85 mm/s), whereas, at high voltage (~21 V) and low speed (~3.33 mm/s), hardness drops. Thus, the lower current with specific voltage-speed settings gives maximum hardness in the HAZ.

4.8.13.1 Comparison of actual and predicted HAZ hardness

The table shows a comparison of the measured and predicted Hardness values (HRB) for 32 experimental runs at HAZ. The predicted values closely follow the measured values, with significant differences generally under 0.2 HRB, indicating that the RSM model was probably used. For example, run 1 has an actual hardness of 86.80 HRB with a predicted value of 86.93 HRB. Hence, the close matching of hardness values for all the runs would suggest that the model is capable of reliably capturing the process parameters' effect on HAZ hardness, as shown in Fig.4. 30.

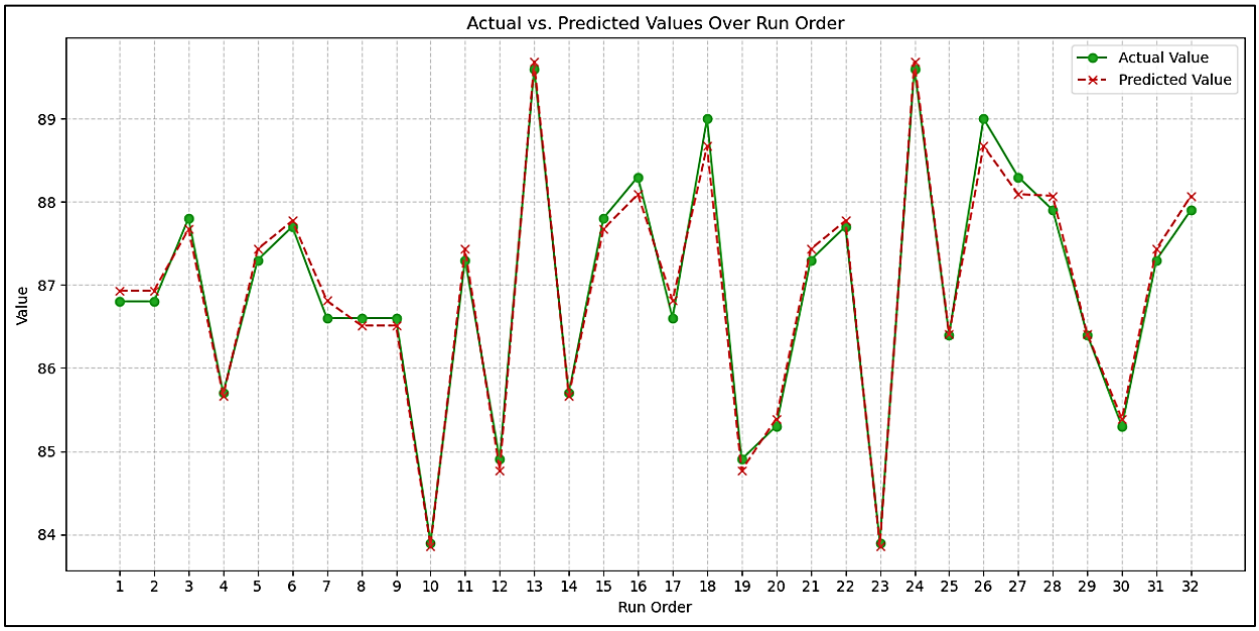

Fig.4. 30 Comparison of actual and predicted HAZ hardness

4.8.14 Desirability function analysis

Table 4. 7 summarizes the DFA solutions obtained for the MIG welding process parameters and their corresponding mechanical property responses. Using the desirability function approach, a total of 76 possible parameter combinations were evaluated, considering welding current, voltage, and speed against target responses: yield strength, ultimate tensile strength (UTS), strain at fracture, and hardness at both the weld zone (WZ) and the heat-affected zone (HAZ). Among these, Solution 1 emerged as the most balanced, achieving the highest desirability value of 0.671. This optimal solution corresponds to a welding current of 99.35 A, voltage of 20.90 V, and speed of 3.54 mm/s, producing predicted mechanical properties of 403.51 MPa yield strength, 499.71 MPa UTS, 22.47% strain at fracture, 92.41 HV hardness at the WZ, and 86.75 HV hardness at the HAZ. The associated standard errors were minimal, indicating high confidence in the predicted values. Across solutions 1 to 75, desirability values remained very close, ranging from 0.666 to 0.671, suggesting that multiple parameter settings can achieve comparably effective results. Minor variations in current, voltage, and speed led to negligible changes in predicted responses, reinforcing the robustness of the optimization model. In this set, yield strength consistently ranged around 403–404 MPa, UTS around 499–500 MPa, strain at fracture between 22.46–22.54%, and hardness values at the WZ and HAZ fluctuated minimally around 92.39–92.45 HV and 86.74–86.75 HV, respectively. An exception is Solution 76, which showed markedly different responses: yield strength of 408.79 MPa, UTS of 506.3 MPa, reduced strain at fracture of 21.94%, and increased hardness values (93.31 HV at WZ and 87.43 HV at HAZ). Despite seemingly improved strength and hardness, the desirability dropped sharply to 0.004, reflecting an imbalance caused by reduced ductility. This highlights that high strength alone does not guarantee optimal weld quality. Thus, the optimization results demonstrate that the selected parameters in Solution 1 offer the most balanced and reliable combination, achieving an adequate trade-off between strength, ductility, and hardness distribution. The corresponding desirability index of 0.671 indicates a satisfactory compromise between competing responses, acknowledging that maximizing one property often reduces another. Fig.4. 31 illustrates the DFA ramp plots, showing the relationship between process parameters and mechanical property responses, and confirming the practical applicability of the developed model for achieving desirable weld quality in MIG welding.

Although higher welding current and lower travel speed enhance yield strength and ultimate tensile strength by improving fusion and penetration, these conditions simultaneously reduce ductility due

to increased heat input, grain coarsening, and elevated residual stresses. Conversely, higher welding speeds and lower heat input promote finer microstructures and improved strain at fracture but may compromise strength if fusion becomes incomplete. The desirability-based multi-objective optimization framework effectively balances these competing responses by identifying parameter combinations that provide near-maximum strength while maintaining acceptable ductility levels. This compromise is essential for structural applications where excessive hardness and strength without sufficient ductility may increase susceptibility to brittle fracture, whereas excessive ductility without adequate strength limits load-bearing capacity. Therefore, the optimized welding parameters represent a practical engineering solution that ensures both structural safety and mechanical reliability.

Table 4. 7 DFA Solutions

Number	Current	Voltage	Speed	Yield strength	StdErr(Yield strength)	UTS	StdErr(UTS)	Strain at fracture	StdErr(Strain at fracture)	Hardness at WZ	StdErr(Hardness at WZ)	Hardness at HAZ	StdErr(Hardness at HAZ)	Desirability	
1	**99.352**	**20.904**	**3.535**	**403.513**	**0.628**	**499.**	**0.811**	**22.467**	**0.080**	**92.408**	**0.090**	**86.750**	**0.080**	**0.671**	**Selected**
2	99.538	20.903	3.540	403.521	0.628	499.7	0.812	22.467	0.080	92.409	0.090	86.750	0.080	0.671	
3	99.096	20.906	3.529	403.502	0.628	499.7	0.812	22.468	0.080	92.407	0.090	86.750	0.080	0.671	
4	99.708	20.902	3.544	403.528	0.628	499.7	0.811	22.467	0.080	92.409	0.090	86.750	0.080	0.671	
5	99.937	20.901	3.550	403.538	0.628	499.7	0.812	22.466	0.080	92.410	0.090	86.750	0.080	0.671	
6	100.051	20.900	3.553	403.542	0.627	499.7	0.811	22.467	0.080	92.411	0.090	86.750	0.080	0.671	
7	98.438	20.910	3.515	403.477	0.628	499.7	0.812	22.469	0.080	92.404	0.090	86.750	0.080	0.671	
8	100.210	20.900	3.557	403.548	0.628	499.7	0.812	22.466	0.080	92.411	0.090	86.750	0.080	0.671	
9	98.110	20.912	3.509	403.466	0.628	499.7	0.812	22.469	0.080	92.403	0.091	86.750	0.080	0.671	
10	100.384	20.900	3.562	403.556	0.628	499.7	0.812	22.466	0.080	92.412	0.091	86.750	0.080	0.671	
11	100.492	20.899	3.565	403.561	0.628	499.7	0.812	22.466	0.080	92.413	0.090	86.750	0.080	0.671	
12	97.974	20.912	3.506	403.462	0.627	499.7	0.811	22.469	0.080	92.402	0.090	86.750	0.080	0.671	
13	97.777	20.913	3.502	403.456	0.627	499.7	0.811	22.470	0.080	92.401	0.090	86.750	0.080	0.671	
14	97.611	20.914	3.499	403.451	0.628	499.7	0.811	22.470	0.080	92.401	0.090	86.750	0.080	0.671	
15	100.713	20.899	3.572	403.572	0.628	499.7	0.812	22.466	0.080	92.414	0.090	86.750	0.080	0.671	
16	97.352	20.916	3.494	403.443	0.628	499.7	0.811	22.470	0.080	92.400	0.090	86.750	0.080	0.671	
17	97.213	20.917	3.492	403.438	0.628	499.7	0.812	22.470	0.080	92.399	0.090	86.750	0.080	0.671	

18	100.998	20.898	3.581	403.586	0.628	499.7	0.812	22.465	0.080	92.415	0.091	86.750	0.080	0.671
19	101.053	20.899	3.583	403.591	0.629	499.7	0.813	22.465	0.080	92.415	0.091	86.750	0.080	0.671
20	96.585	20.921	3.482	403.422	0.628	499.7	0.812	22.471	0.080	92.397	0.091	86.750	0.080	0.671
21	101.271	20.897	3.590	403.603	0.628	499.7	0.811	22.465	0.080	92.416	0.090	86.750	0.080	0.671
22	101.328	20.897	3.592	403.605	0.627	499.7	0.811	22.465	0.080	92.416	0.090	86.750	0.080	0.671
23	96.385	20.922	3.478	403.417	0.628	499.7	0.812	22.471	0.080	92.397	0.091	86.750	0.080	0.671
24	96.193	20.922	3.475	403.413	0.628	499.7	0.811	22.472	0.080	92.396	0.090	86.750	0.080	0.671
25	95.987	20.923	3.472	403.409	0.628	499.7	0.812	22.472	0.080	92.396	0.090	86.750	0.080	0.671
26	101.524	20.898	3.600	403.617	0.628	499.7	0.811	22.465	0.080	92.418	0.090	86.750	0.080	0.671
27	101.641	20.899	3.605	403.624	0.628	499.7	0.812	22.465	0.080	92.418	0.091	86.750	0.080	0.671
28	95.639	20.926	3.467	403.403	0.629	499.7	0.813	22.472	0.081	92.395	0.091	86.750	0.080	0.671
29	95.286	20.926	3.462	403.395	0.628	499.7	0.812	22.473	0.080	92.394	0.090	86.750	0.080	0.671
30	95.142	20.926	3.460	403.393	0.628	499.7	0.811	22.473	0.080	92.394	0.090	86.750	0.080	0.671
31	94.979	20.926	3.458	403.391	0.627	499.7	0.810	22.473	0.080	92.394	0.090	86.750	0.080	0.671
32	94.838	20.927	3.456	403.388	0.628	499.7	0.811	22.473	0.080	92.393	0.090	86.750	0.080	0.671
33	94.264	20.929	3.449	403.382	0.628	499.7	0.812	22.473	0.080	92.393	0.091	86.750	0.080	0.671
34	94.105	20.928	3.447	403.380	0.627	499.7	0.811	22.474	0.080	92.392	0.090	86.750	0.080	0.671
35	93.744	20.930	3.443	403.375	0.628	499.7	0.812	22.474	0.080	92.392	0.090	86.750	0.080	0.671
36	102.200	20.901	3.629	403.660	0.627	499.7	0.810	22.465	0.080	92.421	0.090	86.750	0.080	0.671
37	93.145	20.930	3.436	403.373	0.628	499.7	0.812	22.474	0.080	92.391	0.090	86.750	0.080	0.671
38	102.363	20.905	3.639	403.672	0.628	499.7	0.812	22.465	0.080	92.422	0.090	86.750	0.080	0.671
39	92.793	20.929	3.432	403.371	0.627	499.7	0.811	22.474	0.080	92.391	0.090	86.750	0.080	0.671
40	92.612	20.931	3.430	403.371	0.628	499.7	0.812	22.474	0.080	92.391	0.091	86.750	0.080	0.671
41	92.231	20.929	3.426	403.371	0.628	499.8	0.811	22.475	0.080	92.391	0.090	86.750	0.080	0.671
42	91.885	20.929	3.423	403.370	0.628	499.8	0.811	22.475	0.080	92.390	0.090	86.750	0.080	0.671
43	91.243	20.930	3.417	403.372	0.630	499.8	0.814	22.475	0.081	92.391	0.091	86.750	0.080	0.671
44	89.307	20.919	3.401	403.395	0.629	499.8	0.813	22.474	0.081	92.392	0.091	86.750	0.080	0.671
45	88.940	20.910	3.398	403.407	0.626	499.8	0.809	22.474	0.080	92.394	0.090	86.750	0.080	0.671
46	88.531	20.910	3.396	403.414	0.629	499.8	0.813	22.474	0.080	92.394	0.091	86.750	0.080	0.671
47	87.885	20.903	3.392	403.432	0.629	499.9	0.813	22.473	0.080	92.396	0.091	86.750	0.080	0.671

48	87.702	20.899	3.391	403.438	0.628	499.9	0.812	22.473	0.080	92.397	0.091	86.750	0.080	0.671
49	86.488	20.875	3.383	403.487	0.628	499.9	0.812	22.472	0.080	92.402	0.090	86.750	0.080	0.671
50	85.145	20.832	3.376	403.563	0.630	500.0	0.814	22.470	0.081	92.410	0.091	86.750	0.080	0.670
51	116.299	19.171	3.537	403.947	0.627	500.0	0.811	22.484	0.080	92.450	0.090	86.750	0.080	0.670
52	116.337	19.173	3.540	403.948	0.628	500.0	0.812	22.483	0.080	92.450	0.090	86.749	0.080	0.670
53	116.404	19.178	3.545	403.955	0.628	500.0	0.812	22.482	0.080	92.450	0.090	86.749	0.080	0.670
54	116.440	19.182	3.548	403.957	0.628	500.0	0.812	22.482	0.080	92.450	0.090	86.749	0.080	0.670
55	116.490	19.186	3.552	403.961	0.628	500.0	0.812	22.481	0.080	92.450	0.090	86.748	0.080	0.670
56	116.520	19.190	3.555	403.964	0.628	500.0	0.811	22.481	0.080	92.450	0.090	86.748	0.080	0.670
57	116.639	19.201	3.566	403.976	0.627	500.0	0.811	22.479	0.080	92.450	0.090	86.747	0.080	0.669
58	116.712	19.207	3.573	403.983	0.627	500.0	0.811	22.478	0.080	92.450	0.090	86.747	0.080	0.669
59	116.782	19.211	3.579	403.991	0.628	500.0	0.812	22.477	0.080	92.450	0.090	86.747	0.080	0.669
60	116.802	19.213	3.581	403.992	0.628	500.0	0.812	22.477	0.080	92.450	0.090	86.746	0.080	0.669
61	116.830	19.215	3.583	403.994	0.628	500.0	0.812	22.477	0.080	92.450	0.090	86.746	0.080	0.669
62	116.984	19.222	3.595	404.009	0.629	500.0	0.813	22.475	0.081	92.450	0.091	86.746	0.080	0.669
63	117.512	19.249	3.646	404.068	0.628	500.1	0.811	22.468	0.080	92.450	0.090	86.744	0.080	0.669
64	88.150	20.377	3.348	403.775	0.626	500.3	0.809	22.491	0.080	92.434	0.090	86.750	0.080	0.669
65	92.029	20.212	3.350	403.760	0.627	500.3	0.811	22.504	0.080	92.434	0.090	86.750	0.080	0.668
66	98.041	19.901	3.356	403.765	0.627	500.3	0.810	22.519	0.080	92.436	0.090	86.750	0.080	0.668
67	109.126	19.202	3.362	403.680	0.627	500.2	0.811	22.538	0.080	92.426	0.090	86.750	0.080	0.668
68	101.998	19.630	3.352	403.747	0.627	500.3	0.811	22.530	0.080	92.434	0.090	86.750	0.080	0.667
69	103.226	19.546	3.351	403.735	0.626	500.3	0.810	22.533	0.080	92.432	0.090	86.750	0.080	0.667
70	104.958	19.430	3.350	403.716	0.627	500.3	0.810	22.537	0.080	92.430	0.090	86.750	0.080	0.667
71	107.512	20.315	3.831	404.264	0.627	500.6	0.810	22.490	0.080	92.450	0.090	86.745	0.080	0.667
72	109.778	20.069	3.828	404.303	0.626	500.7	0.810	22.487	0.080	92.450	0.090	86.742	0.080	0.666
73	110.117	20.033	3.828	404.307	0.627	500.7	0.810	22.487	0.080	92.450	0.090	86.742	0.080	0.666
74	111.683	19.874	3.827	404.326	0.627	500.7	0.810	22.482	0.080	92.450	0.090	86.742	0.080	0.666
75	111.567	19.886	3.827	404.324	0.626	500.7	0.809	22.483	0.080	92.450	0.090	86.742	0.080	0.666
76	100.000	20.000	3.590	408.793	0.463	506.3	0.599	21.941	0.059	93.307	0.067	87.428	0.059	0.004

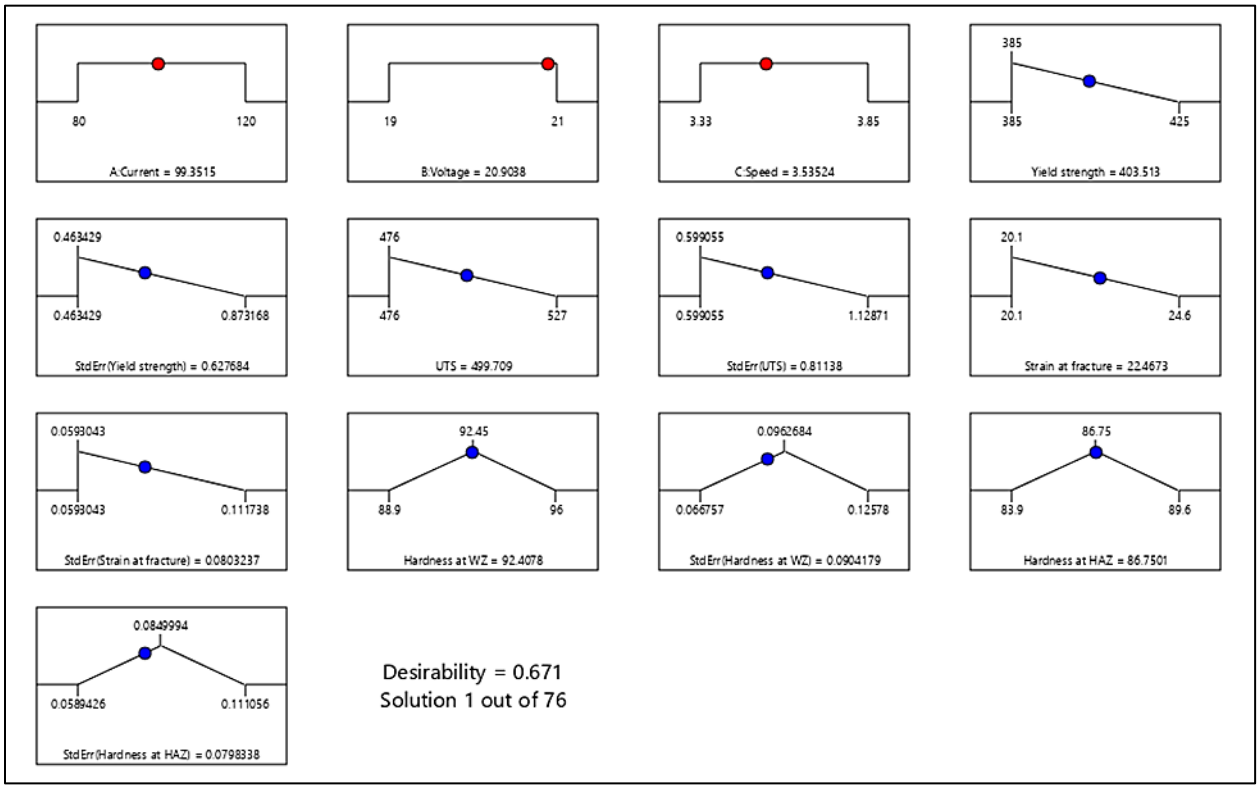

Fig.4. 31 Desirability ramp plots illustrating the optimization of welding current (A), voltage (V), and travel speed (mm/s) to simultaneously maximize yield strength (MPa), ultimate tensile strength (MPa), strain at fracture (%), weld zone hardness (HRB), and HAZ hardness (HRB), along with the resulting overall composite desirability.

4.8.14.1 Comprehensive interpretation of the desirability optimization results

Desirability charts in Fig.4. 32 outline selected process parameters like current, voltage and speed vis-a-vis optimization. Desirability value of 1 hint that the parameter levels conform to the desired range. In the case of responses, the only value that achieved desirability of 1 was for hardness at the heat-affected zone (HAZ) and that of weld zone (WZ) came close at 0.988. Also, standard errors for hardness at both HAZ and WZ scored high (≈0.802), which indicate good precision. Yield strength (0.537), ultimate tensile strength (0.535), and strain at fracture (0.474) achieved only moderate goals, hence, revealing a compromise of strength and ductility compared to hardness. The standard errors for these properties were around 0.599, thus, they were reasonably predicted, if not too accurately. With a desirability value of 0.671, the trade-off is acceptable for all objectives, mostly due to the good result in hardness, while being compromised by lower scores in strength and ductility. Overall, the solution prioritizes optimization on hardness, while better

adjustment of factors weight or constraints in the optimization settings requires harsher bending on tensile properties and fracture strain optimization.

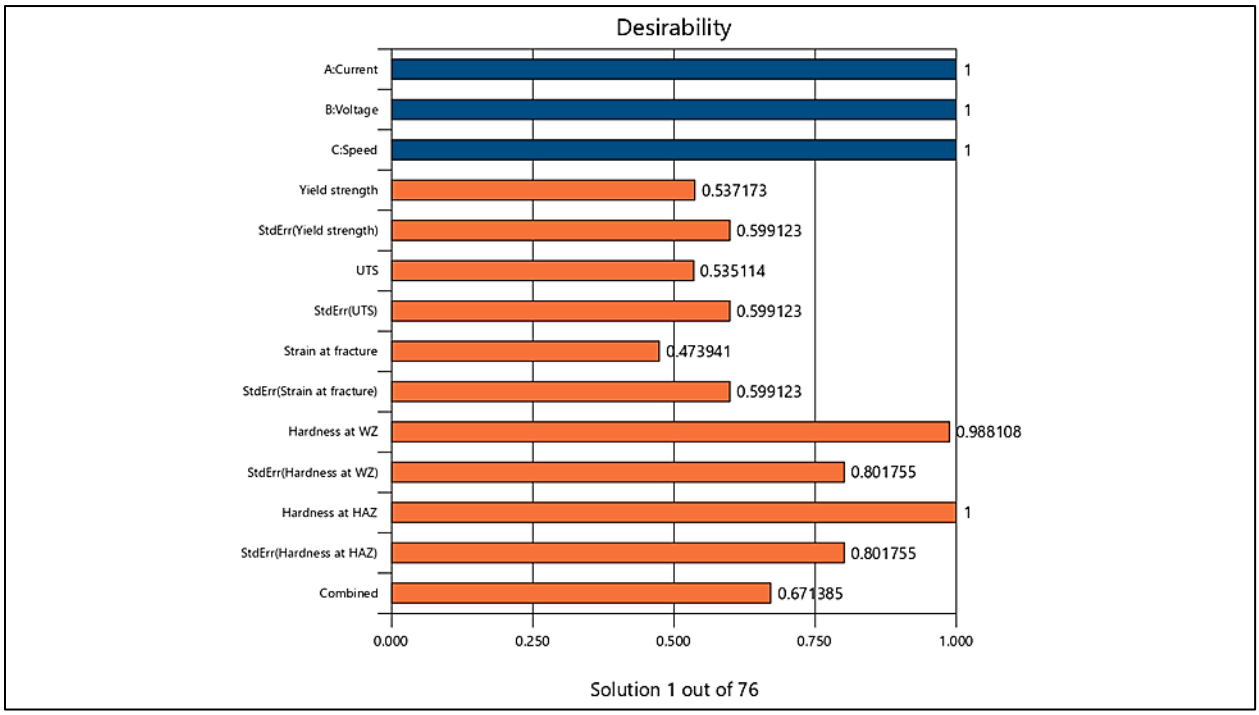

Fig.4. 32 Multi-response trade-off visualization showing the desirability interaction between strength (yield and ultimate tensile strength), ductility (strain at fracture), and hardness responses under optimized MIG welding parameter conditions.

4.8.14.2 Contour plot analysis of desirability across current and voltage parameters

The contour Fig.4. 33 shows the variation of desirability against current (measured in Amperes) and voltage (measured in Volts) while keeping speed constant at 3.53524. The highest desirability values approaching 1.0 are shown in green and yellow. The plot's most central region is bluish, denoting that the combinations of current and voltage don't meet optimization goals, which show very low desirability. As you proceed toward the boundary regions, the desirability would keep on increasing until you find contour lines denoting values above 0.5. The identified optimum point is located at a desirability level of 0.671, slightly above 20.5 V for voltage and around 100 A for current. This means that the window of operation within which acceptable optimization could be realized is narrow. Inasmuch as the solution represents a reasonable trade-off in optimized hardness, it bears a lower level of satisfaction for the target objectives of tensile strength and ductility thereby showing the tradeoffs that exist in the selection of process parameters.

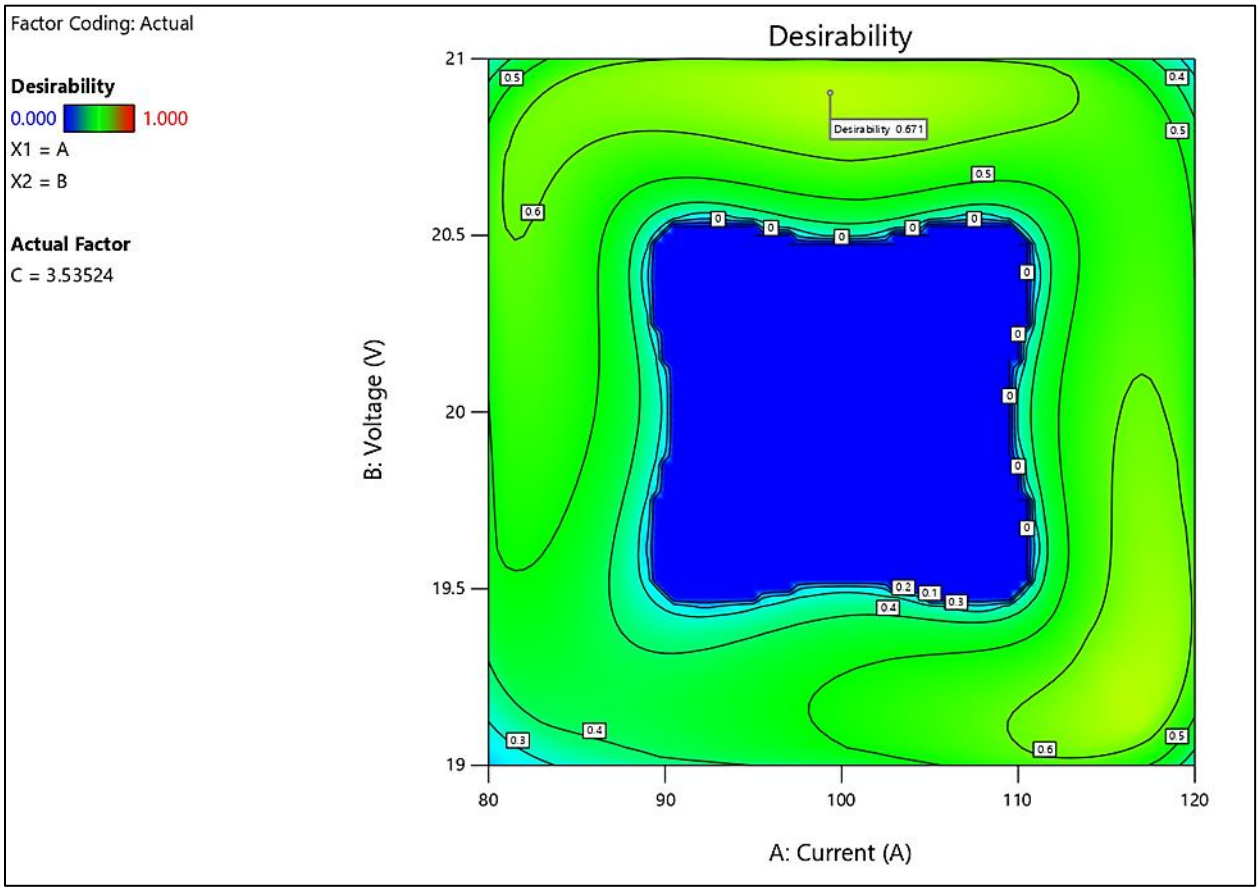

Fig.4. 33 Optimization window for achieving balanced mechanical properties

4.8.14.3 Contour plot of desirability across current and speed parameters

In Fig.4. 34 Current (A) and speed (C) were correlated to the overall desirability, while the voltage (B = 20.9038 V) remained constant. Below lies the color gradient showing levels of desirability; blue means the values are low (close to 0), while green to yellow means the higher values (approaching 1). In contrast to the last plot, green shades dominate the present design space, inferring that most current-speed combinations give moderate desirability values in the range of 0.4 to 0.6. The optimal solution, with a desirability of 0.671, lies around a current of about 100 A and speed of 3.55 mm/s or so, being situated in a zone of reasonably higher desirability. This means that the interaction of current and speed provides a greater workable range compared to current-voltage combinations, since here the desirability is more evenly spread across the region. However, the plot indicates slight dips towards the extreme edges where the desirability goes below 0.3, implying that working at very high or very low current and speed values should be avoided. Thus, this contour delineates the comfort of a wider operating window for balancing

hardness, strength, and ductility with the optimal point providing a fair trade-off among these responses.

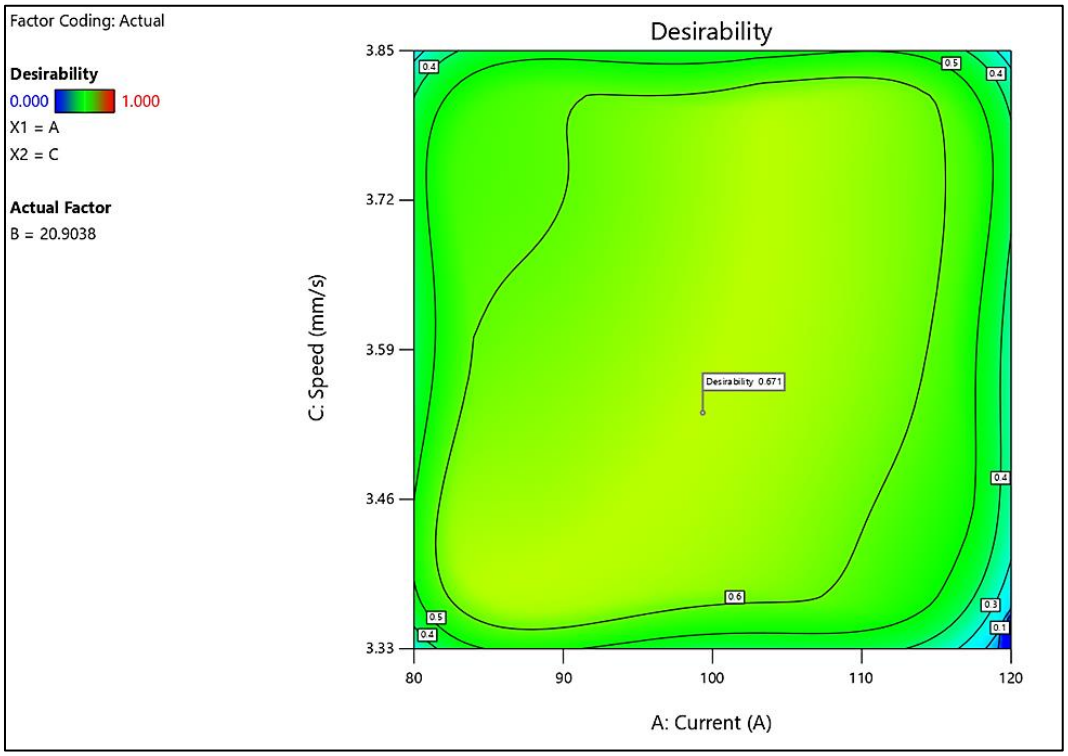

Fig.4. 34 Correlated to the overall desirability across current and speed parameters

4.8.14.4 Interpretation of the desirability contour plot

The desirability contour in Fig.4. 35 illustrates how the combined performance of the process varies with Voltage (B) and Speed (C) while Factor A is fixed at 99.3515. The color scale ranges from blue, representing a desirability of zero (unacceptable), to green and yellow regions indicating moderate values, and approaching red for the highest desirability near one. A large blue area dominates the center of the plot (B ≈ 19.5–20.5 V and C ≈ 3.46–3.72 mm/s), showing that within this region at least one response fails to meet its required specification, resulting in an overall desirability of zero. Moving away from this central zone, the desirability gradually increases, forming green and yellow bands that represent acceptable to good conditions. The highest desirability values, such as 0.671, occur near the right edge of the plot when the voltage is higher (B ≈ 20.8–21.0 V), combined with either lower speeds (C ≈ 3.33–3.46 mm/s) or higher speeds (C ≈ 3.72–3.85 mm/s). This indicates that voltage has a stronger positive influence on desirability, while speed shows a U-shaped effect where the extremes are more favorable than the

midrange. Practically, the central region should be avoided since even small variations in parameters here result in failure, while the right-hand edge bands provide more robust and reliable operating windows. This pattern highlights that process optimization should focus on higher voltage levels with carefully selected speed values away from the central range to ensure better overall desirability.

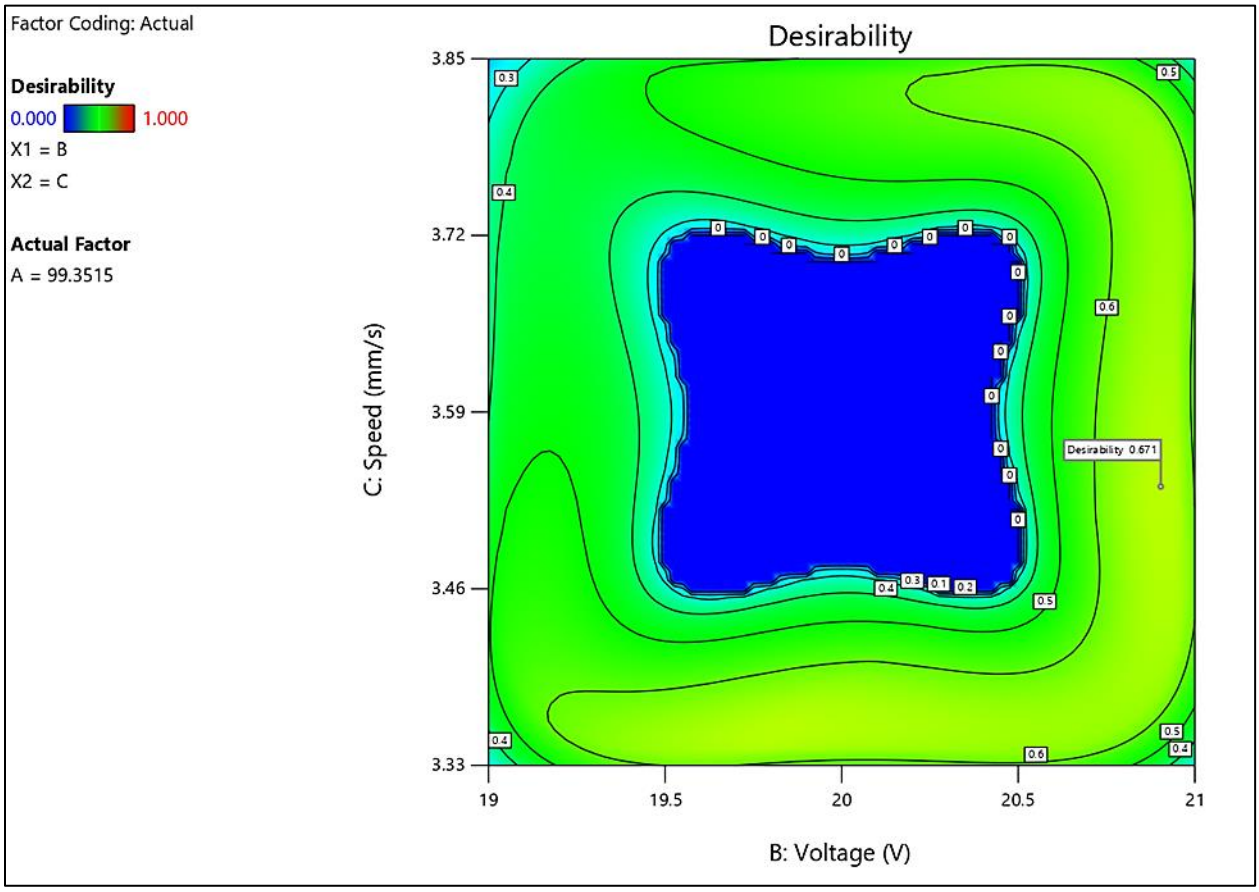

Fig.4. 35 Optimal process window and practical implications

4.9 Verification of the results

To verify the predictive capability of the desirability function analysis (DFA)–based optimization, confirmation experiments were conducted using five welded samples fabricated under the optimal MIG welding parameters identified by the RSM–DFA model, as shown in Table 4. 8. The optimized process conditions consisted of a welding current of 99.35 A, welding voltage of 20.90 V, and welding speed of 3.54 mm/s, which were applied uniformly to all confirmation samples. Fig.4. 36 presents the physical appearance of the specimens prepared for verification tests at different stages of sample preparation. Fig.4. 36 (a) shows the as-welded rectangular samples

before surface polishing, while Fig.4. 36 (b) illustrates the as-welded tensile test specimens before polishing. Fig.4. 36 (c) and Fig.4. 36 (d) display the corresponding polished rectangular hardness specimens and polished tensile specimens, respectively, prepared according to standard testing requirements. These samples were used for hardness and tensile testing to validate the DFA-predicted responses. At the optimal welding conditions, the DFA predicted a yield strength of 403.51 MPa, ultimate tensile strength (UTS) of 499.71 MPa, strain at fracture of 22.47%, weld zone (WZ) hardness of 92.41 HV, and heat-affected zone (HAZ) hardness of 86.75 HV. The associated standard errors were minimal, indicating a high level of confidence in the predictive accuracy of the developed RSM–DFA model. The experimentally obtained results from the five confirmation samples yielded average values of 399.98 MPa yield strength, 494.22 MPa UTS, 22.24% strain at fracture, 91.46 HV hardness at the WZ, and 85.90 HV hardness at the HAZ. The percentage deviation between the predicted and experimental responses was found to be low, with average errors of 1.25% for yield strength, 1.29% for UTS, 1.29% for strain at fracture, 1.46% for WZ hardness, and 1.19% for HAZ hardness, all of which fall within acceptable experimental limits (±2%) for MIG welding processes. These small deviations can be attributed to inherent process variability, including minor fluctuations in arc stability, heat input, and measurement uncertainty during tensile and hardness testing. Despite these variations, the experimental responses closely followed the predicted trends, thereby confirming the robustness and reliability of the developed RSM–DFA optimization framework. The experimental verification results closely matched the predicted values obtained from the Response Surface Methodology and desirability-based optimization. This strong agreement confirms the adequacy, robustness, and predictive accuracy of the developed regression models for estimating mechanical performance of MIG-welded mild steel joints. Despite this strong validation, certain practical limitations should be acknowledged. The experiments were conducted under controlled laboratory conditions using flat-position welding and uniform plate thicknesses, whereas industrial welding environments often involve positional welding, variable joint fit-up, surface contamination, and fluctuating ambient conditions. These factors may introduce additional variability in heat input and weld pool stability, potentially affecting mechanical outcomes. Furthermore, the study focused on a limited parameter range of current, voltage, and travel speed; extrapolation beyond this domain may require additional experimental validation.

Nevertheless, the optimized parameter window identified in this study provides a robust and practically applicable guideline for improving weld quality, minimizing defect formation, and enhancing mechanical reliability in real-world fabrication environments. Future studies may extend this framework to thicker sections, multi-pass welding, positional welding, and other alloy systems to further broaden industrial applicability. Thus, the verification results demonstrate that the DFA-selected optimal welding parameters provide a well-balanced and practically achievable combination of strength, ductility, and hardness distribution. This confirms the suitability of the optimized solution for practical MIG welding applications, where controlled trade-offs among competing mechanical properties are essential for achieving high-quality and reliable welds.

Table 4. 8: Confirmation test results comparing DFA-predicted and experimental mechanical properties at optimal MIG welding parameters

Sample	**Yield Strength (MPa)**	**Error (%)**	**UTS (MPa)**	**Error (%)**	**Strain at Fracture (%)**	**Error (%)**	**WZ Hardness (HV)**	**Error (%)**	**HAZ Hardness (HV)**	**Error (%)**
Predicted (DFA)	**403.51**	–	**499.71**	–	**22.47**	–	**92.41**	–	**86.75**	–
Sample 1	396.8	1.66	491.2	1.70	22.05	1.87	90.9	1.63	85.4	1.56
Sample 2	401.5	0.50	496.3	0.68	22.21	1.16	91.8	0.66	86.1	0.75
Sample 3	398.9	1.15	488.7	2.20	21.98	2.18	90.2	2.39	84.9	2.13
Sample 4	407.3	0.94	502.1	0.48	22.62	0.67	93.4	1.07	87.2	0.52
Sample 5	395.4	2.01	492.8	1.38	22.34	0.58	91.0	1.53	85.9	0.98
Average	**399.98**	**1.25**	**494.22**	**1.29**	**22.24**	**1.29**	**91.46**	**1.46**	**85.90**	**1.19**

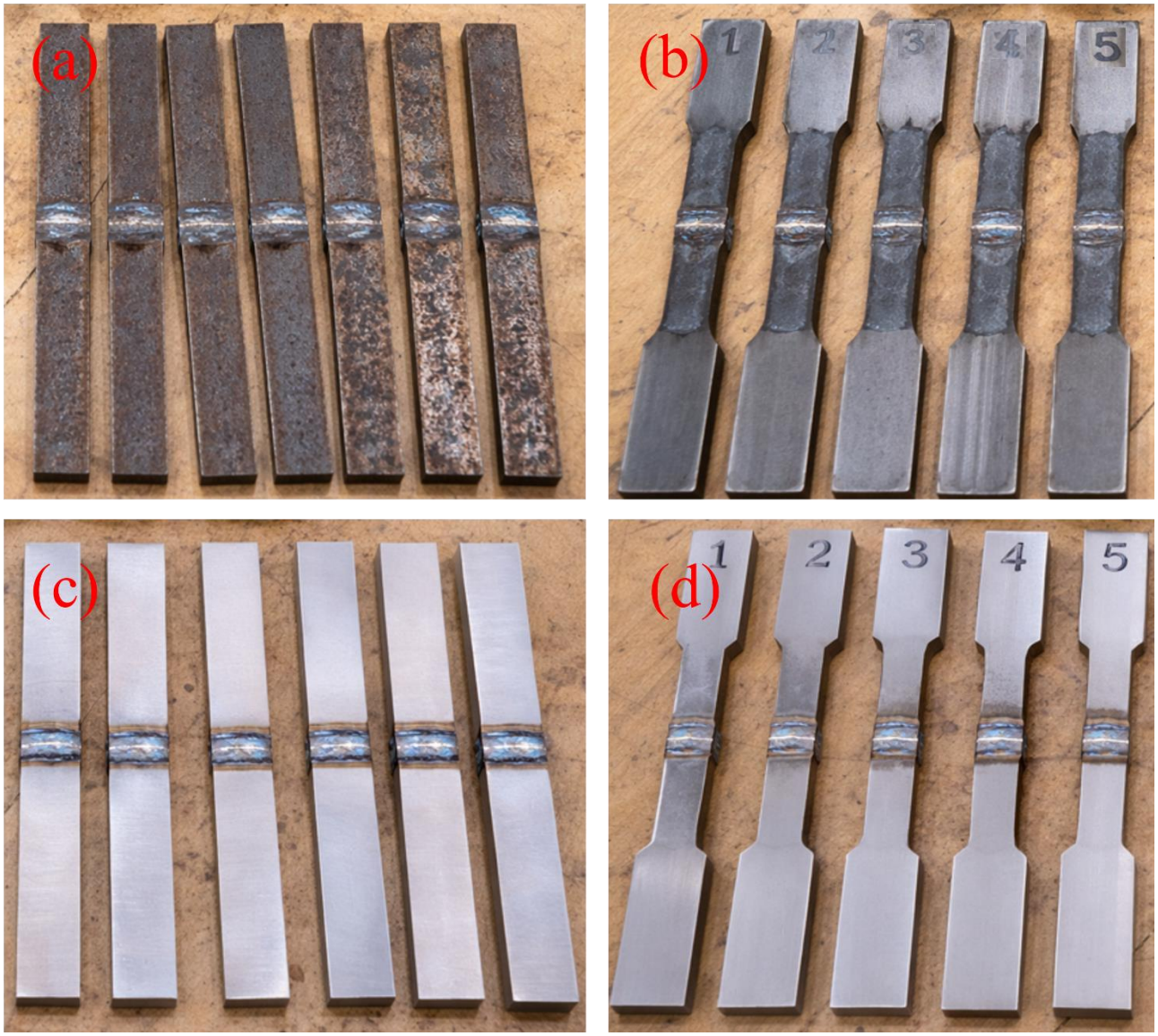

Fig.4. 36 Sample prepared for the verification: a) As-welded specimens (before surface finishing), (b) Machined tensile specimens (rough/initial machining stage), (c) Ground and polished welded specimens, (d) Final tensile test specimens (finished and numbered)

CHAPTER FIVE

CONCLUSION AND RECOMMENDATIONS

5.1 Conclusion

This study investigated and optimized Metal Inert Gas (MIG) welding parameters to enhance the mechanical performance and structural integrity of low-carbon steel welded joints using Response Surface Methodology (RSM) and Desirability Function Analysis (DFA). The integrated approach combining non-destructive testing (liquid penetrant testing, magnetic particle testing, and ultrasonic testing), destructive mechanical testing (tensile and hardness testing), and statistical optimization enabled systematic identification of defect mechanisms and performance improvement pathways.

Quantitative analysis demonstrated that optimized welding parameters significantly improved mechanical properties compared to the failed (old) welded joints. The ultimate tensile strength (UTS) increased by approximately 36%, from an average of ~360 MPa in failed joints to ~490 MPa in optimized joints. Similarly, yield strength improved by approximately 38%, increasing from ~290 MPa to ~400 MPa, while strain at fracture increased by nearly 95%, rising from ~11% to ~21–22%, indicating a substantial enhancement in ductility and energy absorption capacity. Hardness values also showed improvement and homogenization, with weld zone hardness increasing by approximately 14% and HAZ hardness by approximately 10%, reflecting improved microstructural refinement and thermal control.

Non-destructive testing results confirmed that optimized welds exhibited significantly reduced defect density, with average surface crack lengths decreasing from ~12 mm to <4 mm, porosity cluster sizes reducing from ~6–7 mm to <2 mm, and ultrasonic echo attenuation diminishing markedly, indicating improved metallurgical continuity and internal integrity. These improvements translated directly into enhanced tensile performance and more stable ductile fracture behavior, as evidenced by smoother stress–strain curves and delayed fracture initiation in optimized specimens.

Statistical analysis revealed that welding current was the most influential parameter affecting strength and hardness responses, while welding speed predominantly governed ductility. Voltage exhibited secondary but significant interaction effects, particularly in conjunction with current and travel speed. The developed quadratic regression models exhibited strong predictive capability,

with experimental verification errors below ±2%, confirming the robustness and reliability of the optimization framework.

Thus, the study demonstrates that systematic parameter optimization using RSM-DFA can substantially improve weld quality, mechanical reliability, and structural safety in MIG-welded mild steel joints. The findings provide validated quantitative evidence that defect minimization and microstructural refinement achieved through optimized heat input control lead directly to superior mechanical performance and long-term service reliability.

5.2 Recommendations

5.2.1 Recommendations for Industry and Practice

Based on the outcomes of this research, it is recommended that fabrication industries adopting MIG welding for structural steel applications implement the optimized parameter window identified in this study to improve weld quality and service reliability. The demonstrated increases of over 35% in strength and nearly 100% in ductility**,** combined with reduced defect frequency and improved ultrasonic signal integrity, indicate that the proposed welding conditions are well-suited for load-bearing structures such as stair joints, frames, bridges, and support assemblies. These improvements can reduce repair frequency, extend service life, and enhance safety margins in industrial applications.

In addition, integrating non-destructive testing methods such as ultrasonic testing and magnetic particle inspection into routine quality control procedures is strongly recommended to ensure early detection of defects and to maintain consistency in weld performance under production environments.

5.2.2 Future Research Recommendations

1. **Machine learning and predictive modeling:**
   Advanced data-driven tools such as Artificial Neural Networks (ANNs)**,** Random Forest regression**,** and Support Vector Machines (SVMs) could be employed to predict weld defect formation and mechanical performance based on process parameters. Software platforms such as MATLAB**,** Python (TensorFlow, Scikit-learn)**,** and ANSYS Welding Simulation modules could be integrated with experimental datasets to enable real-time adaptive welding control and intelligent defect prevention.
2. **Cost–benefit and productivity analysis:**
   Future studies should include a comprehensive cost–benefit analysis comparing optimized and non-optimized welding conditions. This may quantify reductions in rework, scrap rate, inspection time, and maintenance costs against marginal increases in energy consumption or consumable usage, thereby establishing the economic feasibility and industrial scalability of optimized MIG welding parameters.
3. **Expanded process domains and joint configurations:**
   Further investigations could extend the optimization framework to multi-pass welding,

positional welding, thicker plates, and alternative joint geometries, as well as to other alloys such as stainless steels and aluminum alloys, to broaden the applicability of the findings.

4. **In-service performance and fatigue life evaluation:**

   Long-term fatigue testing, corrosion-fatigue interaction studies, and fracture mechanics-based assessments under service loading conditions would provide additional validation of the durability and reliability of optimized welds in real industrial environments.

References

Alifian, F., Setiawan, E. A., & Rosidah, A. A. (2025). Swing and Electrode Diameter Effects on Toughness and Hardness of Stainless Steel 304 MIG Welding Results. *Jurnal IPTEK*, *28*(2), 85–90. https://doi.org/10.31284/j.iptek.2024.v28i2.5375

Arandjelovic, M., Djordjevic, B., Sedmak, S., Radu, D., Petrovic, A., Dikic, S., & Sedmak, A. (2024). Failure analysis of welded joint with multiple defects by extended Finite Element Method and Engineering Critical Analysis. *Engineering Failure Analysis*, *160*. https://doi.org/10.1016/j.engfailanal.2024.108176

Behredin, K. B., Ramulu, P. J., Habtamu, B., Besufekad, N., & Tesfaye, N. (2022). Characterization and Parametric Optimization of EN-10149-2 Steel Welded Joints Made by MIG Welding. *Advances in Materials Science and Engineering*, *2022*. https://doi.org/10.1155/2022/8276496

Demiral, M., & Kadioglu, F. (2023). Damage Characteristics of a Step Lap Joint Exposed to Flexural Loading for Its Different Configurations. *Polymers*, *15*(11). https://doi.org/10.3390/polym15112458

Demiral, M., & Mamedov, A. (2025). Comparison of the strength of resistance spot-welded, bonded, and hybrid single lap joints: A numerical investigation. *Results in Engineering*, *25*. https://doi.org/10.1016/j.rineng.2024.103871

Di, S., Yang, X., Luan, G., & Jian, B. (2006). Comparative study on fatigue properties between AA2024-T4 friction stir welds and base materials. *Materials Science and Engineering: A*, *435–436*, 389–395. https://doi.org/10.1016/j.msea.2006.07.009

Falodun, O., Oke, S., & Bodunrin, M. (2025). A comprehensive review of residual stresses in carbon steel welding: formation mechanisms, mitigation strategies, and advanced post-weld heat treatment techniques. *International Journal of Advanced Manufacturing Technology*, *136*(10), 4107–4140. https://doi.org/10.1007/s00170-025-15088-8

Frih, I., Montay, G., & Adragna, P. A. (2017). Microstructure, Hardness, and Residual Stress Distributions in T-Joint Weld of HSLA S500MC Steel. *Metallurgical and Materials Transactions A: Physical Metallurgy and Materials Science*, *48*(3), 1103–1110.

https://doi.org/10.1007/s11661-016-3932-6

Gaidhane, V. K., & Kolhe, S. R. (2024). A Review on Advances in Computer Aided Weld Defects Detection. *1st International Conference on Electronics, Computing, Communication and Control Technology, ICECCC 2024*. https://doi.org/10.1109/ICECCC61767.2024.10593858

García-Gómez, M., Curiel-López, F. F., Taha-Tijerina, J. J., López-Morelos, V. H., Verduzco-Juárez, J. C., & García-Ochoa, C. A. (2024). Reduction in Porosity in GMAW-P Welds of CP780 Galvanized Steel with ER70S-3 Electrode Using the Taguchi Methodology. *Metals*, *14*(8). https://doi.org/10.3390/met14080857

Guizani, H., Ben Nasser, M., Tlili, B., Oueslati, A., & Chafra, M. (2019). Finishing and quality of mechanically brushed 316L stainless steel welded joints using MIG process: hardness modeling by L9 TAGUCHI design. *International Journal of Advanced Manufacturing Technology*, *105*(1–4), 1009–1022. https://doi.org/10.1007/s00170-019-04249-1

Haque, S. R. (2023). Investigation on welding defects of alloys using TIG and MIG welding. *Hybrid Advances*, *3*. https://doi.org/10.1016/j.hybadv.2023.100066

Hobbacher, A. F. (2019). *Erratum to: Recommendations for Fatigue Design of Welded Joints and Components*. E3–E3. https://doi.org/10.1007/978-3-319-23757-2_8

Holmstrand, T., Mrdjanov, N., Barsoum, Z., & Åstrand, E. (2014). Fatigue life assessment of improved joints welded with alternative welding techniques. *Engineering Failure Analysis*, *42*, 10–21. https://doi.org/10.1016/j.engfailanal.2014.03.012

Jatavallabhula, J. K., Masubelele, F., Chikumba, S., & Veeredhi, V. R. (2025). Artificial intelligence for quality assurance in friction stir welding - a review on opportunities and challenges. *Engineering Research Express*, *7*(2). https://doi.org/10.1088/2631-8695/adc877

Jerbi, A., Souissi, S., & Trabelsi, E. (2024). Optimization of the Parameters of Robotized TIG Welding of an Aluminum Alloy. *Mechanisms and Machine Science*, *144*, 259–267. https://doi.org/10.1007/978-3-031-42659-9_29

Kalácska, E., Májlinger, K., Fábián, E. R., & Pasquale, R. S. (2017). MIG-welding of dissimilar

advanced high strength steel sheets. *Materials Science Forum*, *885*, 80–85. https://doi.org/10.4028/www.scientific.net/MSF.885.80

Kalita, K., Ghadai, R. K., Čep, R., & Jangir, P. (2024). Enhancing Welding Quality Through Predictive Modelling — Insights From Machine Learning Techniques. *MM Science Journal*, *2024-Decem*, 7897–7902. https://doi.org/10.17973/MMSJ.2024_12_2024124

Khdir, Y. K., Kako, S. A., & Gardi, R. H. (2020). Study of Welding Dissimilar Metals – Low-carbon Steel AISI 1018 and Austenitic Stainless Steel AISI 304. *Polytechnic Journal*, *10*(1), 1–5. https://doi.org/10.25156/ptj.v10n1y2020.pp1-5

Kumar, R., Ghosh, B., Nigam, R., Mukherjee, A., & Das, S. (2023). Optimization of Process Parameters of Gas Metal Arc Welding using Taguchi Method. *Journal of Mines, Metals and Fuels*, *71*(12), 6–14. https://doi.org/10.18311/jmmf/2023/43787

Laukhin, D., Pozniakov, V., Beketov, O., Rott, N., & Shchudro, A. (2020). Analysis of the effects of welding conditions on the formation of the structure of welded joints of low-carbon low-alloy steels. *Key Engineering Materials*, *844*, 146–154. https://doi.org/10.4028/www.scientific.net/KEM.844.146

Lei, Z., Cao, H., Cui, X., Wen, Z., Li, L., & Zhang, Q. (2024). Study on the suppression of solidification cracks in narrow gap laser welding of high-strength steel based on dual-beam gradient control weld solidification. *Journal of Materials Processing Technology*, *329*. https://doi.org/10.1016/j.jmatprotec.2024.118440

Lewandowski, J., Rozumek, D., & Hepner, M. (2018). Test of fatigue crack growth in welded specimens subjected to bending. *Bulletin of the Military University of Technology*, *67*(1), 185–196. https://doi.org/10.5604/01.3001.0011.8061

Madhvacharyula, A. S., Pavan, A. V. S., Gorthi, S., Chitral, S., Venkaiah, N., & Kiran, D. V. (2022). In situ detection of welding defects: a review. *Welding in the World*, *66*(4), 611–628. https://doi.org/10.1007/s40194-021-01229-6

Mekonone, S. T., Gemechu, T. G., Mekonnen, T. H., & Momhur, A. M. (2025). Optimization, thermo-mechanical loading effects and microstructure evolutions of Metal Inert Gas (MIG)

welded 304L stainless steel. *Materials Today Communications*, *42*. https://doi.org/10.1016/j.mtcomm.2025.111514

Mushthofa, M., Pratama Nurfauzi, F., & Hardawati, A. (2023). Investigation of Effective Section Reduction in Low Carbon Steel during SMAW Welding. *Teknisia*, *28*(2), 79–89. https://doi.org/10.20885/teknisia.vol28.iss2.art2

Odermatt, A. E., Ventzke, V., Dorn, F., Dinsé, R., Merhof, P., & Kashaev, N. (2021). Effect of laser beam welding on microstructure, tensile strength and fatigue behaviour of duplex stainless steel 2205. *Journal of Manufacturing Processes*, *72*, 148–158. https://doi.org/10.1016/j.jmapro.2021.10.020

Orlando, M., De Maddis, M., Razza, V., & Lunetto, V. (2024). Non-destructive detection and analysis of weld defects in dissimilar pulsed GMAW and FSW joints of aluminium castings and plates through 3D X-ray computed tomography. *International Journal of Advanced Manufacturing Technology*, *132*(5–6), 2957–2970. https://doi.org/10.1007/s00170-024-13576-x

Pereira, A. B., & Fernandes, F. A. O. (2023). Non-destructive material testing in welding: ultrasonic scanning. *Non-Destructive Material Characterization Methods*, 281–293. https://doi.org/10.1016/B978-0-323-91150-4.00020-3

Purwaningrum, Y., Triyono, Wirawan PU, M., & Alfarizi, F. (2016). Effect of shielding gas mixture on gas metal arc welding (GMAW) of low carbon steel (LR Grade A). *Key Engineering Materials*, *705*, 250–254. https://doi.org/10.4028/www.scientific.net/KEM.705.250

Ren, X. (2022). Research on main defects and prevention measures of metal material welding based on ultrasonic nondestructive testing technology. *Journal of Physics: Conference Series*, *2321*(1). https://doi.org/10.1088/1742-6596/2321/1/012023

Saha, S., Shahjahan, N. B., & Ahmed, N. (2015). Effect of Process Parameters on Hardness, Depth of Heat Affected Zone and Micro Structure of Weldment in Mig Welding. *Journal of Mechanical Engineering*, *44*(2), 132–136. https://doi.org/10.3329/jme.v44i2.21438

Said, J. M., Turan, F. M., & Sazali, N. (2023). Integrated Assessment of MIG Welding Parameters on Carbon Steel using RSM Optimisation. *Journal of Advanced Research in Applied Mechanics*, *111*(1), 16–29. https://doi.org/10.37934/aram.111.1.1629

SaThierbach, K., Petrovic, S., Schilbach, S., Mayo, D. J., Perriches, T., Rundlet, E. J. E. J. E. J., Jeon, Y. E., Collins, L. N. L. N., Huber, F. M. F. M., Lin, D. D. H. D. H., Paduch, M., Koide, A., Lu, V. T., Fischer, J., Hurt, E., Koide, S., Kossiakoff, A. A., Hoelz, A., Hawryluk-gara, L. A., … Hoelz, A. (2015). No 主観的健康感を中心とした在宅高齢者における 健康関連指標に関する共分散構造分析Title. *Proceedings of the National Academy of Sciences*, *3*(1), 1–15. https://doi.org/Digital Twin Development for Additive Manufacturing

Shravan, C., Radhika, N., Deepak Kumar, N. H., & Sivasailam, B. (2024). A review on welding techniques: properties, characterisations and engineering applications. *Advances in Materials and Processing Technologies*, *10*(2), 1126–1181. https://doi.org/10.1080/2374068X.2023.2186638

Sonsino, C. M. (2009). Effect of residual stresses on the fatigue behaviour of welded joints depending on loading conditions and weld geometry. *International Journal of Fatigue*, *31*(1), 88–101. https://doi.org/10.1016/j.ijfatigue.2008.02.015

Sood, S., Mishra, P., Pandit, M., & Khanna, P. (2022). Prediction and Optimization of Weld Bead Geometry of MIG Welded Stainless Steel 202 Plates. *Lecture Notes in Mechanical Engineering*, 723–734. https://doi.org/10.1007/978-981-16-2794-1_64

Steimbreger, C., Gubeljak, N., Enzinger, N., Ernst, W., & Chapetti, M. (2018). Influence of static strength on the fatigue resistance of welds. *MATEC Web of Conferences*, *165*. https://doi.org/10.1051/matecconf/201816513010

Sudarno, S., Do, Q. T., Nubli, H., Prabowoputra, D. M., Agusti, N. C. D., Ridwan, R., & Vandika, A. (2023). Evaluating the Influence of Environmental Factors and Parameters on Advancements in Welding and Joining Processes: A Review. *Mekanika: Majalah Ilmiah Mekanika*, *22*(2), 88. https://doi.org/10.20961/mekanika.v22i2.75378

Suleimanov, R. I., Zainagalina, L. Z., Khabibullin, M. Y., Zaripova, L. M., & Kovalev, N. O. (2018). Studying heat-affected zone deformations of electric arc welding. *IOP Conference Series: Materials Science and Engineering*, *327*(3). https://doi.org/10.1088/1757-899X/327/3/032053

Szusta, J., Derpeński, Ł., Karakaş, Ö., Tüzün, N., & Dobrzański, S. (2023). Effect of Welding Process Parameters on the Strength of Dissimilar Joints of S355 and Strenx 700 Steels Used in the Manufacture of Agricultural Machinery. *Materials*, *16*(21). https://doi.org/10.3390/ma16216963

Tan, Z., Yu, K., Zeng, C., Cai, X., Wang, Z., Wang, H., Yang, M., Qi, B., & Cong, B. (2024). Porosity suppression and mechanical property improvement of wire-arc directed energy deposited TiCp/Al-Cu alloys joint by oscillating pulsed wave laser beam welding. *Journal of Materials Processing Technology*, *329*. https://doi.org/10.1016/j.jmatprotec.2024.118458

Thompson, T., Liu, J., & Hu, C. (2023). A comparative analysis of step loading and staircase testing for fatigue strength estimation of an engine component. *Fatigue and Fracture of Engineering Materials and Structures*, *46*(2), 667–681. https://doi.org/10.1111/ffe.13898

Venkatratnam, D., & Kesava Rao, V. V. S. (2020). Effect of MIG welding parameters on mechanical properties of dissimilar weld joints of AISI 202 and AISI 316 steels. *Int J of Advanced Design and Manufacturing Technology*, *13*(2), 51–64.

Wang, Z., Xue, H., Zhang, Y. B., Wang, R. X., & Geng, M. (2024). Characterization of Mechanical Heterogeneity and Study of the Mechanical Field at the Tip of the Stationary-Growing Crack in Dissimilar Metal Welded Joints. *Journal of Engineering Materials and Technology*, *146*(4). https://doi.org/10.1115/1.4065096

Widiatmika, K. P. (2015). No 主観的健康感を中心とした在宅高齢者における 健康関連指標に関する共分散構造分析Title. *Etika Jurnalisme Pada Koran Kuning : Sebuah Studi Mengenai Koran Lampu Hijau*, *16*(2), 39–55. https://doi.org/https://doi.org/10.26153/TSW/7149

Xu, X., Xie, L., Zhou, S., An, J., Huang, Y., Liu, Y., & Jin, L. (2023). Effect of Welding Defects

on Fatigue Properties of SWA490BW Steel Cruciform Welded Joints. *Materials*, *16*(13). https://doi.org/10.3390/ma16134751

Yu, B., Chen, Z., Wang, P., & Song, X. (2023). A comparative study on the mechanical behavior of S355J2 steel repair-welded joints. *Journal of Constructional Steel Research*, *205*. https://doi.org/10.1016/j.jcsr.2023.107878

Zhang, B., Sun, K., Zhou, H., Zhang, C., & Gao, D. (2024). Extraction, modeling and impact analysis of porosity defects formed in the CFRTP/Al6061 laser direct joining process. *Polymer Composites*, *45*(11), 10527–10541. https://doi.org/10.1002/pc.28492

Zhang, G., & Xu, J. (2024). Finite Element Analysis of Six-axis Manipulator Based on Solidworks and ANSYS. *Proceedings - 2024 International Conference on Intelligent Computing and Robotics, ICICR 2024*, 220–225. https://doi.org/10.1109/ICICR61203.2024.00047

Zong, L., Fang, W., Huang, C., Wang, Z., & Gardner, L. (2023). Low cycle fatigue behaviour of wire arc additively manufactured ER70S-6 steel. *International Journal of Fatigue*, *176*. https://doi.org/10.1016/j.ijfatigue.2023.107910

Appendixes

A: Composition (spectroscopy results)

This appendix presents the detailed spectroscopic characterization results used to determine the chemical composition and alloying element distribution of the base metal and weld metal. These data support the metallurgical interpretation of mechanical behavior and microstructural evolution discussed in Chapters 3 and 4.

Fig.A. 1 presents the spectrometric analysis results of the tested material sample identified as a welded joint steel specimen. The analysis, conducted by the Ethiopia Conformity Assessment Enterprise (ECAE), reveals that the primary constituent element of the sample is iron (Fe), accounting for approximately 99.33–99.39% of the total composition. The remaining elements occur in minor proportions, confirming that the material is a typical low-carbon steel. The carbon (C) content of about 0.065% indicates a mild steel with good ductility and excellent weldability, characteristics that minimize the risk of cracking in the heat-affected zone during welding operations. Manganese (Mn), present at around 0.35%, serves as a strengthening element and helps to improve the toughness of the steel, while the small amount of silicon (Si) recorded at 0.015% contributes to deoxidation during steelmaking. Phosphorus (P) and sulfur (S) contents, measured at 0.006% and 0.017% respectively, are within acceptable limits for structural and welded applications. Their low concentrations are desirable since excessive amounts can cause brittleness and hot shortness in welded joints. The traces of alloying elements such as chromium (Cr), nickel (Ni), molybdenum (Mo), and copper (Cu) are negligible, confirming that the specimen is not an alloyed steel grade but rather an unalloyed carbon steel suitable for general fabrication. Aluminum (Al) content of 0.051% further supports its role as a deoxidizing agent used during the steel refining process. Overall, the chemical composition obtained through spectrometric evaluation verifies that the material corresponds to standard mild steel used for structural and fabrication purposes. The low carbon and impurity levels ensure good weldability, adequate mechanical strength, and ease of forming, making it well-suited for applications that do not demand high corrosion or heat resistance. However, due to the absence of significant chromium and nickel content, the corrosion resistance of the material remains limited, and protective coatings are recommended when used in outdoor or humid environments. Thus, the spectroscopic results presented in Fig. A1 confirm that the analyzed welding joint sample possesses the typical compositional characteristics and

metallurgical suitability expected of mild steel employed in general engineering and construction applications.

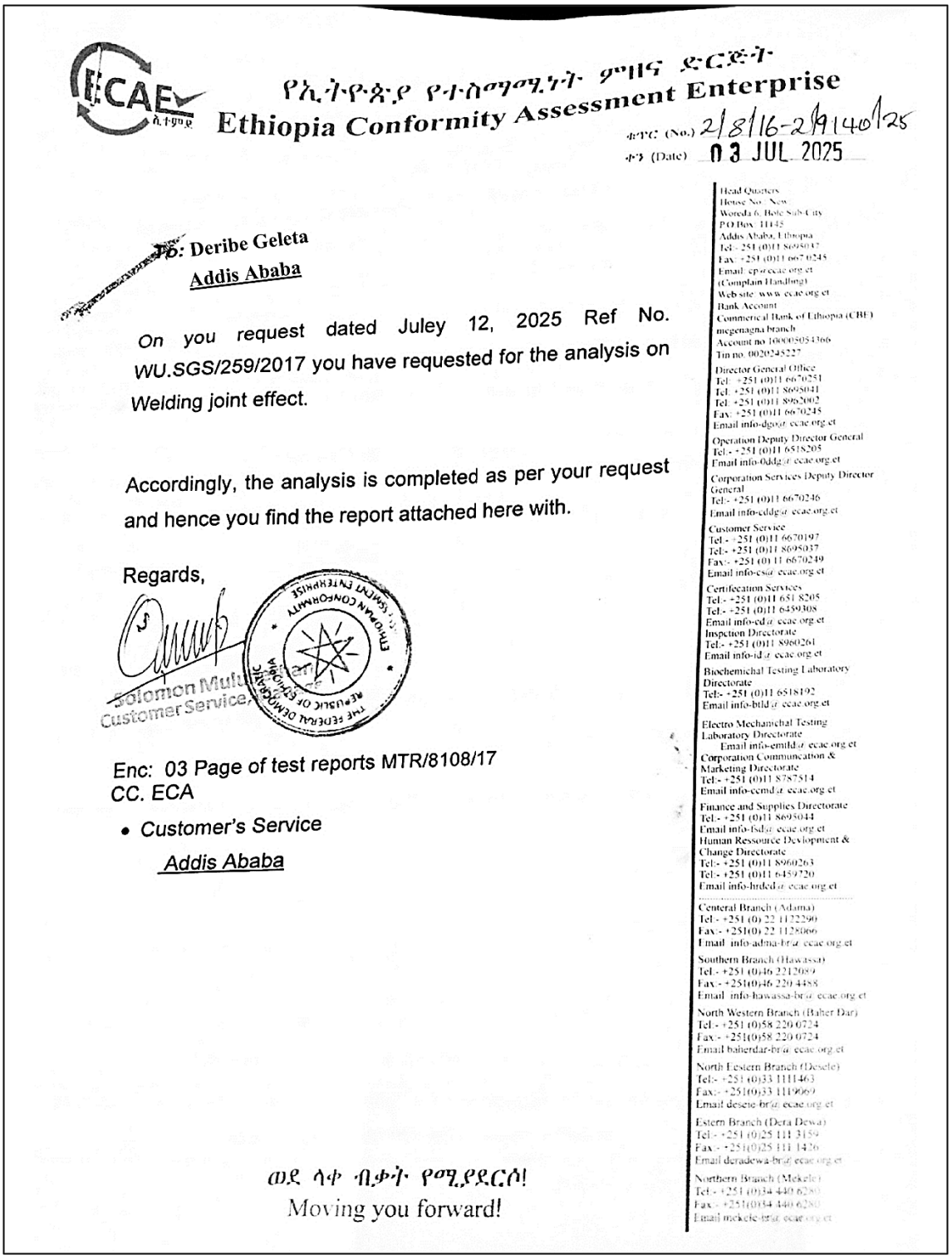

የኢትዮጵያ የተስማሚነት ምዘና ድርጅት
Ethiopia Conformity Assessment Enterprise

ቁጥር (No.) 2/8116-2/9140/25
ቀን (Date) 03 JUL 2025

To: Deribe Geleta
Addis Ababa

On you request dated Juley 12, 2025 Ref No. WU.SGS/259/2017 you have requested for the analysis on Welding joint effect.

Accordingly, the analysis is completed as per your request and hence you find the report attached here with.

Regards,

Solomon Mufu
Customer Service

Enc: 03 Page of test reports MTR/8108/17
CC. ECA
- Customer's Service
  Addis Ababa

ወደ ላቀ ብቃት የሚያደርሰ!
Moving you forward!

Head Quarters
House No. New
Woreda 6, Bole Sub City
P.O.Box: 11145
Addis Ababa, Ethiopia
Tel:- +251 (0)11 8695037
Fax: +251 (0)11 667 0245
Email: cp@ecae.org.et
(Complain Handling)
Web site: www.ecae.org.et
Bank Account
Commerical Bank of Ethiopia (CBE)
megenagna branch
Account no 1000035043366
Tin no. 0020245227

Director General Office
Tel: +251 (0)11 6670251
Tel: +251 (0)11 8695041
Tel. +251 (0)11 8962002
Fax: +251 (0)11 6670245
Email info-dgo@ ecae.org.et

Operation Deputy Director General
Tel:- +251 (0)11 6518205
Email info-oddg@ ecae.org.et

Corporation Services Deputy Director General
Tel:- +251 (0)11 6670246
Email info-cddg@ ecae.org.et

Customer Service
Tel - +251 (0)11 6670197
Tel:- +251 (0)11 8695037
Fax:- +251 (0) 11 6670249
Email info-cs@ ecae.org.et

Certifecation Services
Tel:- +251 (0)11 651 8205
Tel:- +251 (0)11 6459308
Email info-cd@ ecae.org.et
Inspction Directorate
Tel:- +251 (0)11 8960261
Email info-id@ ecae.org.et

Biochemichal Testing Laboratory Directorate
Tel:- +251 (0)11 6518192
Email info-btld@ ecae.org.et

Electro Mechanichal Testing Laboratory Directorate
Email info-emtld@ ecae.org.et
Corporation Communication & Marketing Directorate
Tel:- +251 (0)11 8787514
Email info-ccmd@ ecae.org.et

Finance and Supplies Directorate
Tel:- +251 (0)11 8695044
Email info-fsd@ ecae.org.et
Human Ressource Development & Change Directorate
Tel:- +251 (0)11 8960263
Tel:- +251 (0)11 6459720
Email info-hrded@ ecae.org.et

Centeral Branch (Adama)
Tel:- +251 (0) 22 1122290
Fax:- +251(0) 22 1128066
Email info-adma-br@ ecae.org.et

Southern Branch (Hawassa)
Tel:- +251 (0)46 2212089
Fax:- +251(0)46 220 4488
Email info-hawassa-br@ ecae.org.et

North Western Branch (Bahir Dar)
Tel:- +251 (0)58 220 0724
Fax:- +251(0)58 220 0724
Email bahirdar-br@ ecae.org.et

North Eastern Branch (Desele)
Tel:- +251 (0)33 1111463
Fax:- +251(0)33 1119069
Email desele-br@ ecae.org.et

Estern Branch (Dera Dewa)
Tel:- +251 (0)25 111 3159
Fax:- +251(0)25 111 1426
Email deradewa-br@ ecae.org.et

Northern Branch (Mekele)
Tel:- +251 (0)34 440 6280
Fax:- +251(0)34 440 6280
Email mekele-br@ ecae.org.et

የኢትዮጵያ የተስማሚነት ምዘና ድርጅት

Ethiopian Conformity Assessment Enterprise

Document No.	
ECAE/F/QR/1	
Copy No.	Page No.
-	3
Page No.	Effective Date
1 of 3	25 Oct 22

Title:

TEST REPORT
የፍተሻ ሪፖርት

Name and address of client:	Deribe Geleta, Addis Ababa	Test Report No:	MTR/8108/17
Tel:	+251-912642474	Test Order No:	WU.SGS/259/2017
Fax:	--	Reported date:	30/06/2025
E-mail:	--	Date of sampling	Not specified
Date sample Received:	27/06/2025	Place of sampling	Not specified
Client Sample code: (brand)	--	Sampled and submitted by	Client
Type of sample:	Welding Joint effect	Date tested:	27/06/2025
Laboratory Designation Number: 17290056		Method Specification -	

S/N	Characteristics tested	Test Method/ Specification	Standard Requirements			Test result	Comment
			Min	Nom	Min		
1.	Chemical Composition (%)	Spectrometric / -	-	-	-	Two - pages chemical composition result is attached at the back of this test report	-

Remark

1 This test report relates only to the specific sample product which has been tested by ECAE testing laboratory.

Test report authorized by, Name Liyew Wudie , Position Analyst IV, Sign. for

ARCHIVES

ISO/IEC 17025:2017 Accredited Testing Laboratory

✉ 11145 ☎ 011 6 51-64-68, Fax. 011 6 45-97-20, E-mail info-cs@eca-e.com Web site: www.eca-e.com

BOLE SUBCITY, WOREDA 6, ADDIS ABABA, ETHIOPIA

SPECTRO

Sample Results

Sample Result Name	Type	Measure Date Time	Recalculation Date Time	Origin
17290056	Unknown	27/06/2025 16:17	27/06/2025 16:19	Measured

Method Name	Check Type	Check Status	Correction Type	Outlier Test Type
Fe-10-M	None	Not Used	None	None

Status
Not Used

Sample Name	Grade ID
17290056	

	C Conc %	Si Conc %	Mn Conc %	P Conc %	S Conc %	Cr Conc %	Mo Conc %	Ni Conc %	Al Conc %	Co Conc %	Cu Conc %	Nb Conc %	Ti Conc %
1	0.054	0.013	0.36	0.006	0.017	0.007	0.009	0.048	0.051	0.028	0.011	<0.0010	<0.0002
2	0.061	0.016	0.37	0.005	0.017	0.007	0.011	0.047	0.053	0.029	0.011	<0.0010	<0.0002
3	0.053	0.015	0.36	0.006	0.015	0.007	0.012	0.049	0.053	0.028	0.012	<0.0010	<0.0002
Rep	*0.056*	*0.014*	*0.37*	*0.006*	*0.016*	*0.007*	*0.010*	*0.048*	*0.052*	*0.029*	*0.011*	<0.0010	<0.0002
SD	*0.005*	*0.001*	*0.006*	*0.0002*	*0.001*	*0.0001*	*0.002*	*0.0007*	*0.0009*	*0.0002*	*0.0003*	*0.0000*	*0.0000*
RSD	*8.14*	*7.95*	*1.58*	*3.09*	*7.32*	*1.58*	*15.55*	*1.47*	*1.80*	*0.79*	*2.72*	*0.0000*	*0.0000*

	V Conc %	W Conc %	Pb Conc %	Sn Conc %	As Conc %	Zr Conc %	Bi Conc %	Ca Conc %	Ce Conc %	Sb Conc %	Se Conc %	Te Conc %	Ta Conc %
1	0.002	0.007	0.007	0.0008	0.002	0.002	<0.0010	0.0002	<0.0010	0.006	<0.002	0.005	<0.007
2	0.003	0.013	0.009	0.0006	<0.0010	0.002	<0.0010	0.0009	<0.0010	0.003	<0.002	0.003	<0.007
3	0.003	0.009	0.007	0.0007	<0.0010	0.002	<0.0010	0.0003	<0.0010	0.006	<0.002	0.005	<0.007
Rep	*0.003*	*0.010*	*0.007*	*0.0007*	*0.001*	*0.002*	<0.0010	*0.0004*	<0.0010	*0.005*	<0.002	*0.005*	<0.007
SD	*0.0004*	*0.003*	*0.001*	*0.0001*	*0.0008*	*0.0002*	*0.0000*	*0.0004*	*0.0000*	*0.002*	*0.0000*	*0.0009*	*0.0000*
RSD	*13.23*	*29.34*	*15.84*	*19.41*	*56.9*	*15.55*		*81.4*	*0.0000*	*38.79*	*0.0000*	*20.56*	*0.0000*

	B Conc %	Zn Conc %	La Conc %	N Conc %	Fe Conc %
1	0.002	0.004	<0.0003	0.003	99.3
2	0.002	0.007	0.001	0.007	99.3
3	0.002	0.004	<0.0003	0.002	99.3
Rep	*0.002*	*0.005*	*0.0006*	*0.004*	*99.3*
SD	*0.0002*	*0.001*	*0.0005*	*0.003*	*0.022*

Ethiopian Conformity Assessment

Sample Results

1

Sample Results

SPECTRO

	B Conc %	Zn Conc %	La Conc %	N Conc %	Fe Conc %
RSD	9.87	26.89	80.9	70.0	0.022

Ethiopian Conformity Assessment Enterprise ARCHIVES

Sample Results

30/06/2025

2

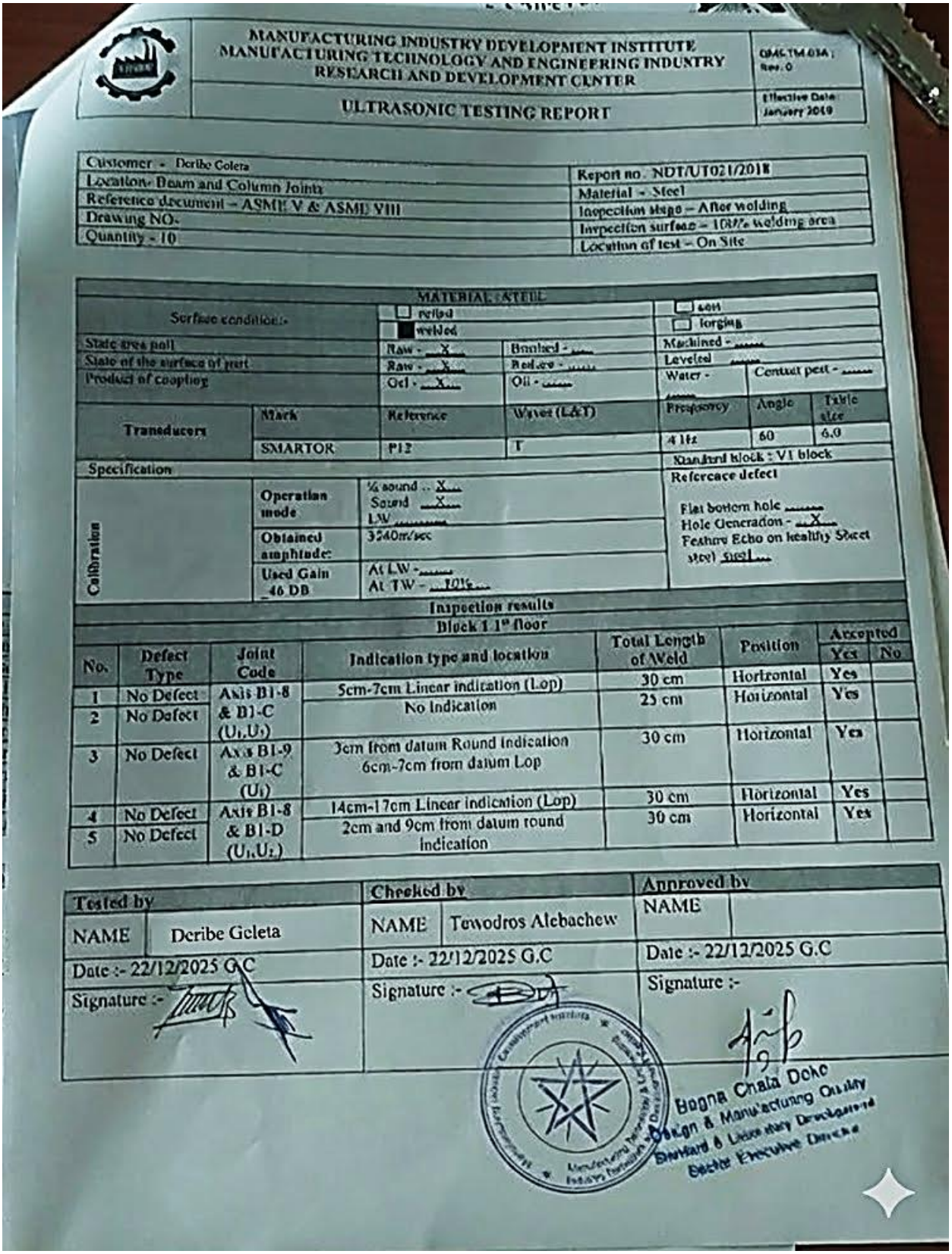

MANUFACTURING INDUSTRY DEVELOPMENT INSTITUTE
MANUFACTURING TECHNOLOGY AND ENGINEERING INDUSTRY RESEARCH AND DEVELOPMENT CENTER

QMS-TM-03A | Rev. 0 | Effective Date: January 2019

ULTRASONIC TESTING REPORT

Customer - Deribe Goleta	Report no. NDT/UT021/2018
Location- Beam and Column Joints	Material - Steel
Reference document – ASME V & ASME VIII	Inspection stage – After welding
Drawing NO.	Inspection surface – 100% welding area
Quantity - 10	Location of test – On Site

MATERIAL : STEEL						
Surface condition:-	☐ rolled ■ welded		☐ cast ☐ forging			
State area nail	Raw - X	Brushed -	Machined -			
State of the surface of part	Raw - X	Reduce -	Leveled			
Product of coupling	Oil - X	Oil -	Water -	Contact past -		
Transducers	Mark	Reference	Wave (L&T)	Frequency	Angle	Table size
	SMARTOR	P12	T	4 Hz	60	6.0
Specification				Standard block : V1 block		
Calibration	Operation mode	¼ sound .. X Sound ..X LW		Reference defect Flat bottom hole ..... Hole Generation - ..X.. Feature Echo on healthy Sheet steel Steel....		
	Obtained amplitude:	3240m/sec				
	Used Gain _46 DB	At LW - ..... At TW - ..10%..				

Inspection results

Block 1 1st floor

No.	Defect Type	Joint Code	Indication type and location	Total Length of Weld	Position	Accepted Yes	Accepted No
1	No Defect	Axis B1-8 & B1-C (U_1,U_3)	5cm-7cm Linear indication (Lop)	30 cm	Horizontal	Yes	
2	No Defect		No Indication	25 cm	Horizontal	Yes	
3	No Defect	Axis B1-9 & B1-C (U_1)	3cm from datum Round indication 6cm-7cm from datum Lop	30 cm	Horizontal	Yes	
4	No Defect	Axis B1-8 & B1-D (U_1,U_2)	14cm-17cm Linear indication (Lop)	30 cm	Horizontal	Yes	
5	No Defect		2cm and 9cm from datum round indication				

Tested by	Checked by	Approved by
NAME Deribe Geleta	NAME Tewodros Alebachew	NAME
Date :- 22/12/2025 G.C	Date :- 22/12/2025 G.C	Date :- 22/12/2025 G.C
Signature :-	Signature :-	Signature :-

Bogna Chala Dako
Design & Manufacturing Quality Standard & Laboratory Development Sector Executive Director

Fig.A. 1 Composition (spectroscopy results) and ultrasonic results

B. Yield strength

This appendix provides the complete statistical modeling, validation, and optimization results related to yield strength obtained from MIG welding experiments, supporting the response surface analysis presented in Chapter 4. The Fit Summary results for the MIG welding yield strength model, presented in Table A. 1, provide important insights into the adequacy of different polynomial models and help identify the most suitable one for prediction and optimization. The linear model shows a very small sequential p-value (<0.0001), indicating that linear terms are significant in explaining the variation in yield strength. Its adjusted R^2 (0.9169) and predicted R^2 (0.9039) are also high, meaning that the linear model captures a large portion of the variability with good predictive power. However, the analysis of higher-order models shows potential for further improvement. The two-factor interaction (2FI) model does not significantly improve the fit, as reflected by a sequential p-value of 0.5967 and only marginal changes in adjusted and predicted R^2 values. This suggests that simple pairwise interactions between parameters are not strong enough to substantially affect the response.

The quadratic model, however, is both statistically significant and suggested by the software. It shows a sequential p-value <0.0001, confirming that the quadratic terms add significant explanatory power to the model. The adjusted R^2 (0.9830) and predicted R^2 (0.9761) values are very high and much closer to each other, indicating that the quadratic model not only fits the data well but also has excellent predictive capability with minimal risk of overfitting. This balance strongly supports the quadratic model as the most appropriate choice. The cubic model, while also showing very high R^2 values (adjusted R^2 = 0.9978 and predicted R^2 = 0.9970), is classified as aliased. This means that due to the limitations of the experimental design and the available data points, the cubic terms cannot be uniquely estimated, and some terms are confounded with others. As a result, even though the fit statistics appear excellent, the cubic model cannot be reliably interpreted.

Based on the guideline to select the highest-order polynomial where the additional terms are significant and the model is not aliased, the quadratic model is the most appropriate model for yield strength prediction in MIG welding. It balances statistical significance, predictive accuracy, and model stability, making it suitable for both understanding the process and guiding parameter optimization.

Table A. 1 Fit summary of yield strength

Source	Sequential p-value	Lack of Fit p-value	Adjusted R^2	Predicted R^2	
Linear	< 0.0001		0.9169	0.9039	
2FI	0.5967		0.9135	0.8910	
Quadratic	**< 0.0001**		**0.9830**	**0.9761**	**Suggested**
Cubic	< 0.0001		0.9978	0.9970	**Aliased**

Source	Sum of Squares	df	Mean Square	F-value	p-value	
Mean vs Total	5.265E+06	1	5.265E+06			
Linear vs Mean	3240.40	3	1080.13	114.95	< 0.0001	
2FI vs Linear	18.75	3	6.25	0.6395	0.5967	
Quadratic vs 2FI	**202.19**	**3**	**67.40**	**35.17**	**< 0.0001**	**Suggested**
Cubic vs Quadratic	37.60	4	9.40	37.10	< 0.0001	Aliased
Residual	4.56	18	0.2534			
Total	5.269E+06	32	1.646E+05			

B.1 Statistical model validation and optimization results for MIG welding yield strength

This section presents regression diagnostics, ANOVA outputs, and optimization results used to validate the adequacy and predictive accuracy of the yield strength model. The statistical analysis of MIG welding yield strength presented in Fig.A. 2 demonstrates the reliability and validity of the developed regression model. The predicted versus actual plot shows that the experimental data points lie very close to the diagonal line, confirming an excellent agreement between measured and model-predicted yield strength values. This high level of correlation indicates that the regression model has strong predictive accuracy within the investigated parameter ranges. The cube plot further illustrates the interaction effects among the key process variables of current, voltage, and welding speed. Yield strength is not governed by a single parameter alone but rather by its combined influence. The highest predicted yield strength, approximately 426 MPa, is observed at higher levels of current and voltage, along with optimized welding speed, highlighting the presence of significant interactive effects. The residual diagnostics provide further evidence supporting the adequacy of the model. The normal probability plot of residuals confirms that the

residuals follow a nearly normal distribution, validating the fundamental assumptions of regression analysis. The residuals versus run plot reveals no systematic patterns, indicating that the experimental data were collected without hidden trends or biases and that the model predictions are stable across all runs. Similarly, the residuals versus current plot shows no observable dependence, suggesting that the model has successfully captured the true influence of current on yield strength.

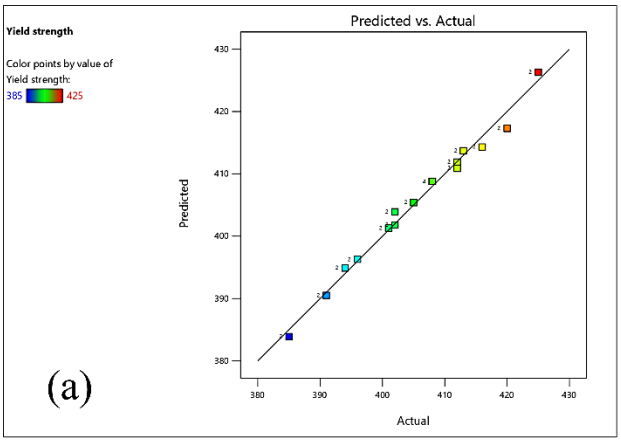

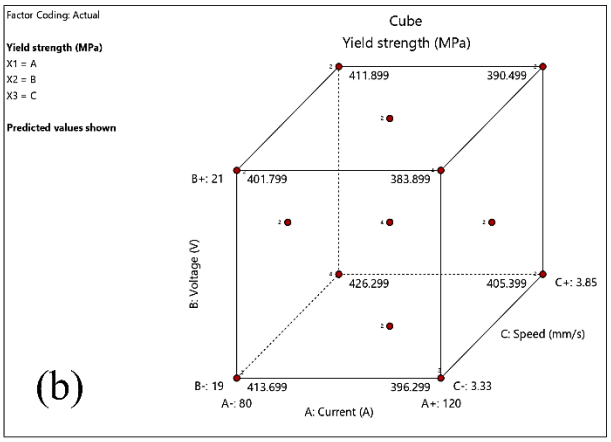

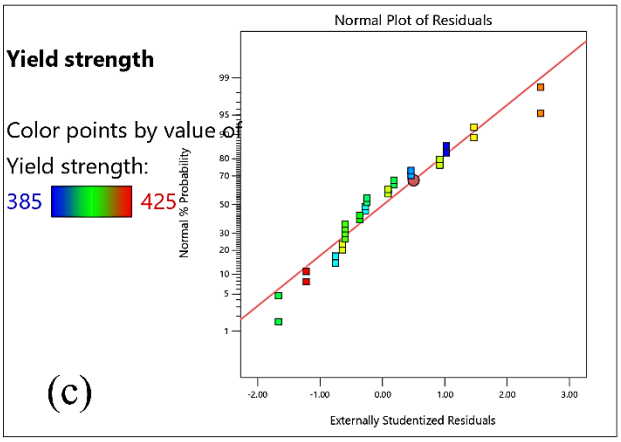

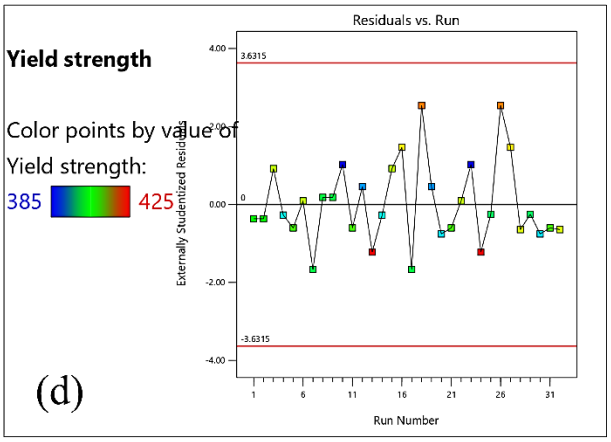

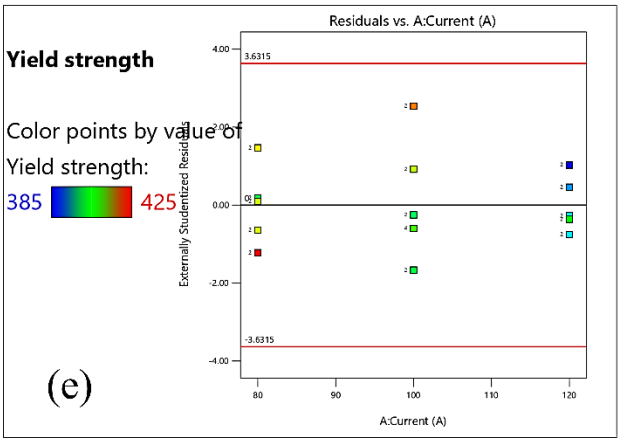

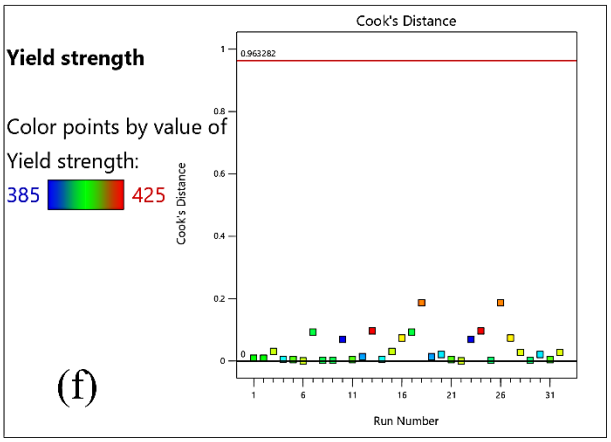

Fig.A. 2 Diagnostic plots for the regression model of MIG welding yield strength, showing predicted vs. actual values, cube plot of parameter interactions, residual analyses, and Cook's distance

Finally, Cook's distance values remain well below the threshold, proving that no single experimental run disproportionately influenced the regression model or acted as an outlier. Therefore, the diagnostic checks presented in Fig. A1 establish that the regression model is both statistically sound and experimentally consistent. The close agreement between predicted and actual values, the normal distribution of residuals, the absence of influential outliers, and the strong interaction effects identified among the process variables all indicate that the model can be confidently applied for optimizing MIG welding yield strength. The results clearly demonstrate that by selecting the appropriate combination of current, voltage, and welding speed, weld joints with superior mechanical performance can be achieved.

B2. Optimization and Desirability Analysis of MIG Welding Yield Strength

This section documents the desirability function analysis and parameter optimization process used to determine the optimal welding conditions for maximizing yield strength. The statistical optimization and diagnostic plots of MIG welding yield strength presented in Fig. A2 provide a deeper understanding of the model behavior and the contribution of each process variable to the overall response. The leverage versus run plot Fig.A. 3 (a) confirms that all experimental data points lie below the critical leverage limit, indicating that none of the runs exerted undue influence on the regression model. This suggests that the experimental design was balanced and all runs contributed fairly to the estimation of the regression coefficients. The one-factor desirability plots Fig.A. 3 (b–d, h) illustrate how individual parameters influence the optimization outcome. For welding current (b, h), desirability reaches a maximum around mid-to-high levels, indicating that extremely low or high current reduces the likelihood of achieving the target yield strength. Similarly, the voltage plot Fig.A. 3 (c) shows an increasing desirability with higher voltage levels, suggesting that yield strength is more favorable in this range. The welding speed desirability curve Fig.A. 3 (d), indicates that an intermediate value provides the most favorable condition, while very low or very high travel speeds reduce the optimization potential. These one-factor plots confirm that the response is sensitive to parameter tuning and that optimal performance occurs within a narrow operating window. The interaction plots Fig.A. 3 (e–g) further highlight the combined effects of welding parameters on desirability. The interaction of voltage and speed Fig.A. 3 (e),

reveals that higher voltage combined with moderate-to-high speed produces greater desirability, reinforcing the importance of joint parameter adjustments. The current–speed interaction Fig.A. 3 (f) shows a non-linear trend, where desirability peaks at moderate levels of both factors but drops significantly when either parameter is extreme.

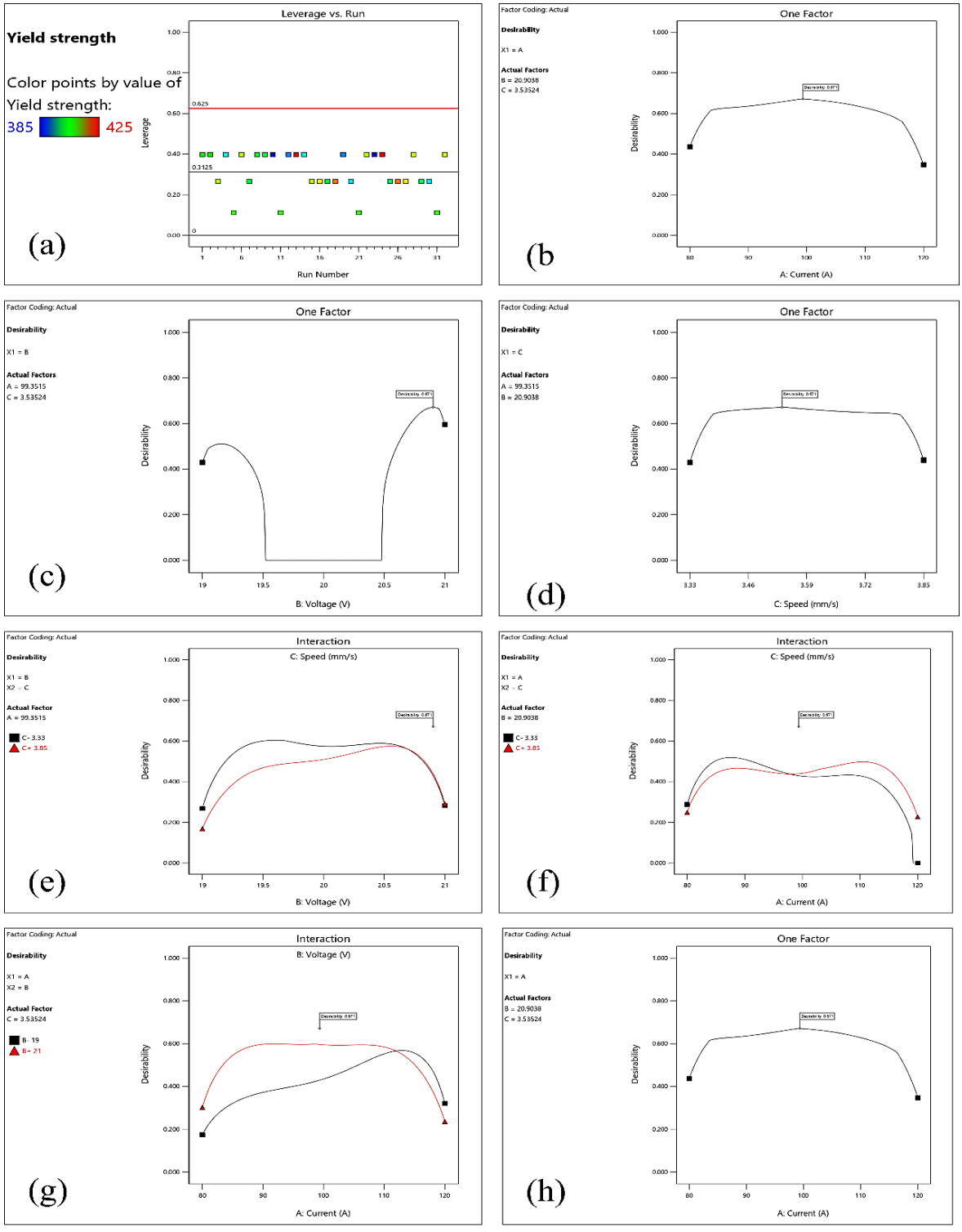

Fig.A. 3 Desirability-based optimization plots for MIG welding yield strength, showing leverage analysis (a), one-factor desirability plots for current, voltage, and speed (b–d, h), and interaction effects among process parameters (e–g)

Similarly, the current–voltage interaction Fig.A. 3 (g) demonstrates that higher desirability is achieved when current and voltage are both set towards their upper ranges, though beyond a certain point, diminishing returns are observed. These interactions confirm that yield strength in MIG welding is not simply a function of isolated parameters but is strongly governed by combined effects. Thus, the optimization analysis demonstrates that yield strength in MIG welding can be effectively maximized through multi-factor optimization. The results show that no single parameter independently ensures superior performance; instead, the combined balance of current, voltage, and welding speed determines the optimum outcome. The desirability analysis confirms that the regression model is capable of identifying precise parameter windows that produce yield strengths near the upper limit of the experimental range. These findings support the practical application of statistical optimization tools in welding parameter selection to ensure joints with enhanced mechanical performance.

C. Statistical validation of MIG welding results (ultimate tensile strength)

This appendix contains the full statistical validation results and regression diagnostics supporting the ultimate tensile strength modeling and analysis discussed in Chapter 4. The Fit Summary results for the ultimate tensile strength (UTS) model, presented in Table A. 2**,** provide a comprehensive evaluation of the model adequacy and statistical significance of different polynomial terms in describing the MIG welding process behavior. The linear model exhibits a highly significant sequential p-value (<0.0001), with an adjusted R^2 of 0.9135 and a predicted R^2 of 0.9000. These high values indicate that the linear terms explain a large proportion of the variation in UTS and that the model has strong predictive reliability. However, while the linear model performs well, additional higher-order terms are tested to determine whether further improvement can be achieved. The two-factor interaction (2FI) model yields a sequential p-value of 0.5846, indicating that the interaction terms between process parameters do not significantly enhance the model's predictive ability. Moreover, the adjusted R^2 and predicted R^2 values (0.9102 and 0.8878, respectively) are slightly lower than those of the linear model, confirming that the inclusion of 2FI terms does not contribute meaningful improvement. This suggests that UTS is not substantially influenced by direct pairwise interactions among the process variables but may instead depend on non-linear effects captured by higher-order terms. The quadratic model demonstrates a sequential p-value <0.0001, confirming its statistical significance and substantial improvement over the previous models. The adjusted R^2 (0.9828) and predicted R^2 (0.9760) values

are both very high and closely aligned, indicating excellent agreement between the model and the experimental data, as well as robust predictive performance with minimal overfitting. The high F-value (36.06) for the quadratic terms further reinforces that the inclusion of squared components significantly improves the model's accuracy in describing the UTS response. Although the cubic model also presents very high R^2 values (adjusted R^2 = 0.9963, predicted R^2 = 0.9951), it is classified as aliased, meaning that due to the experimental design limitations, certain cubic terms are confounded and cannot be distinctly interpreted. Consequently, while the cubic model mathematically appears superior, it cannot be practically relied upon for accurate or independent parameter estimation. Based on the standard model selection criteria—to choose the highest-order polynomial in which additional terms are statistically significant and the model is not aliased, the quadratic model is identified as the most suitable for predicting ultimate tensile strength (UTS) in MIG welding. This model offers the optimal balance of statistical significance, high predictive accuracy, and interpretability, making it an appropriate and robust choice for process optimization and for identifying the optimal welding parameter combinations that yield maximum UTS.

Table A. 2 Fit summary of UTS

Source	Sequential p-value	Lack of Fit p-value	Adjusted R^2	Predicted R^2	
Linear	< 0.0001		0.9135	0.9000	
2FI	0.5846		0.9102	0.8878	
Quadratic	< 0.0001		0.9828	0.9760	Suggested
Cubic	< 0.0001		0.9963	0.9951	Aliased

Source	Sum of Squares	df	Mean Square	F-value	p-value	
Mean vs Total	8.074E+06	1	8.074E+06			
Linear vs Mean	5309.00	3	1769.67	110.14	< 0.0001	
2FI vs Linear	33.00	3	11.00	0.6597	0.5846	
Quadratic vs 2FI	346.43	3	115.48	36.06	< 0.0001	Suggested

Cubic vs Quadratic	58.00	4	14.50	20.97	< 0.0001	Aliased
Residual	12.45	18	0.6916			
Total	8.080E+06	32	2.525E+05			

The statistical validation results for the MIG welding experiments are presented in Fig.A. 4. The normal probability plot of residuals indicates that the residuals follow a near-linear trend along the reference line, confirming that the errors are approximately normally distributed. This validates one of the key regression assumptions and ensures that statistical inferences such as confidence intervals and significance levels are reliable. The residuals versus predicted values plot further supports the adequacy of the model, as the data points are randomly scattered around zero without any systematic trend or funnel-shaped spread, indicating that variance is stable across the predicted range of ultimate tensile strength (UTS) values. The Box–Cox transformation test shows a current lambda of one with the recommendation of no transformation, suggesting that the data do not require any form of variance-stabilizing transformation and that the model is already appropriately specified. The predicted versus actual UTS plot demonstrates an excellent fit between the experimental and modeled values, as the data points fall almost perfectly along the 45° line, highlighting the accuracy of the regression model in capturing the underlying behavior of the MIG welding process. The leverage versus run plot shows that all points fall below the critical threshold, which means no single data point exerts excessive influence on the fitted model. Similarly, the DFFITS versus run results indicate that all observations lie within the acceptable bounds, confirming that no experimental run disproportionately affects the model predictions. The DFBETAS for intercept values also fall well within the control limits, showing that the stability of the regression coefficients is maintained even if individual runs were to be excluded. Finally, the residuals versus run plot shows a random fluctuation of residuals around zero without any discernible pattern, which verifies that the errors are independent and not affected by the sequence of the experimental trials. Consequently, the statistical analysis confirms that the regression model developed for predicting the ultimate tensile strength of MIG-welded joints is robust, well-fitted, and free from violations of regression assumptions. The agreement between predicted and actual values demonstrates the reliability of the model for capturing the influence of welding parameters

on tensile strength, while the absence of influential data points or systematic error patterns ensures that the results are both valid and generalizable. These findings provide strong confidence in using the developed model for process optimization and prediction of mechanical performance in MIG welding applications.

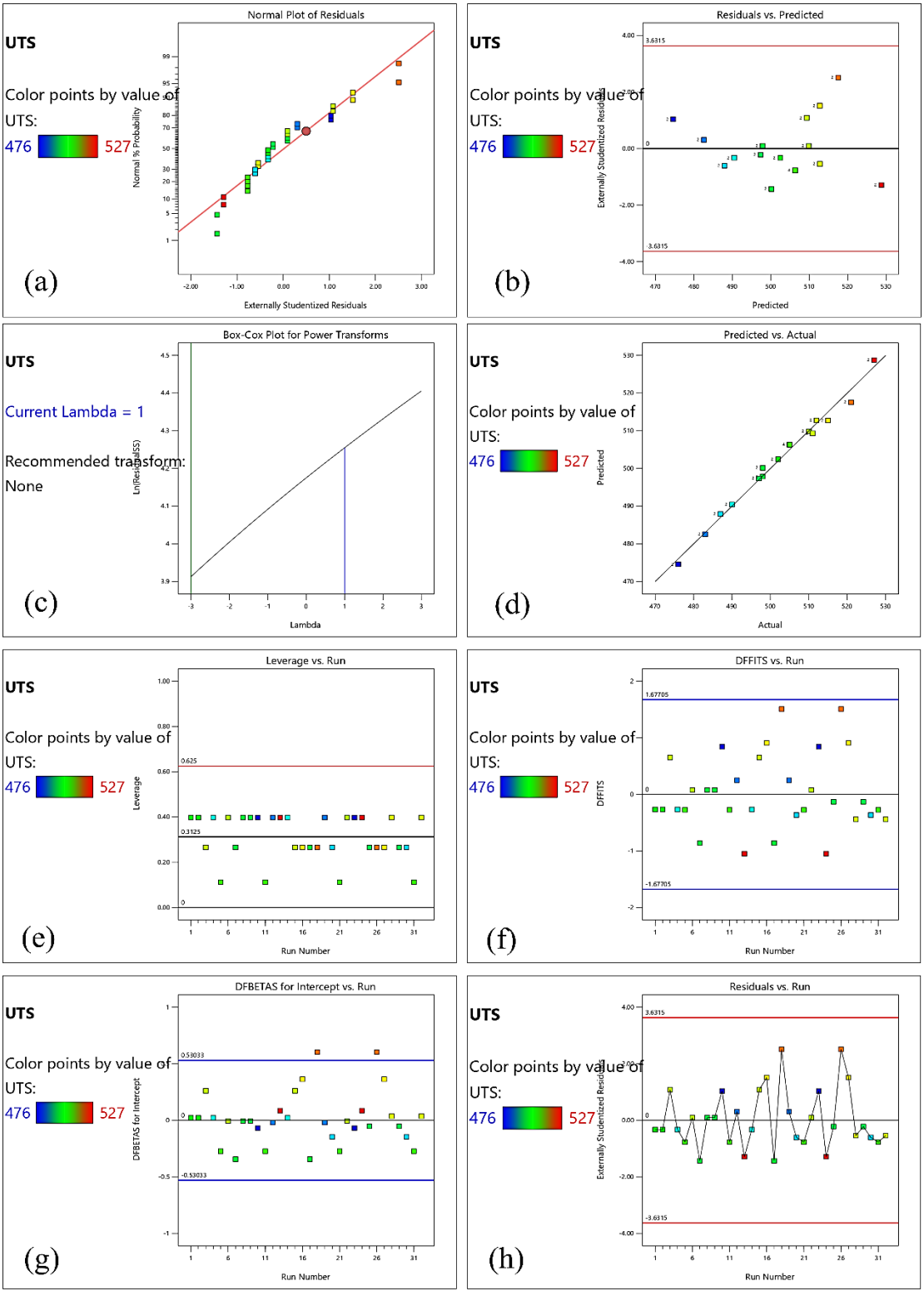

Fig.A. 4 Statistical diagnostic plots for the regression model of ultimate tensile strength (UTS) in MIG welding

C1. Effect of welding parameters on ultimate tensile strength

This section presents detailed regression outputs and response surface plots showing the influence of welding current, voltage, and travel speed on ultimate tensile strength. The MIG welding process optimization results are presented in Fig.A. 5, which shows the perturbation, one-factor, and interaction plots for ultimate tensile strength (UTS). These plots provide valuable insight into the individual and combined influence of current, voltage, and welding speed on the mechanical response of the welded joints. The perturbation plot (Fig.A. 5a) demonstrates the relative sensitivity of UTS to changes in the input parameters. It is evident that current (factor A) exerts the strongest negative influence, as increasing current reduces tensile strength sharply. Voltage (factor B) also shows a negative slope, though its effect is less severe compared to current. Welding speed (factor C) has a positive influence, where higher travel speeds lead to higher UTS within the tested range. This indicates that controlling current and travel speed is more critical for improving weld strength than adjusting voltage alone. The one-factor plots (Figs. A4b–d) further clarify these individual effects. As shown in Fig.A. 5b, UTS decreases steadily with increasing current, suggesting that excessive heat input due to higher current causes coarser grain growth in the weld metal, which in turn lowers tensile strength. Fig. A4c shows that voltage also negatively influences UTS, albeit less significantly, possibly due to the effect of arc length on heat distribution and bead shape. In contrast, Fig.A. 5d reveals that increasing welding speed slightly improves UTS, likely due to lower heat input per unit length, which results in finer microstructures and reduced softening in the heat-affected zone. The interaction plots (Fig.A. 5e–f) highlight the combined effects of parameters. Fig.A. 5e shows the interaction between current and voltage, where the combined increase of both parameters results in a sharp decline in tensile strength. This outcome suggests that simultaneous high current and voltage lead to excessive heat input, causing wider beads, slower cooling, and poor microstructural refinement. Fig.A. 5f illustrates the interaction between current and welding speed. At higher currents, the beneficial effect of increased welding speed is diminished, as the strong negative impact of excessive current dominates. However, at moderate current levels, higher welding speed significantly improves tensile strength, demonstrating that optimizing the balance between these parameters is crucial. Therefore, the analysis in Fig.A. 5 indicates that current is the most influential factor, followed by voltage and welding speed. High welding currents consistently reduce UTS, while higher welding speeds improve it within the studied range. Voltage shows a moderate but negative effect. Importantly, the interaction plots

demonstrate that inappropriate combinations of parameters, especially high current with high voltage, can severely deteriorate weld strength. These findings validate the regression model developed for UTS prediction and provide a clear pathway for optimizing MIG welding parameters to achieve stronger weld joints.

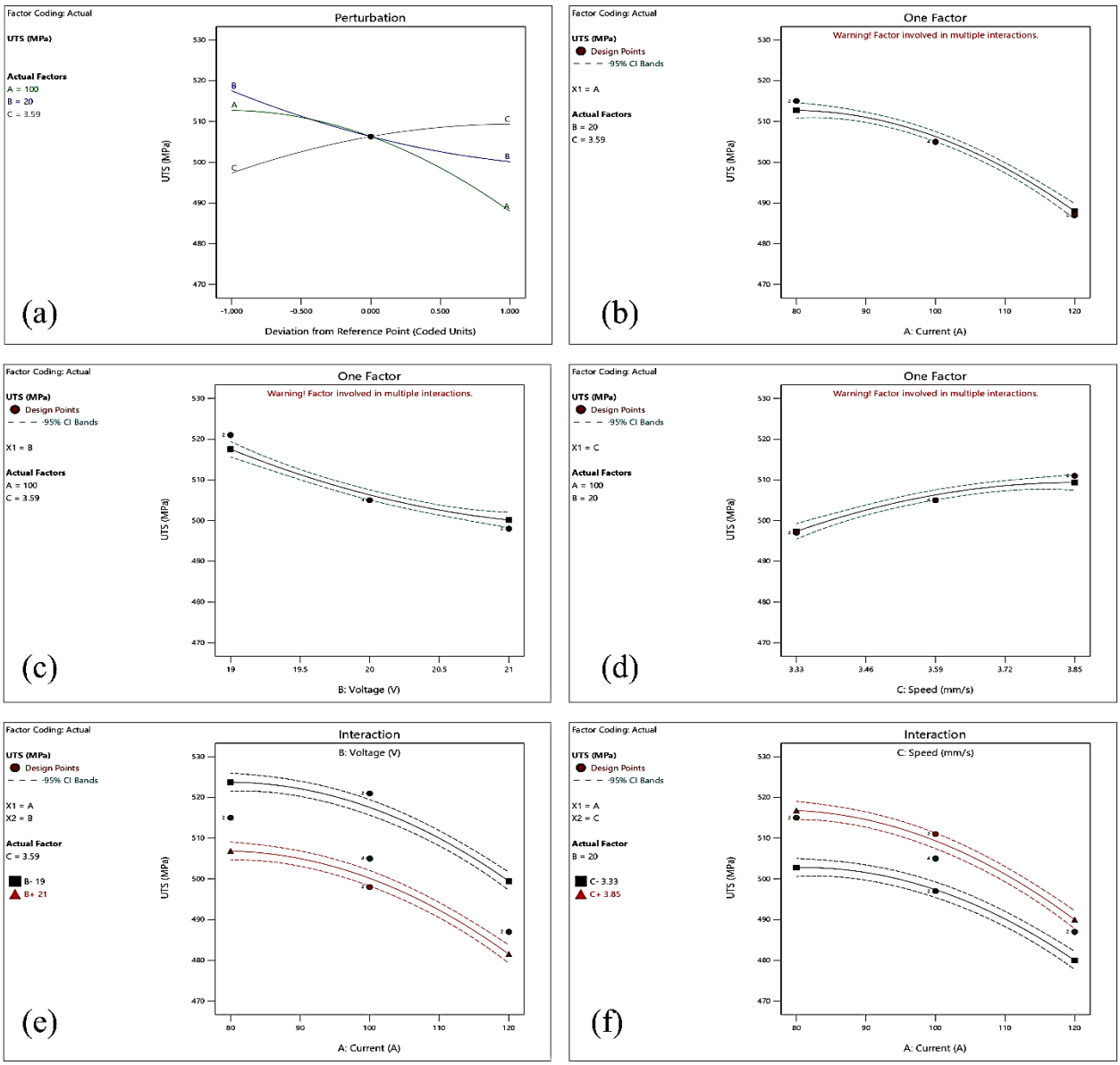

Fig.A. 5 Perturbation, one-factor, and interaction plots showing the influence of current, voltage, and welding speed on ultimate tensile strength (UTS) in MIG welding

D. Selection of the appropriate polynomial model for strain at fracture

This appendix documents the model selection process and statistical criteria used to identify the most appropriate regression model for predicting strain at fracture. In analyzing the fit summary

presented in Table A. 3 for the strain at fracture, it is evident that the selection of an appropriate polynomial model must balance statistical significance with model reliability. The linear model is highly significant with a sequential p-value less than 0.0001, capturing approximately 90% of the variation in the response as indicated by an adjusted R^2 of 0.9057. However, the introduction of two-factor interaction (2FI) terms does not improve the model, as reflected by a sequential p-value of 0.6226 and a slight decrease in adjusted R^2, suggesting that these additional terms are not statistically meaningful in explaining the variation in strain at fracture. In contrast, the quadratic model demonstrates substantial improvement over both the linear and 2FI models, with a sequential p-value less than 0.0001 and an adjusted R^2 of 0.9778, indicating that the inclusion of squared terms captures significant curvature effects in the response. While the cubic model shows a further increase in adjusted R^2 to 0.9928 and is statistically significant, it is aliased, meaning that some model terms cannot be uniquely estimated due to confounding, which renders it unreliable for interpretation. Examination of the ANOVA comparisons reinforces this conclusion: the addition of quadratic terms over the 2FI model significantly enhances the model fit, whereas 2FI terms themselves do not contribute significantly when added to the linear model, and cubic terms, although statistically significant, cannot be safely interpreted due to aliasing. Therefore, the quadratic model emerges as the most appropriate choice, representing the highest-order polynomial that is both statistically significant and free from aliasing, providing a reliable and comprehensive representation of the strain at fracture while capturing essential nonlinear effects.

Table A. 3 Fit summary of strain at fracture

Source	Sequential p-value	Lack of Fit p-value	Adjusted R^2	Predicted R^2	
Linear	< 0.0001		0.9057	0.8910	
2FI	0.6226		0.9014	0.8771	
Quadratic	< 0.0001		0.9778	0.9698	Suggested
Cubic	< 0.0001		0.9928	0.9905	Aliased

Source	Sum of Squares	df	Mean Square	F-value	p-value
Mean vs Total	15904.36	1	15904.36		
Linear vs Mean	40.12	3	13.37	100.21	< 0.0001
2FI vs Linear	0.2500	3	0.0833	0.5975	0.6226

Quadratic vs 2FI	2.80	3	0.9321	29.70	< 0.0001	Suggested
Cubic vs Quadratic	0.5080	4	0.1270	12.53	< 0.0001	Aliased
Residual	0.1824	18	0.0101			
Total	15948.22	32	498.38			

D1. Statistical Validation of MIG Welding Results for Strain at Fracture

This section presents ANOVA tables and diagnostic plots used to verify the adequacy and accuracy of the strain-at-fracture regression model. The statistical diagnostic analysis for the strain at fracture in MIG welding experiments is presented in Fig.A. 6. These results evaluate the adequacy of the regression model developed for predicting strain at fracture and confirm the validity of the underlying statistical assumptions. The DFBETAS versus run plot (Fig.A. 6a) shows that all values fall within the control limits, indicating that no single observation exerts an excessive influence on the model intercept. Similarly, the DFFITS versus run plot (Fig.A. 6b) demonstrates that all experimental points lie within the acceptable range, confirming that no individual run disproportionately affects the overall regression fit. This suggests that the dataset is well-balanced and free from influential outliers that could bias parameter estimation. The Box–Cox transformation test (Fig.A. 65c) reveals that the current lambda value is one, with no transformation recommended. This confirms that the strain-at-fracture data are adequately modeled without the need for power transformations and that variance stability is maintained across the dataset. The predicted versus actual values plot (Fig.A. 6d) illustrates a near-perfect alignment of points along the 45° reference line, indicating excellent agreement between the experimental results and the model predictions. This highlights the accuracy and robustness of the regression model in predicting strain at fracture. The residuals versus run plot (Fig.A. 6e) shows random scattering around zero without any discernible systematic pattern, verifying the independence of residuals across experimental trials. Similarly, the residuals versus current plot (Fig.A. 6f) demonstrates that the residuals are randomly distributed with no visible trend, confirming that model errors are not correlated with variations in welding current. Together, these results confirm that assumptions of normality, homoscedasticity, and independence have been satisfied. Overall, the diagnostic analysis in Fig.A. 6 confirms that the regression model developed for predicting strain at fracture in MIG-welded joints is statistically sound, free from outliers or

influential points, and highly accurate in reproducing experimental data. This provides strong evidence that the model is suitable for understanding the influence of process parameters on ductility and can be reliably used for optimizing welding conditions to balance strength and toughness.

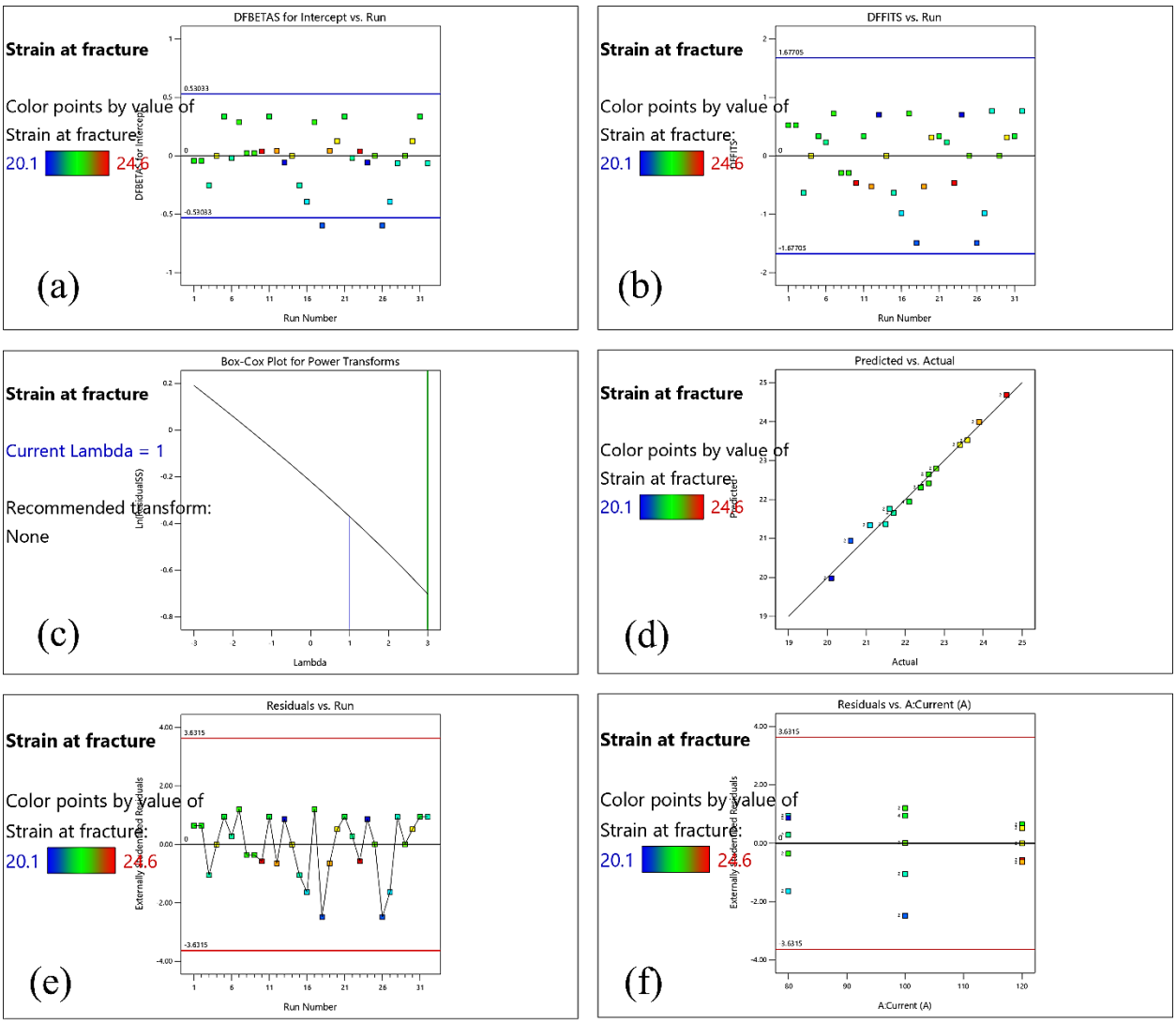

Fig.A. 6 Statistical diagnostic plots for the regression model of strain at fracture in MIG welding

D2. MIG welding results and discussion of welding parameters on strain at fracture

This section provides detailed response surface analyses and regression interpretations showing how welding parameters influence ductility and fracture strain behavior. The results presented in Fig.A. 7 provide a clear picture of how welding parameters influence the strain at fracture in MIG welding. The perturbation plot shows that welding current is the most dominant factor, as strain at fracture increases significantly with higher current. Voltage also contributes positively, though

with a smaller effect, while welding speed exerts a negative influence, indicating that higher travel speed reduces ductility due to insufficient heat input and weaker fusion. The one-factor plot confirms that strain at fracture rises steadily with increasing current, making current optimization essential for improving weld quality. Interaction plots further reveal the combined effects of process parameters. The interaction between current and voltage demonstrates a strong positive relationship, where higher levels of both parameters enhance ductility more than either alone. In contrast, the interaction between current and speed indicates that excessive welding speed suppresses the benefits of increased current, leading to reduced strain at fracture. Similarly, the interaction between voltage and speed shows that while higher voltage generally improves ductility, its positive effect diminishes considerably at higher welding speeds. Overall, these results highlight that current plays the most critical role in determining weld ductility, voltage provides a supportive enhancement, and welding speed is a limiting factor that must be carefully controlled. The findings suggest that optimal welding performance can be achieved under conditions of high current, moderate-to-high voltage, and relatively low welding speed. This combination maximizes heat input, ensures proper fusion, and leads to higher strain at fracture, reflecting improved ductility of the welded joints.

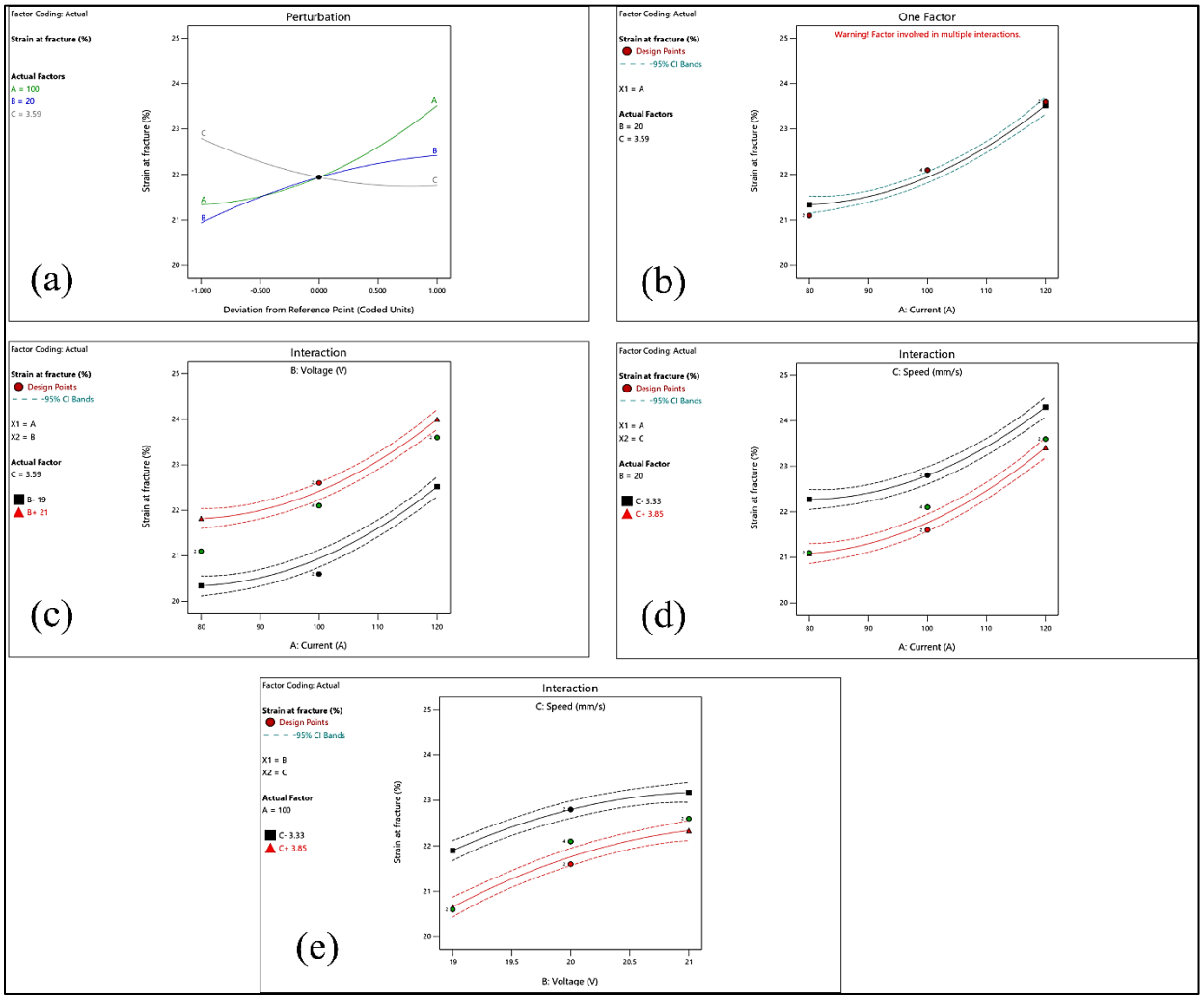

Fig.A. 7 Response surface methodology (RSM) plots for MIG welding showing the effects of welding parameters on strain at fracture (%): (a) perturbation plot, (b) one-factor effect of current, (c) interaction between current and voltage, (d) interaction between current and speed, and (e) interaction between voltage and speed.

E. Model Fit Summary for Hardness at Weld Zone

This appendix presents statistical model fit summaries and regression outputs supporting the hardness prediction analysis for the weld zone. The model summary for hardness at the weld zone is presented in Table A. 4. The linear model was found to be highly significant with a sequential p-value of < 0.0001, and it explained the majority of the variation in the data with an adjusted R^2 of 0.9091 and a predicted R^2 of 0.8956. This indicates that even the linear model provides a strong baseline for describing the relationship between welding parameters and hardness. The addition of two-factor interaction (2FI) terms did not significantly improve the model, as reflected by the high

p-value (0.7643) and only a marginal change in adjusted and predicted R^2 values. This suggests that the two-factor interactions between current, voltage, and speed are not critical in predicting hardness at the weld zone. By contrast, the quadratic model significantly improved the fit, with a sequential p-value of < 0.0001, and achieved a very high adjusted R^2 (0.9885) and predicted R^2 (0.9835). These values are in excellent agreement, indicating strong model predictability without evidence of overfitting. Based on these results, the quadratic model was suggested as the most appropriate representation for this response. Although the cubic model also returned significant results (p-value < 0.0001), it was identified as aliased, meaning it cannot be reliably interpreted due to insufficient degrees of freedom and confounding effects. Therefore, despite its higher R^2 values (adjusted R^2 = 0.9987, predicted R^2 = 0.9982), the cubic model cannot be considered valid. In conclusion, the quadratic model is the most suitable for describing the hardness at the weld zone. It balances statistical significance, high explanatory power, and predictive reliability while avoiding aliasing issues present in the cubic model. This outcome confirms that curvature effects in the welding parameters play an important role in determining hardness at the weld zone, while interaction terms are comparatively less influential.

Table A. 4 Fit summary statistics for hardness at the weld zone (WZ)

Source	Sequential p-value	Lack of Fit p-value	Adjusted R^2	Predicted R^2	
Linear	< 0.0001		0.9091	0.8956	
2FI	0.7643		0.9027	0.8772	
Quadratic	< 0.0001		0.9885	0.9835	Suggested
Cubic	< 0.0001		0.9987	0.9982	Aliased

Source	Sum of Squares	df	Mean Square	F-value	p-value	
Mean vs Total	2.749E+05	1	2.749E+05			
Linear vs Mean	97.98	3	32.66	104.38	< 0.0001	
2FI vs Linear	0.3875	3	0.1292	0.3857	0.7643	
Quadratic vs 2FI	7.50	3	2.50	62.85	< 0.0001	Suggested

Cubic vs Quadratic	0.7920	4	0.1980	43.02	< 0.0001	Aliased
Residual	0.0828	18	0.0046			
Total	2.751E+05	32	8595.47			

E1. Diagnostic plots for hardness at the weld zone

This section includes residual plots, normal probability plots, and leverage diagnostics used to verify the adequacy and assumptions of the weld zone hardness model. The adequacy of the developed model for hardness at the weld zone was verified using diagnostic plots, as shown in Fig.A. 8. The Box–Cox power transformation plot (Fig.A. 8a) shows that the current lambda value is 1, and no transformation is recommended for the response data. This confirms that the hardness values satisfy the assumptions of normality and homoscedasticity without requiring transformation. The DFBETAS plot (Fig.A. 8b) assesses the influence of individual runs on the model coefficients. All data points remain within the control limits (±0.533), indicating that no single observation exerts an undue effect on the regression coefficients. Similarly, the DFFITS plot (Fig.A. 8c) shows all points within the critical bounds (±1.697), confirming that none of the experimental runs disproportionately influences model predictions. The leverage plot (Fig.A. 8d) further validates this, with leverage values of all runs falling below the threshold of 0.625. This suggests that each run contributes reasonably to model fitting without dominating the regression space. Residual analysis was performed to assess the distribution of errors. The residuals vs. run plot (Fig.A. 8e) shows a random scatter around zero without systematic trends, supporting the assumption of independence. Finally, the residuals vs. current (Fig.A. 8f) confirm that residuals are symmetrically distributed across the current range, with no evidence of curvature or heteroscedasticity. Consequently, the diagnostic results confirm that the quadratic regression model for hardness at the weld zone is statistically adequate. The absence of influential points, outliers, or transformation requirements validates the robustness of the model. Therefore, the quadratic model can be reliably used to describe and predict hardness in the weld zone under different MIG welding conditions.

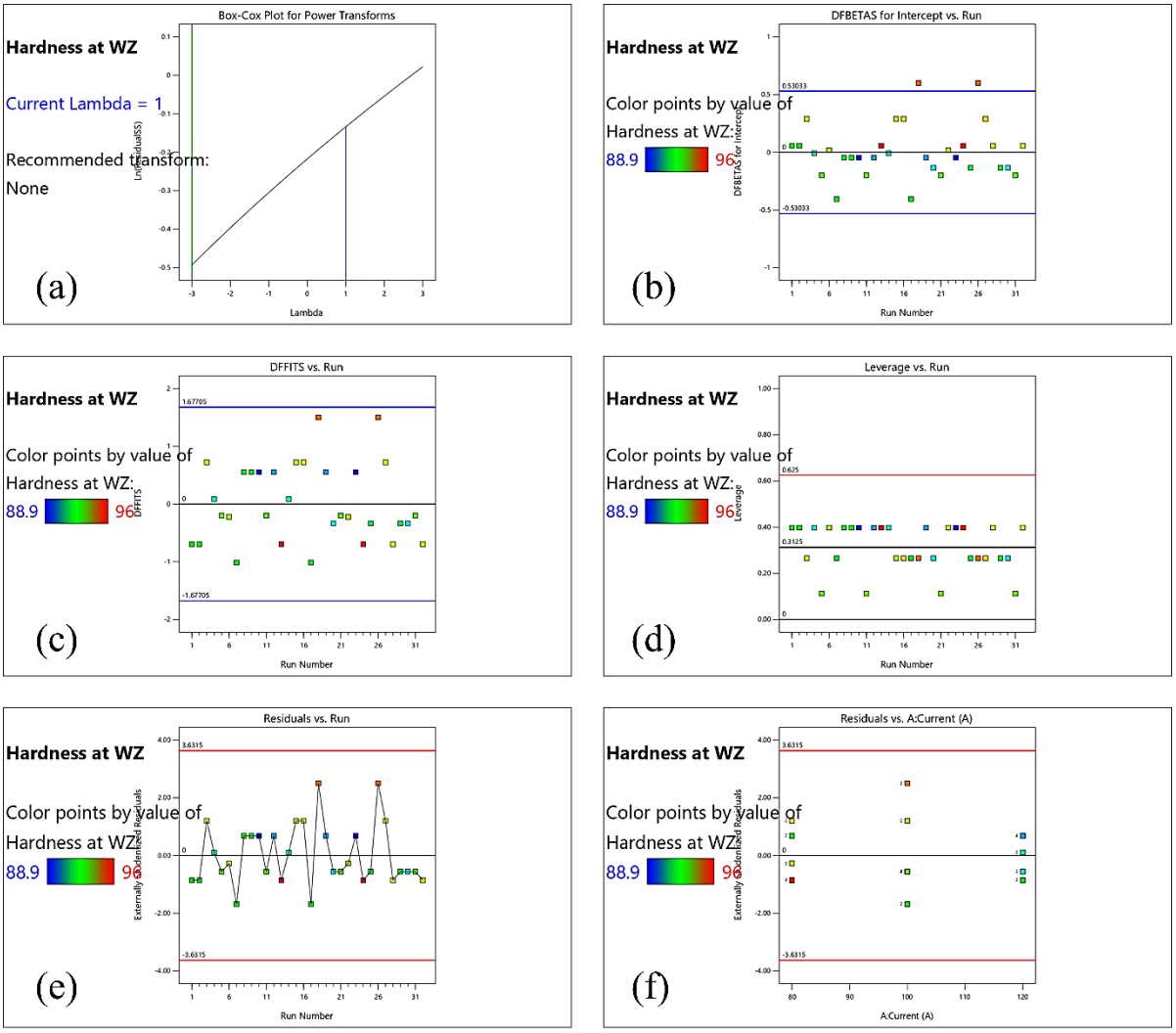

Fig.A. 8 Diagnostic plots for hardness at weld zone (WZ): (a) Box–Cox plot for power transforms, (b) DFBETAS for intercept, (c) DFFITS vs. run, (d) leverage vs. run, (e) residuals vs. run, and (f) residuals vs. current.

E2. MIG welding results for hardness at the weld zone

This section presents detailed response surface plots and regression interpretations showing the influence of welding parameters on weld zone hardness. The effect of MIG welding parameters on hardness at the weld zone is illustrated in Fig. A8. The perturbation plot (Fig.A. 9a) shows that hardness is most sensitive to welding current and speed, both of which have negative slopes. This indicates that higher current and higher welding speed reduce the hardness at the weld zone. Voltage exhibits a smaller but still negative effect, suggesting that all three parameters tend to decrease hardness when increased. Among them, current shows the strongest influence, followed

by speed, while voltage has the least impact. The one-factor plot (Fig.A. 9b) further confirms this trend, where hardness steadily decreases with an increase in welding current. This observation is consistent with the higher heat input at elevated current levels, which promotes grain coarsening and softening in the weld zone, thereby lowering hardness. The two-factor interaction plots provide further insights. The interaction between current and voltage (Fig.A. 9c) demonstrates that hardness decreases with increasing levels of both parameters, with the combined effect being more pronounced than their individual effects. Similarly, the interaction between current and speed (Fig.A. 9d) shows that higher values of both parameters result in lower hardness, indicating that rapid heat input and fast cooling reduce structural refinement in the weld zone. Finally, the interaction between voltage and speed (Fig.A. 9e) reveals a similar negative interaction: simultaneous increases in voltage and speed consistently lead to reduced hardness values. Consequently, these results suggest that welding parameters have a strong influence on weld zone hardness, predominantly through heat input effects. Excessive current and voltage increase the heat supplied, while higher welding speed reduces the cooling time, both of which contribute to softening and reduced hardness in the weld zone. Hence, to maintain higher hardness levels, the welding process should be carried out under relatively moderate current and voltage values combined with a lower welding speed. This balance ensures controlled heat input, finer grain structure, and improved hardness at the weld zone.

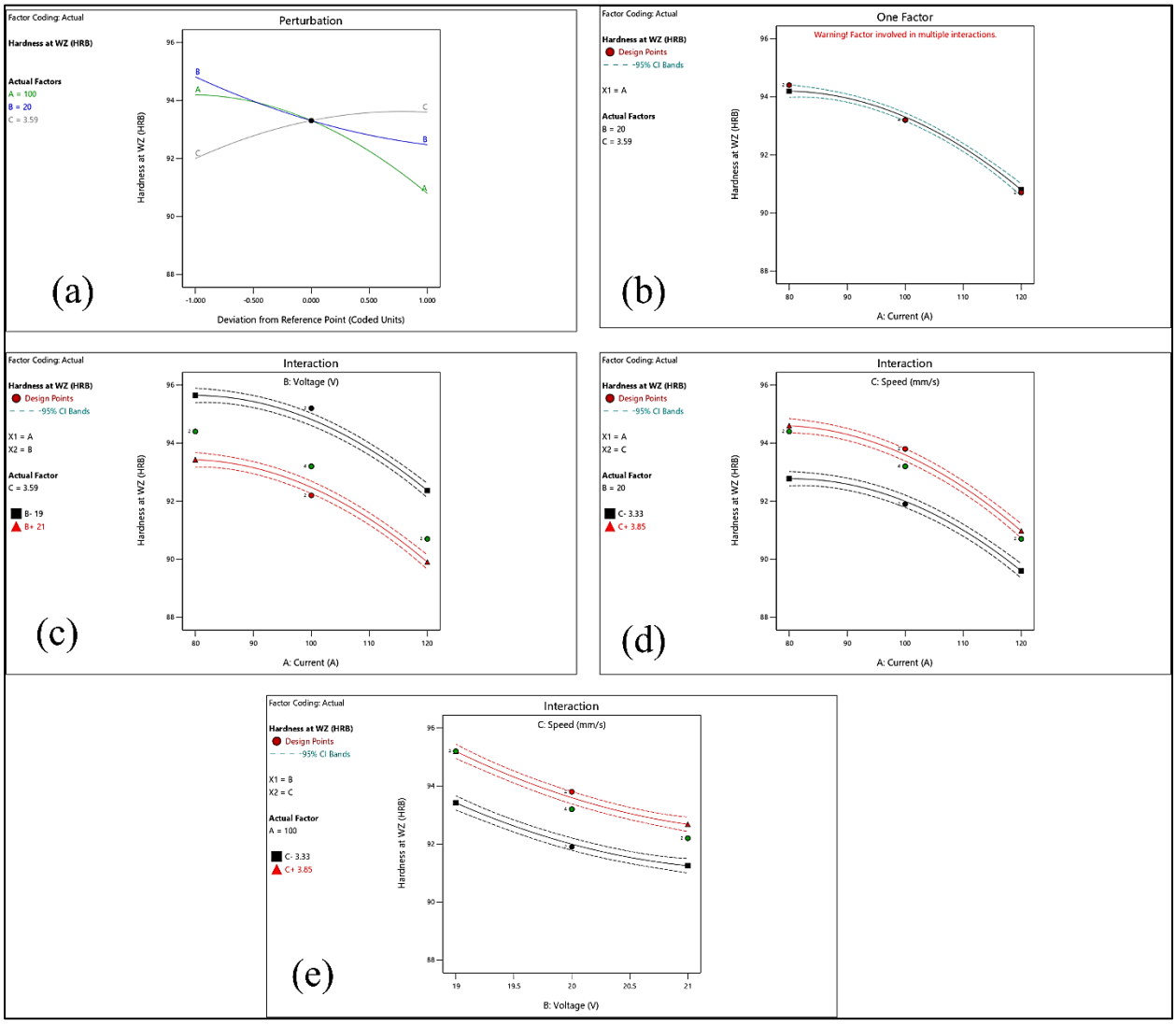

Fig.A. 9 Response surface methodology (RSM) plots for hardness at weld zone (WZ): (a) perturbation plot, (b) one-factor effect of current, (c) interaction between current and voltage, (d) interaction between current and speed, and (e) interaction between voltage and speed

F. Model Fit Summary for Hardness at Heat Affected Zone (HAZ)

This appendix presents statistical model summaries and regression outputs supporting hardness prediction in the heat-affected zone. The model summary for hardness at the HAZ is presented in Table A. 5. The linear model was highly significant with a sequential p-value of < 0.0001, and produced an adjusted R^2 of 0.9020 and a predicted R^2 of 0.8871, both indicating a strong explanatory and predictive capability. This shows that hardness at the HAZ is strongly influenced by the main welding parameters. The two-factor interaction (2FI) model did not significantly improve the fit, as reflected by the high sequential p-value (0.7190) and the lower adjusted and

predicted R^2 values compared to the linear model. This confirms that interaction effects between current, voltage, and speed are not critical in predicting hardness at the HAZ. The quadratic model, however, significantly enhanced the fit, with a sequential p-value of < 0.0001. The model achieved an adjusted R^2 of 0.9858 and a predicted R^2 of 0.9797, which are both in close agreement. This strong alignment demonstrates the high reliability of the quadratic model in both fitting the observed data and predicting new values. Based on these results, the quadratic model is suggested as the most appropriate representation for hardness at the HAZ. Although the cubic model also showed statistical significance (p-value < 0.0001), it was identified as aliased, meaning that higher-order terms are confounded with each other due to limited experimental runs. As such, the cubic model cannot be reliably interpreted despite its very high R^2 values (adjusted R^2 = 0.9970, predicted R^2 = 0.9960). Thus, the quadratic model was selected as the best-fitting model for hardness at the HAZ, as it provides both statistical significance and predictive robustness without the aliasing issues seen in the cubic model. This suggests that curvature effects in the welding parameters play a significant role in determining hardness at the HAZ, whereas simple linear and interaction terms alone are insufficient.

Table A. 5 Fit summary of hardness at HAZ

Source	**Sequential p-value**	**Lack of Fit p-value**	**Adjusted R^2**	**Predicted R^2**	
Linear	< 0.0001		0.9020	0.8871	
2FI	0.7190		0.8958	0.8688	
Quadratic	**< 0.0001**		**0.9858**	**0.9797**	**Suggested**
Cubic	< 0.0001		0.9970	0.9960	**Aliased**

Source	**Sum of Squares**	**df**	**Mean Square**	**F-value**	**p-value**
Mean vs Total	2.419E+05	1	2.419E+05		
Linear vs Mean	61.69	3	20.56	96.07	< 0.0001
2FI vs Linear	0.3075	3	0.1025	0.4507	0.7190

Quadratic vs 2FI	**5.00**	**3**	**1.67**	**53.80**	**< 0.0001**	**Suggested**
Cubic vs Quadratic	0.5640	4	0.1410	21.51	< 0.0001	Aliased
Residual	0.1180	18	0.0066			
Total	2.420E+05	32	7561.33			

F1. Model Adequacy Checking for Hardness at HAZ

This section contains diagnostic plots and validation results used to confirm the adequacy and predictive reliability of the hardness model for the heat-affected zone. Fig.A. 10 presents the diagnostic plots used to evaluate the adequacy of the regression model developed for predicting hardness at the heat-affected zone (HAZ) in MIG welding. The DFBETAS plot for the intercept versus run (Fig. A8a) shows that all values lie within the established limits, indicating that no single experimental run exerts an excessive influence on the regression coefficients. Similarly, the DFFITS versus run plot (Fig. A8b) confirms that none of the runs dominate the fitted model since all data points remain within the acceptable range. The Box-Cox power transformation plot (Fig. A8c) suggests that the current Lambda is equal to one, and as it falls within the 95% confidence interval, no transformation of the response variable is necessary, confirming that the original scale of hardness is appropriate for analysis. The residuals versus run plot (Fig. A8d) demonstrates that the residuals fluctuate randomly around zero within the control limits, implying that there are no systematic patterns or biases introduced by the sequence of experiments. The residuals versus predicted plot (Fig. A8e) further supports the adequacy of the model by showing that residuals are symmetrically scattered around zero without any visible curvature or heteroscedasticity, thereby satisfying the assumption of constant variance. Finally, the predicted versus actual values plot (Fig. A8f) exhibits a close alignment of data points along the 45° line, indicating excellent agreement between experimental results and model predictions. Overall, these diagnostics confirm that the regression model is statistically valid, free from significant outliers or influential points, and capable of reliably predicting hardness at the HAZ under the investigated MIG welding conditions.

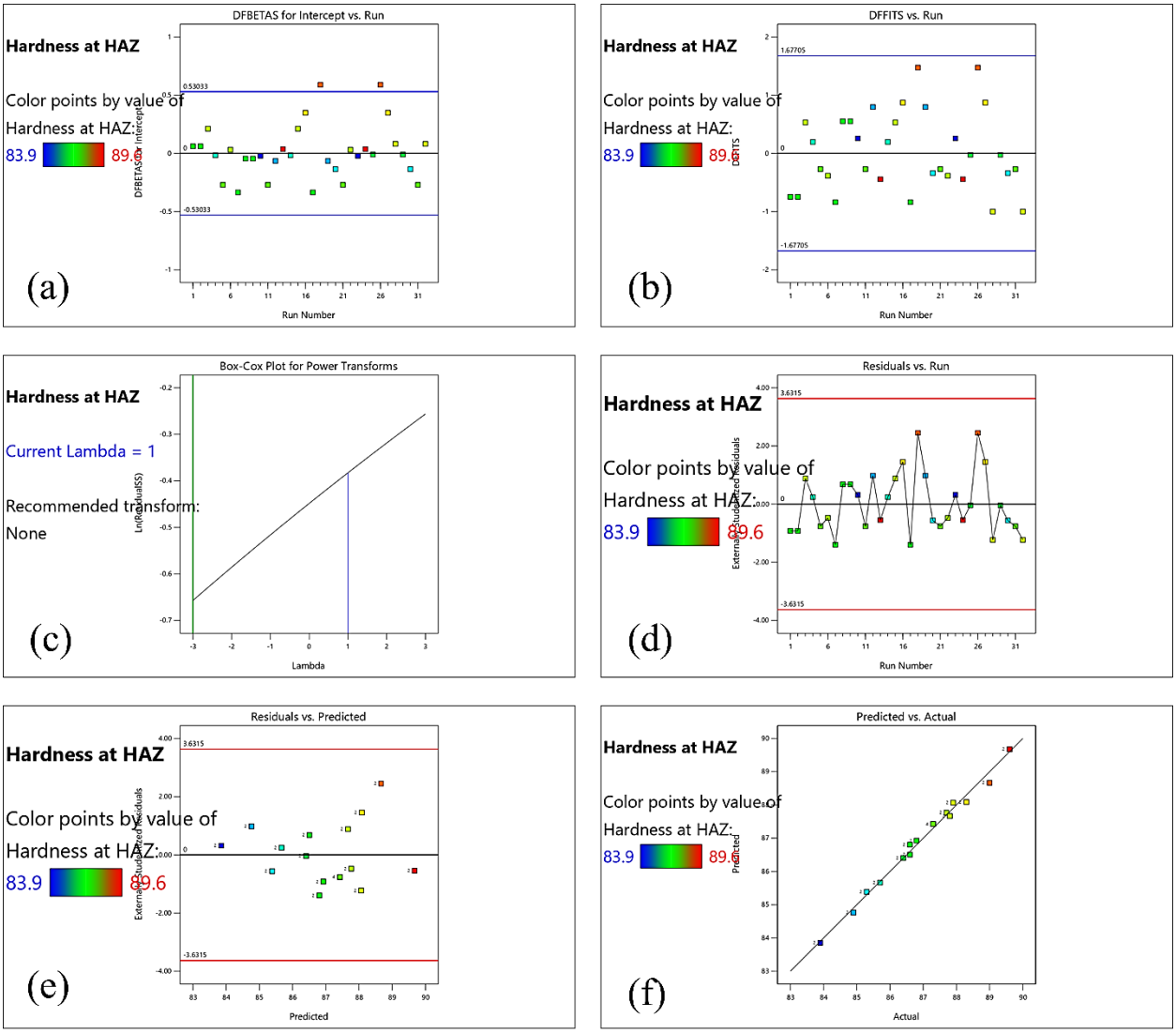

Fig.A. 10 Diagnostic plots for regression model adequacy of hardness at HAZ in MIG welding